

# CONVECTIVELY COUPLED EQUATORIAL WAVES

George N. Kiladis,<sup>1</sup> Matthew C. Wheeler,<sup>2</sup> Patrick T. Haertel,<sup>3</sup> Katherine H. Straub,<sup>4</sup> and Paul E. Roundy<sup>5</sup>

Received 4 March 2008; revised 15 September 2008; accepted 10 November 2008; published 10 April 2009.

[1] Convectively coupled equatorial waves (CCEWs) control a substantial fraction of tropical rainfall variability. Their horizontal structures and dispersion characteristics correspond to Matsuno's (1966) solutions of the shallow water equations on an equatorial beta plane, namely, Kelvin, equatorial Rossby, mixed Rossby-gravity, and inertio-gravity waves. Because of moist processes, the tilted vertical structures of CCEWs are complex, and their scales do not correspond to that expected from the linear theory of dry waves. The dynamical structures and cloud

morphology of CCEWs display a large degree of self-similarity over a surprisingly wide range of scales, with shallow convection at their leading edge, followed by deep convection and then stratiform precipitation, mirroring that of individual mesoscale convective complexes. CCEWs have broad impacts within the tropics, and their simulation in general circulation models is still problematic, although progress has been made using simpler models. A complete understanding of CCEWs remains a challenge in tropical meteorology.

**Citation:** Kiladis, G. N., M. C. Wheeler, P. T. Haertel, K. H. Straub, and P. E. Roundy (2009), Convectively coupled equatorial waves, *Rev. Geophys.*, 47, RG2003, doi:10.1029/2008RG000266.

## 1. HISTORICAL OVERVIEW

[2] Rain falling from cumulus clouds accounts for the majority of precipitation within the tropics. Without the benefit of spaceborne satellite views, to an observer on the ground, much of this rainfall may seem randomly distributed. In some locations, such as within the monsoon regions, precipitation can appear decidedly episodic, with relatively low frequency variability of around a month or so. In fact, the bulk of this tropical convective rainfall is known to be organized over a wide range of spatial and temporal scales, from *mesoscale convective systems* (MCSs) to planetary-scale features such as the *Madden-Julian oscillation* (MJO). (Italicized terms are included in the glossary, after the main text. For full, standard definitions of these and other terms used in this article, refer to *American Meteorological Society* [2000].) At intermediate scales, rainfall is frequently organized by waves that move eastward or westward, either along the equator or within a few degrees of latitude parallel to it within the *Intertropical Convergence Zone* (ITCZ). Research over the past few decades has

established that some of these waves exhibit characteristics described within the classical wave theory of *Matsuno* [1966]. Such *convectively coupled equatorial waves* (CCEWs) are the topic of this article.

[3] The notion that the equatorial region might provide a setting for disturbances that behave distinctly differently from those in the extratropics goes back to *Riehl* [1945], who realized that westward propagating waves were responsible for much of the day-to-day weather variability over the Caribbean. These "easterly waves" (EWs) were identified as inverted troughs of low pressure with a scale of a few thousand kilometers propagating westward within the ITCZ and were implicated in tropical cyclone formation by *Dunn* [1940] and *Riehl* [1948]. Subsequent studies have confirmed that EWs, also known as tropical depression (TD)-type waves, are important features over nearly all regions of the tropics outside the Indian Ocean.

[4] In the late 1950s it was realized that the low-latitude region of a rotating planet could give rise to a particular class of "trapped" motions along the equator [*Yoshida*, 1959; *Rosenthal*, 1960, 1965; *Bretherton*, 1964]. In his classic paper on equatorial motions, *Matsuno* [1966] solved for the zonally propagating wave solutions of a system of equations known as the "*shallow water (SW) equations* on an equatorial beta plane," which govern motions in a layer of constant density fluid when the restoring forces are gravity and a linearly varying Coriolis parameter. The solutions of this system correspond to the now well-known waves of the equatorial atmosphere and ocean, namely, Kelvin, equatorial Rossby (ER), westward and eastward

<sup>1</sup>Earth System Research Laboratory, NOAA, Boulder, Colorado, USA.

<sup>2</sup>Bureau of Meteorology, Centre for Australian Weather and Climate Research, Melbourne, Victoria, Australia.

<sup>3</sup>Department of Geology and Geophysics, Yale University, New Haven, Connecticut, USA.

<sup>4</sup>Department of Earth and Environmental Sciences, Susquehanna University, Selinsgrove, Pennsylvania, USA.

<sup>5</sup>Department of Atmospheric and Environmental Sciences, State University of New York at Albany, Albany, New York, USA.

inertia-gravity (WIG and EIG), and mixed Rossby-gravity (MRG) waves.

[5] At about the same time as the publication of Matsuno's [1966] paper, observational evidence for MRG waves [Yanai and Maruyama, 1966; Maruyama, 1967] and Kelvin waves [Wallace and Kousky, 1968] in the equatorial stratosphere was uncovered. The discovery of these atmospheric modes, along with evidence for their oceanic counterparts shortly afterward [Wunsch and Gill, 1976], was a triumph for equatorial SW theory. As expected theoretically, MRG waves were associated with primarily meridional flow fluctuations, while the Kelvin mode was characterized by primarily zonal fluctuations. The observed stratospheric waves are considered to be *dry* (or "free") modes; that is, once produced, they are uncoupled to convection or any other forcing. Their initial energy source was assumed to be diabatic heating by moist convection in the troposphere since their vertical structure indicated upward energy dispersion, consistent with forcing from below [Holton, 1972, 1973].

[6] The discovery of dry stratospheric Kelvin and MRG waves stimulated great interest in determining the potential for these modes to explain the workings of the stratospheric quasi-biennial oscillation (QBO), the remarkably periodic alteration of westerly to easterly flow that propagates downward through the lower stratosphere with a period of  $\sim 22$  months [see Baldwin *et al.*, 2001]. Prior theoretical work had established that vertically propagating waves in vertical shear would generate vertical fluxes of zonal momentum [Booker and Bretherton, 1967]. This led to the development of the Lindzen and Holton [1968] theory of the forcing of the QBO, with Kelvin waves providing the eastward acceleration and MRG waves providing the westward acceleration, along with an assumed broad spectrum of gravity waves to account for the remaining accelerations not accounted for by the observable modes.

[7] Over subsequent years, satellite data were used to detect both westward and eastward propagating disturbances in cloudiness [Chang, 1970; Yanai and Murakami, 1970a, 1970b; Wallace and Chang, 1972; Reed and Recker, 1971], raising the possibility of convectively coupled counterparts to the dry modes of SW theory. While some of the westward modes were categorized as EWs, the possibility was raised that others might be associated with ER and MRG waves [Holton, 1970, 1971]. There was also speculation that the eastward disturbances might be Kelvin modes [Wallace and Chang, 1972].

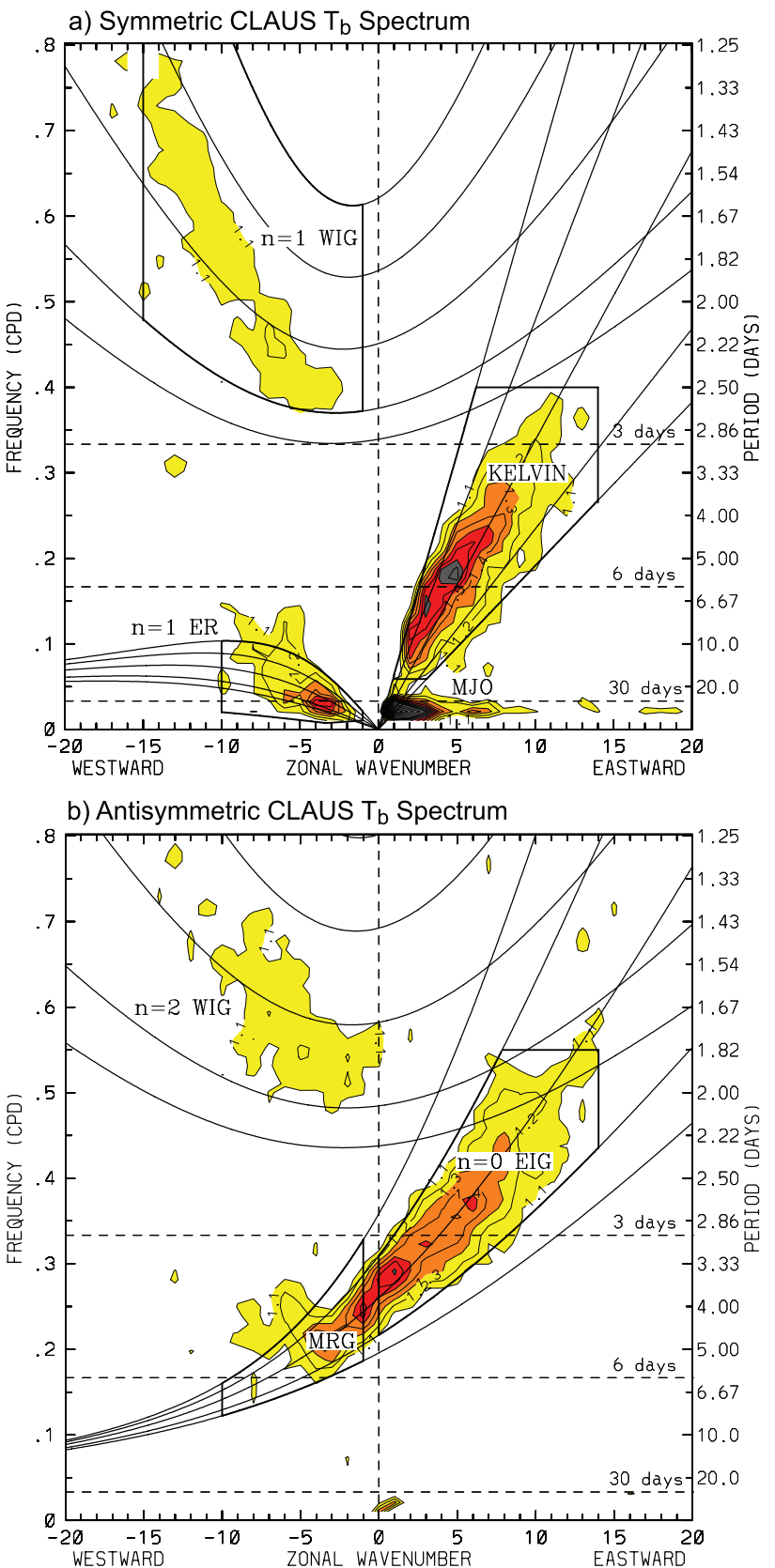
[8] At around the same time, spectral studies by Madden and Julian [1971, 1972] revealed the MJO, consisting of an envelope of deep convection and cloudiness around 10,000 km in scale, with an eastward phase speed in the range of  $4\text{--}8 \text{ m s}^{-1}$  coupled to the large-scale circulation. The envelope is, in part, organized into CCEWs, along with a broad spectrum of MCSs. The MJO has been discussed extensively in the literature (see reviews by Madden and Julian [1994], Wang [2005], and Zhang [2005]) and so will not be treated here except with regards to its close connection to other CCEWs.

[9] More detailed spectral analysis of satellite tropical cloudiness data was undertaken by Gruber [1974], Zangvil [1975], and Zangvil and Yanai [1980, 1981], and these investigations began to more strongly suggest a connection between Matsuno's [1966] equatorial SW modes and deep convection. Although these studies provided ample evidence for the existence of convectively coupled ER, MRG, and Kelvin waves, detailed observational studies of them were not undertaken until the 1990s, although work on the MJO and dry stratospheric modes continued. Part of the impetus for the studies of the 1990s was no doubt the availability of long-period global satellite and operational data analyses, which provided regularly gridded fields suitable for identifying and tracking CCEWs. Using such data, Liebmann and Hendon [1990], Hendon and Liebmann [1991], and Takayabu and Nitta [1993] isolated the properties of convectively coupled MRG waves and showed that their vertical structures exhibited strong tilts with height in the lower and middle troposphere, much like the EWs studied by Reed and Recker [1971].

[10] While studying the detailed structure of the MJO, Nakazawa [1988] identified both eastward and westward propagating convective disturbances within the MJO envelope. These eastward propagating "superclusters" had a phase speed of around  $12\text{--}18 \text{ m s}^{-1}$ , and Takayabu and Murakami [1991] found that they were dominated by zonal wind perturbations in phase with their pressure field, consistent with the structure of Kelvin waves. At this point, there was enough empirical evidence available to support the idea that there were different species of Kelvin and MRG modes, some of which were relatively fast propagating dry modes primarily seen in the stratosphere, while others were more slowly propagating waves closely coupled to convection within the troposphere.

[11] Takayabu [1994a] performed a space-time spectral analysis of high-resolution geostationary satellite imagery and detected spectral peaks corresponding to Kelvin, ER, MRG, and WIG waves. By this time, dry WIG waves had already been observed and extensively studied as potential forcing mechanisms for the QBO [Tsuda *et al.*, 1994a, 1994b; Maruyama, 1994; Sato *et al.*, 1994], but the realization of WIG signals in cloudiness led to more extensive studies of these "2-day waves" in convection, which were prominent during the Tropical Ocean–Global Atmosphere Coupled Ocean–Atmosphere Response Experiment (TOGA COARE, hereinafter referred to as COARE) field experiment which took place over the western tropical Pacific during 1992–1993 [Takayabu, 1994b].

[12] Wheeler and Kiladis [1999] (hereinafter referred to as WK99) built on the work of Takayabu [1994a] by calculating a global space-time spectrum of a long record of tropical cloudiness. Figure 1 shows such a spectrum obtained by dividing the raw power in satellite brightness temperature by an estimate of its red noise background (see WK99 for details). Prominent spectral peaks are oriented along the dispersion curves of Matsuno's [1966] SW modes for a resting basic state (similar results are obtained using a more direct measure of satellite-derived rainfall [e.g., Cho *et*

**Figure 1**

*al.*, 2004]). Remarkably, the dispersion characteristics and structure of these CCEWs broadly correspond to those predicted by linear theory, even without considering the potential effects of the basic state flow and despite the potential for nonlinearities arising from coupling with convection. As will be discussed in more detail in section 2, the observed phase speeds of these waves are considerably slower than their dry counterparts because of this coupling. Recent studies have focused on reconciling the dynamical structures of observed CCEWs within a theoretical framework, which currently comprises a very active area of research in tropical meteorology and is the subject of this article.

## 2. THEORY OF CONVECTIVELY COUPLED EQUATORIAL WAVES

### 2.1. Shallow Water Theory

[13] As discussed in section 1, a portion of deep tropical convection appears to be controlled by dynamics consistent with Matsuno's [1966] SW theory. However, the applicability of classical SW theory to the observed CCEWs is by no means self-evident [e.g., Lindzen, 2003]. However, the fact that the observed waves display the dispersive properties derived from SW theory (Figure 1) suggests its usefulness as a place to start. Although it has been extensively covered elsewhere (see references given by Lindzen [2003] and Hoskins and Wang [2006]), here we touch upon some background theory useful for our later discussions of observed CCEWs, focusing on relevant points not previously emphasized in the literature.

[14] The SW equations govern the vertically independent motions of a single thin layer of incompressible, homogeneous density fluid on a rotating sphere, as also known as Laplace's tidal equations. The SW equations can be derived from the mathematical separation of the vertical versus horizontal and time-varying portions of the flow from the full primitive equations, although the assumptions required to perform this separation and derive the vertical dependence of motion are far from trivial.

[15] Matsuno [1966] considered inviscid SW equations that were linearized about a motionless basic state. The Coriolis parameter,  $f$ , was assumed to be linearly proportional to distance from the equator (i.e.,  $f = \beta y$ ), a suitably valid approximation for motions in the tropics. The equations are

$$\frac{\partial u_l}{\partial t} - \beta y v_l = -\frac{\partial \phi_l}{\partial x}, \quad (1)$$

$$\frac{\partial v_l}{\partial t} + \beta y u_l = -\frac{\partial \phi_l}{\partial y}, \quad (2)$$

$$\frac{\partial \phi_l}{\partial t} + g h_e \left( \frac{\partial u_l}{\partial x} + \frac{\partial v_l}{\partial y} \right) = 0. \quad (3)$$

Here  $u_l$  and  $v_l$  are the zonal and meridional velocities,  $\phi_l$  is the geopotential,  $g$  is the acceleration due to gravity, and  $h_e$  is the depth of the undisturbed layer of fluid. Equations (1) and (2) are the horizontal momentum equations, and (3) is a consequence of mass conservation, linking changes in the geopotential to the divergence. We use the subscript  $l$  to denote that in the context of the full three-dimensional atmospheric flow, these equations model the horizontal ( $x$  and  $y$ ) and time ( $t$ ) varying components of the flow only. That is, they govern the motions of a particular vertical mode,  $l$ , for which an appropriate choice of  $h_e$  must be made.

[16] Matsuno [1966] was the first to derive the complete set of zonally propagating wave solutions to these equations [see also Andrews *et al.*, 1987; Gill, 1982a; Pedlosky, 1987; Wheeler, 2002; Holton, 2004]. Briefly, one seeks zonally propagating wave solutions of the form

$$\begin{pmatrix} u_l \\ v_l \\ \phi_l \end{pmatrix} = \begin{pmatrix} \hat{u}(y) \\ \hat{v}(y) \\ \hat{\phi}(y) \end{pmatrix} \exp[i(kx - \omega t)], \quad (4)$$

where  $k$  is zonal wave number and  $\omega$  is frequency. Substitution and rearrangement yields a second-order differential equation in  $\hat{v}$  only:

$$\frac{d^2 \hat{v}}{dy^2} + \left( \frac{\omega^2}{gh_e} - k^2 - \frac{k}{\omega} \beta - \frac{\beta^2 y^2}{gh_e} \right) \hat{v} = 0. \quad (5)$$

Solutions to this equation that decay away from the equator are well known, from which it follows that the constant part of the coefficient in parentheses must satisfy

$$\frac{\sqrt{gh_e}}{\beta} \left( \frac{\omega^2}{gh_e} - k^2 - \frac{k}{\omega} \beta \right) = 2n + 1 \quad n = 0, 1, 2, \dots \quad (6)$$

This equation gives a relation between  $\omega$  and  $k$ , for each positive integer  $n$ , thus defining the horizontal dispersion relation for the waves. The equation is cubic in  $\omega$ , resulting in three classes of solutions corresponding to the EIG, WIG, and ER waves. Special consideration is required for the  $n = 0$  solution, corresponding to the MRG wave, and an additional solution to (1)–(3) not covered by (5) is the

**Figure 1.** Wave number–frequency power spectrum of the (a) symmetric and (b) antisymmetric component of Cloud Archive User Services (CLAUS)  $T_b$  for July 1983 to June 2005, summed from  $15^\circ\text{N}$  to  $15^\circ\text{S}$ , plotted as the ratio between raw  $T_b$  power and the power in a smoothed red noise background spectrum (see WK99 for details). Contour interval is 0.1, and contours and shading begin at 1.1, where the signal is significant at greater than the 95% level. Dispersion curves for the Kelvin,  $n = 1$  equatorial Rossby (ER),  $n = 1$  and  $n = 2$  westward inertio-gravity (WIG),  $n = 0$  eastward inertio-gravity (EIG), and mixed Rossby-gravity (MRG) waves are plotted for equivalent depths of 8, 12, 25, 50, and 90 m. Heavy solid boxes represent regions of wave number–frequency filtering (see section 3).

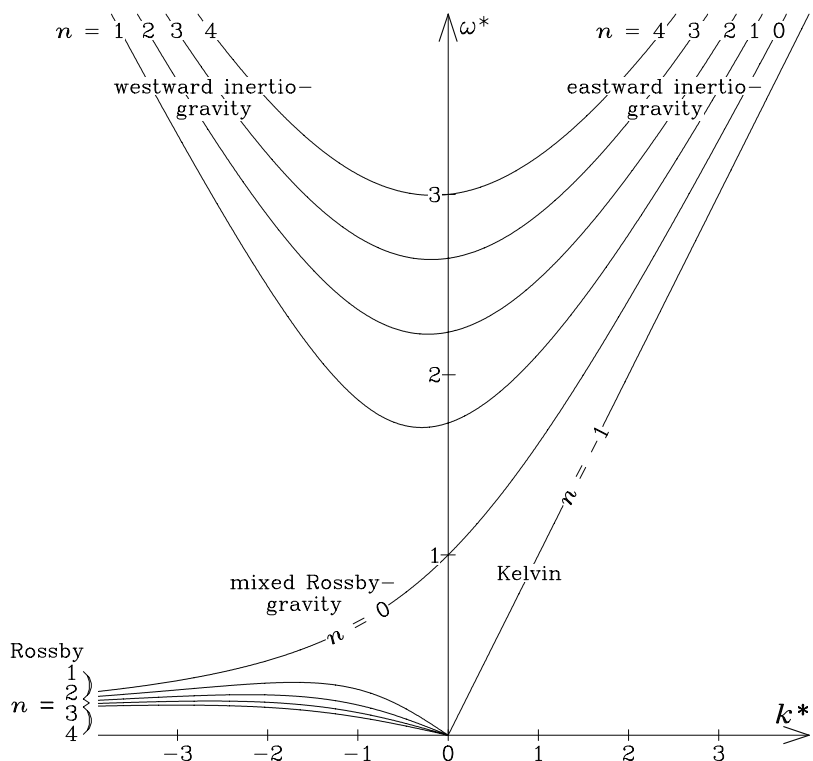


**Figure 2.** Dispersion curves for equatorial waves (up to  $n = 4$ ) as a function of the nondimensional frequency,  $\omega^*$ , and nondimensional zonal wave number,  $k^*$ , where  $\omega^* \equiv \omega/(\beta\sqrt{gh_e})^{1/2}$ , and  $k^* \equiv k(\sqrt{gh_e}/\beta)^{1/2}$ . For all but the Kelvin wave, these dispersion curves are solutions of equation (6). Westward propagating waves (relative to the zero basic state) appear on the left, and eastward propagating waves appear on the right. For consistency with equation (6), the Kelvin wave solution is labeled as  $n = -1$ .

Kelvin wave, for which  $\hat{v} = 0$  for all  $y$  and which is labeled as  $n = -1$  for consistency with (6). All the solutions to (6), plus the Kelvin wave dispersion relation, are presented in Figure 2.

[17] By substituting solutions for  $\hat{v}$  from (5) back into (1)–(3), one may obtain the full horizontal structures of the wave solutions. Figure 3 shows the full structures for the Kelvin wave,  $n = 1$  ER wave, MRG wave,  $n = 0$  EIG wave, and  $n = 1$  and  $n = 2$  WIG waves. As  $n$  corresponds to the number of nodes in the meridional profile of  $v$  (except for the Kelvin wave), it is called the meridional mode number. These six wave types include all those that have been observed as CCEWs. All other equatorial wave modes have considerably more complicated horizontal structures [Wheeler, 2002].

[18] Important characteristics of the wave solutions are as follows:

[19] 1. Since the original SW equations were linearized, any linear combination of the wave solutions is also a solution.

[20] 2. The phase speed of the Kelvin wave, a nondispersive wave, is  $c = \sqrt{gh_e}$ , and the phase speeds of all types of inertio-gravity waves, either eastward or westward, asymptotically approach this magnitude for large  $k$ .

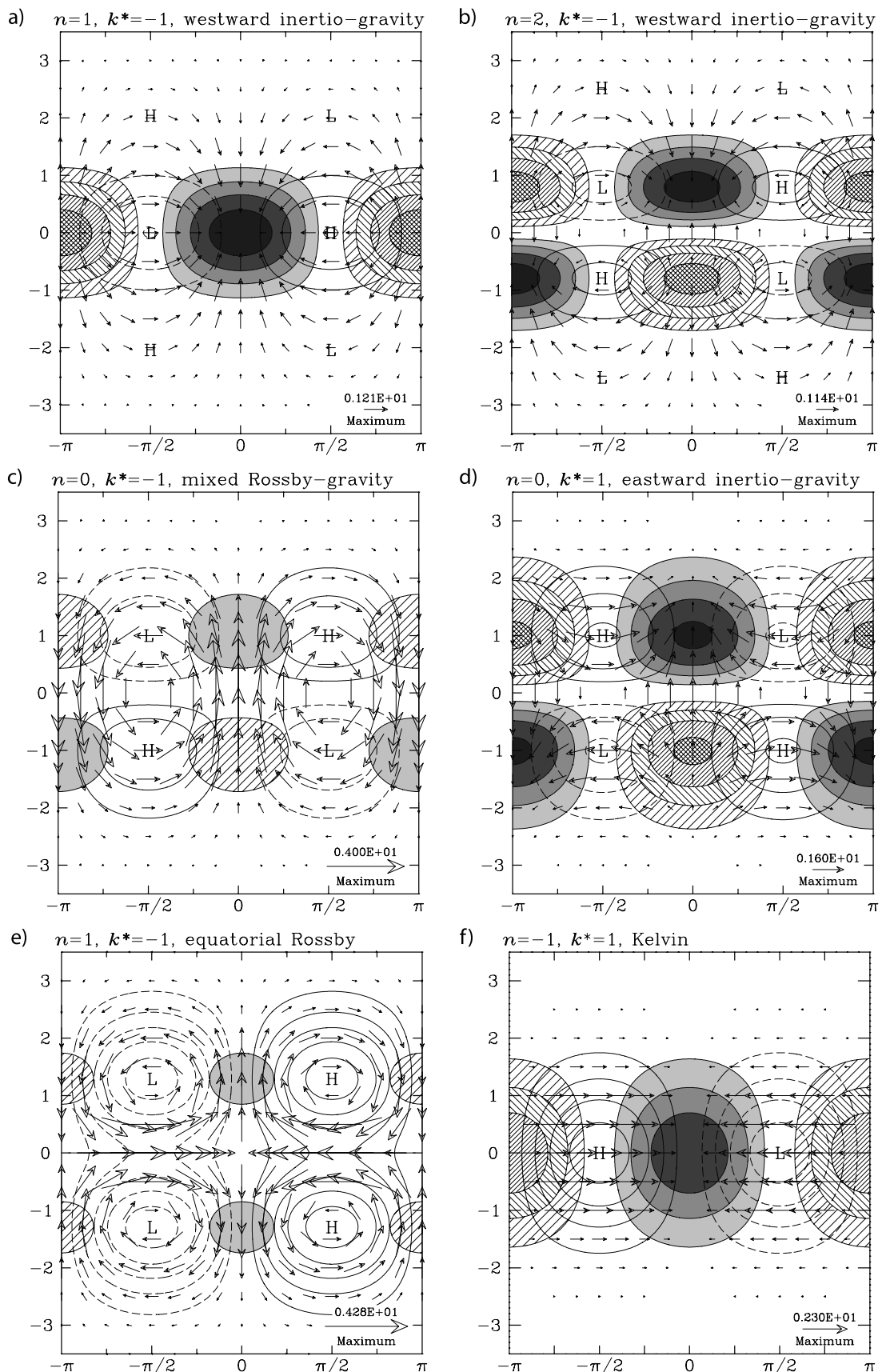
[21] 3. The equatorial *Rossby radius of deformation*, which governs the rate of decay of solutions with distance away from the equator, is given by  $R_e = (\sqrt{gh_e}/\beta)^{1/2}$  and has been used to scale the horizontal lengths in Figure 3. In practice,  $R_e$  is on the order of  $10^\circ$  of latitude for CCEWs (see Table 1).

[22] 4. The horizontal energy dispersion of waves is governed by the group velocity,  $c_g^{(x)} \equiv \partial\omega/\partial k$ , which may be estimated from Figure 2. The MRG wave, for example, has westward phase propagation ( $\omega/k$  is negative) but eastward energy dispersion ( $c_g^{(x)}$  is positive).

[23] 5. The inertio-gravity and Kelvin waves tend to be more divergent in character, whereas the MRG and ER waves are more rotational.

[24] 6. The SW depth  $h_e$  determines the speed and scale of the waves and for the purpose of modeling motions of the

**Figure 3.** Horizontal structures of a subset of the zonally propagating wave solutions to the shallow water equations on an equatorial  $\beta$  plane (equations (1)–(3)). Each is shown for a nondimensional zonal wave number,  $k^* = \pm 1$ . All scales and fields have been nondimensionalized by taking the units of time and length as given in the caption of Figure 2. The equator runs through the center of each diagram. Hatching is for divergence, and shading is for convergence, with a 0.6 unit interval between successive levels. Unshaded contours are geopotential, with a contour interval of 0.5 units. Negative contours are dashed, and the zero contour is omitted. The maximum wind vectors in each panel are specified in the bottom right corner.

**Figure 3**

**TABLE 1.** Vertical Structure Values for Dry Waves in a Constant  $N$  Atmosphere<sup>a</sup>

$h_e$	$L_z$ (km)	$\sqrt{gh_e}$ (m s $^{-1}$ )	$R_e$ (Degrees Latitude)
$H = 7.3 \text{ km}, dT_0/dz = -7.0 \text{ K km}^{-1}$ ( <i>Troposphere</i> )			
10	6.0	9.9	6.0
20	8.5	14.0	7.1
50	13.4	22.1	9.0
100	19.2	31.3	10.7
200	27.9	44.3	12.7
500	47.5	70.0	15.9
$H = 6.1 \text{ km}, dT_0/dz = +2.5 \text{ K km}^{-1}$ ( <i>Lower Stratosphere</i> )			
10	2.6	9.9	6.0
20	3.7	14.0	7.1
50	5.8	22.1	9.0
100	8.3	31.3	10.7
200	11.8	44.3	12.7
500	18.9	70.0	15.9

<sup>a</sup>As calculated from equation (17).

full atmosphere is called the “equivalent depth.” In the context of the real atmosphere, however, in no way should the equivalent depth be thought of as a physical depth but as an important parameter of the theory, as discussed further in section 2.2.1.

## 2.2. Relating Shallow Water Equations to Equations of Atmospheric Motion

[25] While the applicability of SW theory to CCEWs is evident, there is neither a unique nor a standard way to relate the full three-dimensional equations of atmospheric motion to the SW equations of motion, especially when circulations are forced by or coupled to convective heating. Rather, there are multiple ways to derive such a relation, which differ in the choice of vertical structure and the manner in which diabatic effects are included. Here we summarize several possibilities and note the impacts of the different choices on the corresponding theoretical dispersive properties and wave structures.

### 2.2.1. Dry Waves

[26] When the effects of moisture are neglected, and, in particular, the heating and cooling due to condensation and evaporation, it is relatively straightforward to derive solutions for atmospheric waves whose horizontal structures are governed by SW equations. Consider the hydrostatic primitive equations with the log pressure vertical coordinate  $z$  [e.g., Holton, 2004, p. 317], linearized about a motionless basic state:

$$\frac{\partial u}{\partial t} - fv + \frac{\partial \phi}{\partial x} = 0, \quad (7)$$

$$\frac{\partial v}{\partial t} + fu + \frac{\partial \phi}{\partial y} = 0, \quad (8)$$

$$\frac{\partial u}{\partial x} + \frac{\partial v}{\partial y} + \rho_0^{-1} \frac{\partial(\rho_0 w)}{\partial z} = 0, \quad (9)$$

$$\frac{\partial}{\partial t} \left( \frac{\partial \phi}{\partial z} \right) + wN^2 = 0, \quad (10)$$

where  $z = -H \log(p/p_s)$ ,  $p$  is pressure, the subscript  $s$  denotes fixed surface values,  $w$  is the vertical velocity,  $H = RT_m/g$  is the scale height for a layer mean temperature  $T_m$ ,  $R$  is the gas constant,  $\rho_0(z) = \rho_s \exp(-z/H)$ ,  $N^2 = (R/H)(dT_0/dz + g/c_p)$  is a measure of the static stability where  $dT_0/dz$  is an average lapse rate, and  $c_p$  is the specific heat of dry air at constant pressure. For simplicity we assume  $N^2$  is constant, and we neglect heating and frictional effects. Combining (9) and (10) to eliminate  $w$ ,

$$\frac{\partial}{\partial t} L[\phi] - N^2 \left( \frac{\partial u}{\partial x} + \frac{\partial v}{\partial y} \right) = 0, \quad (11)$$

where  $L = (1/\rho_0)(\partial/\partial z)(\rho_0)(\partial/\partial z)$  is a linear operator. Now assume that  $\phi$  has a vertical structure,  $\phi_v$ , that is an eigenfunction of  $L$ ; that is,

$$L[\phi_v] = -\lambda \phi_v, \quad (12)$$

where  $\lambda$  is a constant. Then (11) becomes

$$\frac{\partial \phi}{\partial t} + \frac{N^2}{\lambda} \left( \frac{\partial u}{\partial x} + \frac{\partial v}{\partial y} \right) = 0. \quad (13)$$

Note that (7), (8), and (13) are algebraically equivalent to the SW equations (1)–(3) with an equivalent depth of

$$h_e = N^2/(g\lambda) \quad (14)$$

and that this equivalence is independent of the method of approximating the Coriolis parameter by an  $f$  plane or  $\beta$  plane. Therefore, we can construct solutions to (7)–(10) whose horizontal structures come from solutions to the SW equations and whose vertical structures are derived from eigenfunctions of  $L$ . We might expect such solutions to provide insights about the structures and dispersive properties of observed CCEWs. However, the first complication is that even for dry waves, there are two fundamentally different types of vertical structures that are eigenfunctions of  $L$ :

$$\exp(z/2H) \exp(imz) \quad (15a)$$

or

$$\exp(z/2H) \sin(mz + b), \quad (15b)$$

where  $m$  is a vertical wave number and  $b$  is the phase (a constant). The first structure (15a) is for a *radiation upper boundary condition* [Lindzen, 1974, 2003], while (15b) is for a rigid lid at the upper boundary [see Haertel et al., 2008]. The real parts of these choices are essentially the same: sinusoidal functions that increase in amplitude with height. However, their different imaginary parts lead to different wave structures when the vertical structure is

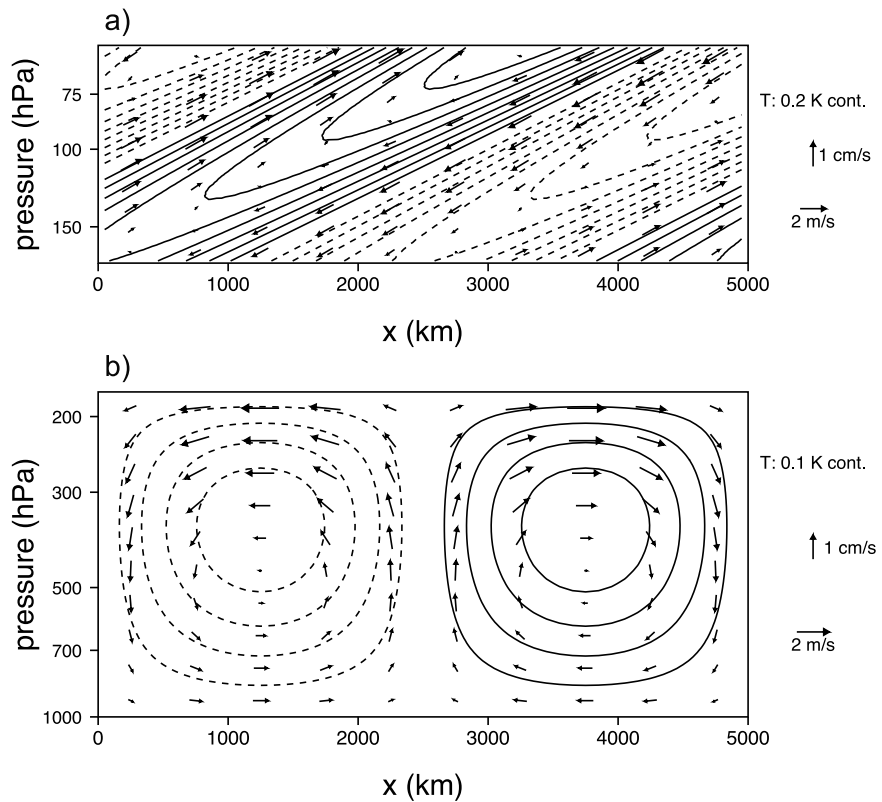


**Figure 4.** Zonal-vertical cross sections of Kelvin wave zonal and vertical wind (vectors) and temperature (contours) constructed by using a vertical structure function corresponding to (a)  $\exp(z/2H)\cos(mz + kx)$  and (b)  $\exp(z/2H)\sin(mz + b)\cos(kx)$ . Contour interval is 0.1 K, and vectors are scaled to the values shown to the right of each plot.

multiplied by a horizontal structure with an imaginary component. For example, for a wave with a horizontal structure given by equation (4), the real parts of the zonal and vertical structure would be as follows:

$$\exp(z/2H) \cos(mz + kx), \quad (16a)$$

$$\exp(z/2H) \sin(mz + b) \cos(kx). \quad (16b)$$

Figure 4 shows dry atmospheric Kelvin waves for both the (15a) and (15b) vertical structures. For the latter (Figure 4b), temperature perturbations exhibit localized maxima and minima, but for the former (Figure 4a), perturbations are slanted ridges and troughs. As shown in sections 4–8, CCEW dynamical structures resemble the  $\exp(z/2H)\sin(mz + b)$  structure in the troposphere and the vertically radiating  $\exp(z/2H)\exp(imz)$  structure in the stratosphere. Note that the waves shown in Figure 4 are constructed using a single vertical structure function, or vertical mode, and a single horizontal mode (the Kelvin wave), but in general, solutions to (7)–(10) consist of superpositions of such waves and comprise multiple vertical and horizontal modes (section 11).

[27] The relation between the vertical wavelength of the modes and the equivalent depth  $h_e$  of the corresponding SW system is a topic that is particularly relevant here. In an atmosphere with a constant stability parameter  $N$ , vertical

modes are sinusoidal in  $z$ , with corrections for the density variation with height. For example, by combining (12), (14), (15a), and (15b) one obtains

$$m \equiv \frac{2\pi}{L_z} = \left( \frac{N^2}{gh_e} - \frac{1}{4H^2} \right)^{1/2}, \quad (17)$$

where  $L_z$  is the vertical wavelength. In a realistic stratification, however, the modes are only quasi-sinusoidal, with a local vertical wavelength that is small in regions of large  $N$  (such as in the stratosphere) and larger in regions of low  $N$  (such as in the troposphere [Fulton and Schubert, 1985]). Example values of the local vertical wavelength corresponding to a given  $h_e$  are presented in Table 1 for two different representative stratifications.

[28] Table 1 may be used to understand the wavelengths seen in the lower stratosphere above the convective heating of CCEWs. Given a forced, steady state response to a moving heat source, the vertical wavelength above the heating will be set by the equivalent depth that best matches the horizontal movement of the source, with slower moving sources of the same horizontal structure producing a resonant response with a smaller vertical wavelength. This information also provides estimates of the scale of vertical modes radiated outward by the transient latent heating of a typical isolated convective storm (i.e., a disturbance that projects onto all horizontal wave numbers and frequencies).

If the convective heating extends up to near the tropopause (i.e., near 14 km) with greatest magnitude in the midtroposphere (i.e., near 7 km), then this heating will project most strongly onto the vertical mode with a half-wavelength of 14 km in the troposphere, or  $h_e = 200$  m, which is known as the “peak projection response” [Salby and Garcia, 1987]. An atmosphere forced with a random distribution of such deep tropospheric heating events would thus preferentially select equatorial waves with this equivalent depth, corresponding to a gravity wave speed in the range of 44–53 m s<sup>-1</sup> [Garcia and Salby, 1987; Mapes and Houze, 1995; Haertel and Kiladis, 2004]. Indeed, dry Kelvin waves with this scaling are observed [e.g., Hendon and Wheeler, 2008]. By contrast, the CCEWs display the horizontal dispersive characteristics of much shallower equivalent depths (12–50 m, Figure 1) and correspondingly slower speeds. Explaining this mismatch between the implied equivalent depth of the CCEWs and that of the most energetically forced waves in a dry atmosphere with realistic stratification has become one of the major challenges for the theory of CCEWs.

### 2.2.2. Moist Waves

[29] There are many ways to include the effects of moisture in theoretical treatments of equatorial waves; thus, a complete discussion is beyond the scope of this article. Here we simply address the question, Can the inclusion of condensational heating and cooling explain the discrepancy between the observed equivalent depths of CCEWs and those of dry waves with similar tropospheric vertical structures? An inspection of (10) provides an answer to this question. First, suppose that a diabatic forcing term,  $Q$ , had been included in this equation (keeping in mind that  $\partial\phi/\partial z$  is proportional to the temperature perturbation):

$$\frac{\partial}{\partial t} \left( \frac{\partial\phi}{\partial z} \right) + wN^2 = Q. \quad (18)$$

Furthermore, suppose that heating perturbations are proportional to upward motion perturbations, i.e., that  $Q = \alpha wN^2$  (where  $\alpha$  is an arbitrary constant), an idea that has observational support [Haertel and Kiladis, 2004; Haertel et al., 2008]. Then (18) becomes

$$\frac{\partial}{\partial t} \left( \frac{\partial\phi}{\partial z} \right) + w(1 - \alpha)N^2 = 0. \quad (19)$$

In this case, the heating effectively reduces the stability of the atmosphere. If  $\alpha$  were close to but just less than 1 (i.e., perturbation condensational heating/cooling canceled most but not all of the temperature change due to vertical motion), then the “effective static stability” of the atmosphere could be reduced enough to bring theoretical predictions of waves’ equivalent depths in line with those observed for CCEWs [Gill, 1982b]. The problem of explaining the equivalent depth of CCEWs is reduced to determining a theoretical value for  $\alpha$ , which can be accomplished for the first baroclinic mode (i.e., the mode with a half vertical wavelength in the troposphere) by using

a gross moist stability concept [Neelin and Held, 1987; Emanuel et al., 1994; Yu et al., 1998; Haertel and Kiladis, 2004], which is essentially the reduced stability that the large-scale atmosphere “feels” because of convective heating and cooling. However, there are still important discrepancies between the vertical structures of such moist waves and the observed vertical structures of CCEWs. We return to this question in section 11, using observations of CCEWs to evaluate the various theories that could explain their observed equivalent depths.

## 3. DATA SETS AND METHODOLOGY

[30] Given the limitations of in situ observations over the tropics, satellite data sets have been a crucial aid in objectively determining the location and strength of deep tropical convection. The most utilized data set for this purpose has been the interpolated NOAA-produced outgoing longwave radiation (OLR) product [Liebmann and Smith, 1996]. OLR has long served as an excellent statistical proxy for tropical convection, and it has a nearly continuous record back to 1974. However, its resolution is much lower than the recently available Cloud Archive User Services (CLAUS) data set, which utilizes geostationary and polar-orbiting images to produce a global grid of brightness temperature ( $T_b$ ) at an 8 times daily resolution of 0.5°, with very little missing data within the tropics [see Hodies et al., 2000]. We use CLAUS data extending from 1 July 1983 through 30 September 2005 to represent deep convection.

[31] Reanalysis data are commonly used to isolate the dynamical fields associated with atmospheric disturbances. Reanalysis blends observational and first-guess model data to estimate the state of the atmosphere at a particular time. While reanalysis effectively captures the observed large-scale features of the CCEWs, the use of radiosonde data is crucial for isolating more subtle details that may be important to wave dynamics. The European Centre for Medium-Range Weather Forecasts reanalysis (ERA-40 [Uppala et al., 2005]) pressure level data set is used here, on a 2.5° latitude/longitude grid, with four times daily observations that match the CLAUS data availability at 0000, 0600, 1200, and 1800 UT. Twice daily radiosonde soundings from the Comprehensive Aerological Reference Data Set [Eskridge et al., 1995], interpolated to 50 hPa vertical resolution at two Micronesian Island stations, are used to isolate the vertical structures of CCEWs, along with corrected radiosonde soundings from COARE [Ciesielski et al., 2003].

[32] To isolate propagating signals of satellite cloudiness corresponding to CCEWs, space-time filtering of OLR or  $T_b$  is frequently employed (WK99). This is generally accomplished in the wave number–frequency domain by retaining only those spectral coefficients within a specified range corresponding to the spectral peaks associated with a given mode. Figure 1 shows the spectral regions used for filtering to obtain the results shown in this article. This filtering is applied to raw data, without first decomposing into symmetric and antisymmetric components about the equator,

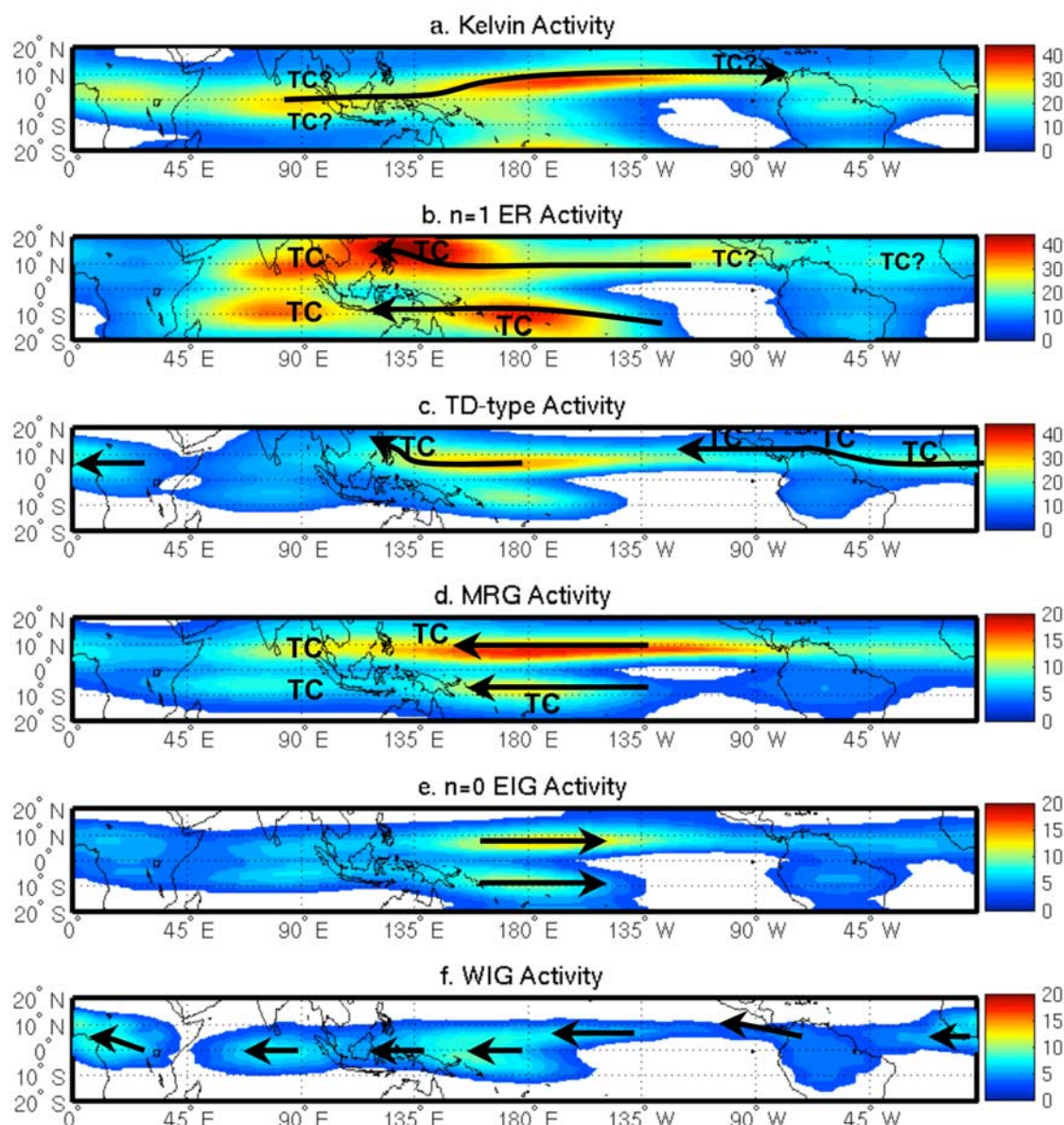


**Figure 5.** Distribution of annual mean variance of CLAUS  $T_b$  filtered for the (a) Kelvin, (b)  $n = 1$  ER, (c) tropical depression (TD), (d) MRG, (e)  $n = 0$  EIG, and (f) WIG bands. Also shown are preferred direction of propagation and preferred location of tropical cyclone (TC) genesis associated with each mode.

since this retains the full signal of the wave in those regions where convection is confined to one hemisphere and thus projects equally onto each component [see Straub and Kiladis, 2002]. The filters shown in Figure 1 are based on more expanded space-time domains than used by WK99 (except for the EIG wave), which better match the spectral peaks in Figure 1. The “TD-type” filter used to isolate EWs is not shown but is identical to that used by Kiladis et al. [2006] to encompass the prominent 2–6 day westward spectral peak found during northern summer (WK99). Figure 5 shows the distribution of  $T_b$  variance for the various CCEWs, along with some information on their propagation and impacts, to be discussed further in sections 4–8. These patterns compare well with those estimated

using OLR by WK99, Wheeler et al. [2000] (hereinafter referred to as WKW00), and Roundy and Frank [2004a].

[33] The space-time filtered  $T_b$  of a particular CCEW at a given grid point is correlated and regressed against unfiltered dynamical and  $T_b$  fields to obtain a “composite” picture of the wave’s evolution. This technique is similar to that used by WKW00 except that we do not window by wave activity amplitude but instead use the entire period available regardless of season. General features of the results are not sensitive to the details of this approach. For all of the plots in this article, the perturbations are scaled to a  $-20\text{ K}$   $T_b$  anomaly at the chosen base grid point, a typical minimum value seen during the convective phase of a moderately strong wave event. Positive/negative lags refer

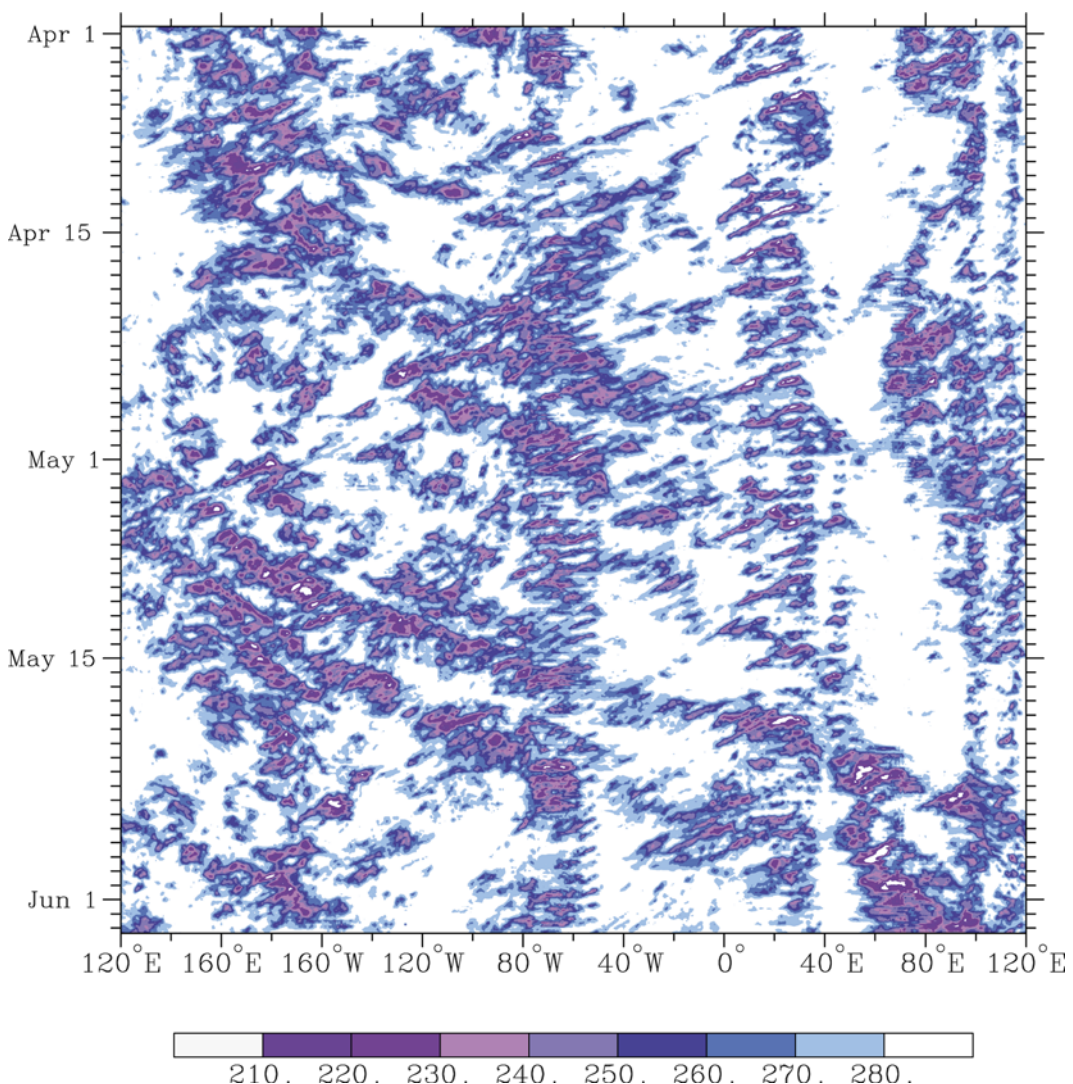


**Figure 6.** Time-longitude section of CLAUS brightness temperature  $T_b$ , averaged from 2.5°S to 7.5°N, from 1 April through 2 June 1987.  $T_b$  shading scale is shown at the bottom in °K.

to times after/before the peak in convection (negative  $T_b$  anomaly) at the base point. Features discussed here are all locally statistically significant at better than the 95% level, after taking into account temporal autocorrelation, and every pattern shown is field significant according to the criteria outlined by Livezey and Chen [1983].

#### 4. KELVIN WAVES

##### 4.1. Observed Structure

[34] In early satellite studies of CCEWs [Wallace and Chang, 1972; Zangvil, 1975], a distinction was made between relatively fast eastward propagating waves and the slower, larger-scale MJO, which concentrates the majority of its spectral power at eastward zonal wave numbers 1 and 2 (Figure 1a). As higher-resolution satellite observations and global model data became available, more detailed observations of fast eastward waves were collected, motivated in particular by their interaction with the MJO. For example, Nakazawa [1986, 1988] identified a hierarchical

structure within the MJO in which “short-period synoptic-scale active convective cells,” now identified as Kelvin waves, comprise a substantial portion of cloudiness within the MJO itself. These “superclusters” had horizontal scales of 3300–6600 km, time scales of <10 days, and eastward phase speeds of 15–20 m s<sup>-1</sup> over the west Pacific. The Kelvin waves were themselves made up of even higher-frequency westward moving disturbances (or “cloud clusters”), some of which are now known to be inertio-gravity modes (see section 5). Later studies showed that Kelvin waves typically propagate more slowly over the Indian Ocean (12–15 m s<sup>-1</sup>) than other regions [Yang *et al.*, 2007b] and more slowly, more frequently, and with higher amplitude through the active convective phase of the MJO [Dunkerton and Crum, 1995; Roundy, 2008].

[35] To illustrate the complexity of cloudiness signals associated with Kelvin waves, Figure 6 shows CLAUS  $T_b$  averaged over 2.5°S–7.5°N during April–May 1987. A wide variety of eastward moving cloudiness envelopes are visible, ranging from large-scale features that propagate

around the globe to much smaller disturbances lasting only a few hours. Figure 6 confirms the tendency for these waves to move more slowly over the Eastern Hemisphere than other regions and their ability to propagate unimpeded over the 3000 m barrier of the Andes from the Pacific into South America. Within the eastward moving envelopes, smaller-scale cloud clusters move westward, sometimes associated with an obvious modulation of the diurnal cycle, as is evident over the Atlantic sector. Although some of this westward propagation can be accounted for by an easterly basic state, in many cases the westward phase speeds are too fast to be explained by simple advection and can be attributed to WIG or other wave types (see section 5). Observations of the hierarchical wave-like nature of tropical cloudiness are ubiquitous in studies using high-resolution data sets [Hendon and Liebmann, 1994; Chen et al., 1996; Straub and Kiladis, 2002, 2003b; Straub et al., 2006].

[36] Cloudiness variations associated with Kelvin waves peak along the latitude of the climatological ITCZ, which is generally confined between the equator and 10°N over the central Pacific, eastern Pacific, and Atlantic basins (Figure 5a) and varies more substantially with season over Africa, the Indian Ocean, and South America [Roundy and Frank, 2004a]. While the precise relationships between cloudiness and the dynamical and thermodynamical fields in Kelvin waves depend on location [see Yang et al., 2007a], the general features presented here are typical regardless of region or season.

[37] To a large degree, the horizontal dynamical structure of observed Kelvin waves is remarkably similar to its corresponding SW mode. Figure 7 shows the composite  $T_b$  (shading), geopotential height (contours), and winds (vectors) for a Kelvin wave over the central Pacific at 850 and 200 hPa, obtained by regressing these fields onto Kelvin-filtered  $T_b$  using the methodology outlined in section 3. Note the predominantly zonal wind near the equator, the latitudinal symmetry of the height and wind fields about the equator, and the in-phase relationship between height and wind, all predicted by theory (Figure 3f). Winds at 850 hPa are easterly to the east of low  $T_b$  and westerly to its west, with maximum zonal convergence at this level located a few hundred kilometers to the east of the  $T_b$  minimum, as also shown by Takayabu and Murakami [1991] and Straub and Kiladis [2002, 2003c]. At this level and location, the contribution of meridional flow to the divergence is negligible, although its magnitude does depend on whether the Kelvin wave is propagating through an active MJO [Roundy, 2008].

[38] The day +2 pattern in Figure 7b shows that the entire composite pattern propagates eastward at roughly 15 m s<sup>-1</sup>. While the circulation field remains nearly symmetric about the equator, the  $T_b$  signal is substantially asymmetric, since equatorial sea surface temperature is normally too cold to support deep convection over the eastern Pacific. At later lags the  $T_b$  signal farther east lies entirely north of the equator within the ITCZ, until the wave reaches South America and interacts with Amazonian convection (not shown).

[39] In the upper troposphere, the height and wind fields associated with a Kelvin wave are opposite to those in the lower troposphere (Figure 7c), with a few minor but important differences. Heights are high to the east of the lowest  $T_b$  and low to the west and symmetric with respect to the equator. Equatorial zonal flow is still in phase with the pressure field, but now there is also meridional mass outflow away from and toward the equator, giving rise to significant ageostrophic circulations. These differences from Figure 3f highlight the fact that in the real atmosphere, there are some substantial deviations from the circulations expected in SW theory [Chao, 2007]. The pressure patterns in Figure 7 correspond to a wavelength of around 10,000 km for the composite Kelvin wave, although it is important to bear in mind that much shorter Kelvin waves are often observed, as seen in Figure 6.

[40] The typical vertical structure of a Kelvin wave is illustrated with time-height cross sections of composite 12 hourly radiosonde data. Figure 8 shows the regressed  $T_b$ , zonal wind, temperature, and humidity anomalies for Kelvin waves in the central Pacific, at the island of Majuro (7.1°N, 171.4°E). The time axis in these cross sections runs from right to left so that these plots can also be viewed as longitude-height cross sections for eastward propagation. The tropospheric structure below 150 hPa of wind (Figure 8a) and temperature (Figure 8b) grossly resembles a vertical stacking of the theoretical structure in Figure 4b corresponding to equation (16b), while above this it is more like the vertically radiating, tilted solution in Figure 4a corresponding to equation (16a).

[41] The zonal wind-height cross section, shown in Figure 8a, confirms the reanalysis-derived wind anomalies shown in Figure 7, with lower tropospheric easterly perturbations transitioning to westerlies 12 h before the lowest  $T_b$ , with maximum zonal convergence to the east of the deepest convection, while maximum upper tropospheric zonal divergence is collocated with the low  $T_b$  itself. This phasing varies substantially in the vertical, however, because of the strong westward tilts with height in the lower troposphere and eastward tilts in the upper troposphere and lower stratosphere.

[42] The temperature (Figure 8b) and specific humidity (Figure 8c) cross sections reveal important clues to the thermodynamics of the Kelvin wave. Beginning 2 days before the time of the lowest  $T_b$ , lower tropospheric humidity increases substantially, first deepening slowly and then more rapidly increasing in vertical extent on day 0. Simultaneously, the lower troposphere warms, with a positive temperature anomaly appearing from the surface to around 500 hPa during day -2. Starting ~12 h prior to the lowest  $T_b$ , the lower troposphere rapidly dries and cools, while the upper troposphere remains moist and warm. The broad cold signal of the 850–500 hPa layer likely signifies adiabatic cooling due to vertical advection, while the separate cold and dry pool near the surface is consistent with convective downdrafts, which transport low moist entropy air from the midtroposphere into the boundary layer (see section 11). In addition, the near coincidence between the strongest upward

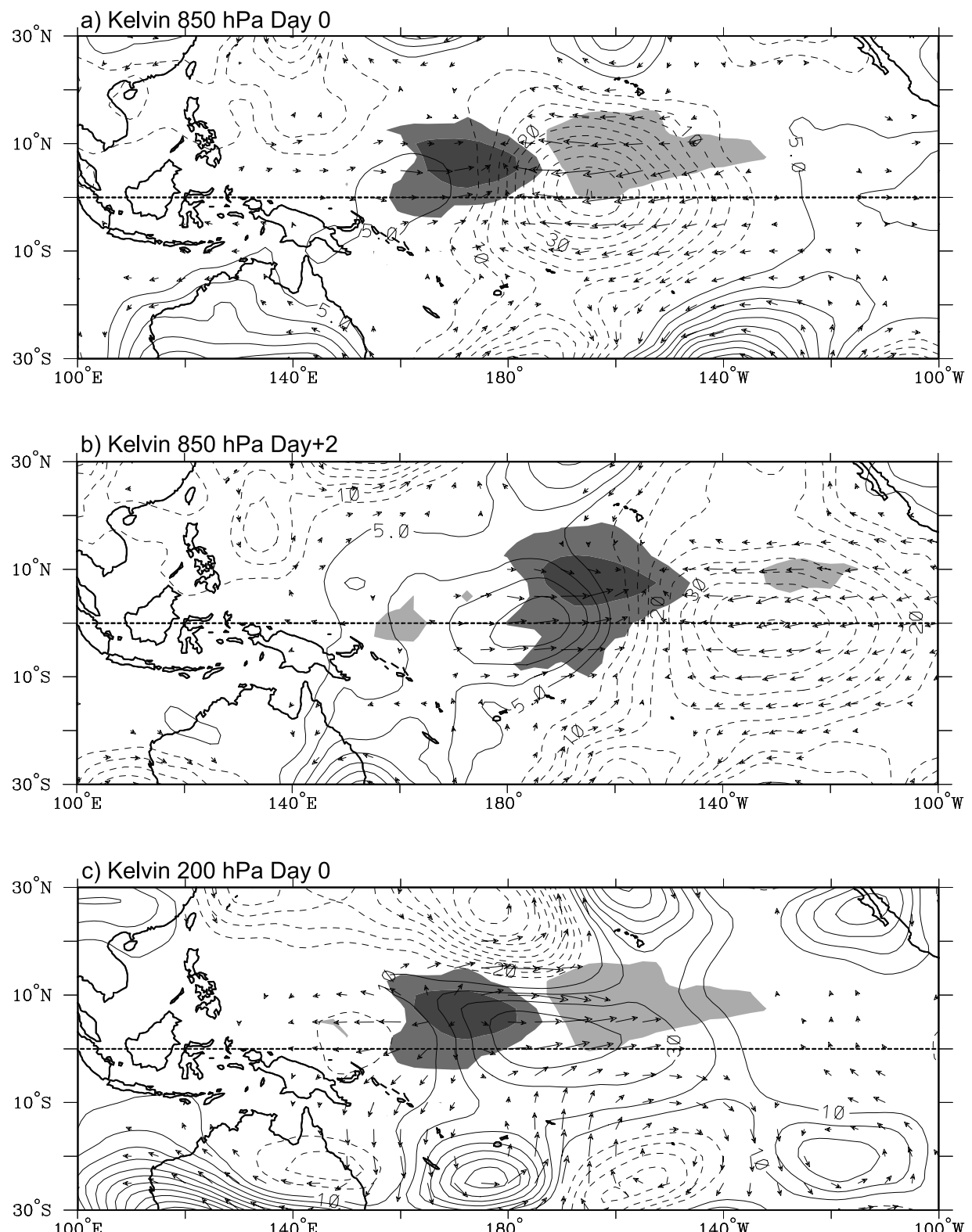


**Figure 7.** Maps of anomalous  $T_b$  (shading), geopotential height (contours), and wind (vectors) associated with a  $-20\text{ K}$  perturbation in Kelvin wave  $T_b$  at the base point  $7.5^\circ\text{N}$ ,  $172.5^\circ\text{E}$ , for (a) day 0 at 850 hPa, (b) day +2 at 850 hPa, and (c) day 0 at 200 hPa. The contour interval is 5 m in Figures 7a and 7b and 10 m in Figure 7c, with negative contours dashed. Dark (light) shading is for negative (positive)  $T_b$  perturbations of  $\pm 10\text{ K}$  and  $3\text{ K}$ .  $T_b$  and wind vectors are locally significant at the 95% level, with the largest vectors around  $2\text{ m s}^{-1}$ .

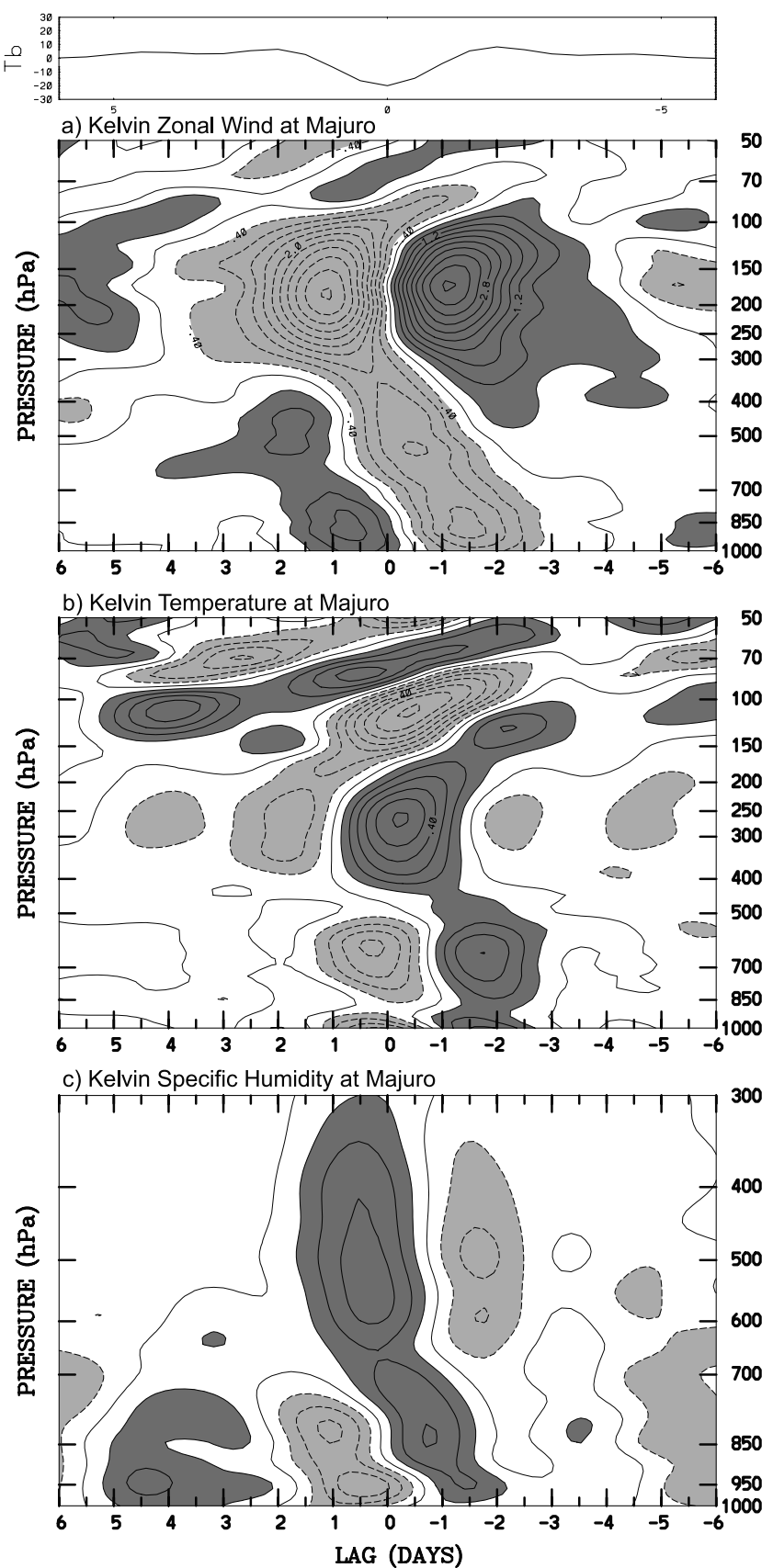


**Figure 8.** Time-height sections of anomalies of (a) zonal wind, (b) temperature, and (c) specific humidity at Majuro ( $7.1^{\circ}\text{N}$ ,  $171.4^{\circ}\text{E}$ ), scaled to a  $-20\text{ K}$  perturbation in Kelvin filtered  $T_b$  at the nearest grid point on day 0. Contour interval is  $0.4 \text{ m s}^{-1}$  for wind,  $0.1 \text{ K}$  for temperature, and  $0.1 \text{ g kg}^{-1}$  for specific humidity, with negative contours dashed. Dark shading represents positive perturbations. The associated  $T_b$  anomaly is shown at the top in  $^{\circ}\text{K}$ .

vertical motion field from reanalysis (not shown) and the positive upper troposphere temperature signal, both of which peak at 250 hPa 12 h prior to the lowest  $T_b$ , implies a positive correlation between the diabatic heating from deep convection and temperature, consistent with production of *available potential energy (APE)* and wave growth.

[43] The temperature and moisture evolution can also be linked to the morphology of cloudiness, which was shown by *Straub and Kiladis* [2002] to begin with shallow convection, progress to deep convection by day 0, and end with upper tropospheric cloud overlying a relatively cloud-free layer (i.e., stratiform cloudiness and precipitation [*Houze*, 2004]) after the main convective signal has passed. Thus, shallow convection initially moistens the lower troposphere; then, deep convection moistens the entire troposphere; and finally, stratiform cloudiness is associated with a moist upper troposphere and a dry lower troposphere. The latter is also cool because of the evaporation of stratiform precipitation in the low level dry air. This morphology is also consistent with the hierarchical structure of superclusters first proposed by *Nakazawa* [1988] and the percentage of deep convection derived from satellite data [e.g., *Kiladis et al.*, 2005, Figure 13].

[44] Divergence and vertical motion from reanalysis provides further evidence for the systematic evolution of cloudiness in the Kelvin wave. Low level convergence and associated upward motion begin near the surface  $\sim 10\text{--}15^\circ$  to the east of the lowest  $T_b$  [*Straub and Kiladis*, 2003a, 2003c], as expected theoretically because of surface frictional effects [*Wang*, 1988; *Wang and Rui*, 1990; *Moskowitz and Bretherton*, 2000]. Upward motion then extends through the entire troposphere where  $T_b$  reaches a minimum. Note that for a theoretical dry, internal Kelvin (or gravity) wave, midlevel temperature is in quadrature with vertical advection such that the coldest temperatures would be 1/4 phase to the west of the strongest upward motion, as in Figure 4b. The fact that positive upper tropospheric temperature anomalies are nearly in phase with the lowest  $T_b$  in Figure 8b reflects the importance of latent heating in determining the wave's temperature structure (section 11).

[45] While much of the tropospheric structure of convectively coupled Kelvin waves is complicated by the interaction between diabatic heating and vertical advection, the signal above the upper tropospheric change in tilt (or “elbow,” here at 250 hPa) in the dynamical fields is much simpler to interpret as a response to the upward propagation of wave energy generated by a moving tropospheric heat source. In the Kelvin wave, and indeed all other CCEWs examined here, the tropopause layer around 100 hPa in the region of deepest convection displays a strong cold signal. This has been interpreted as a hydrostatic response to the induced upward motion below, as opposed to being attributed to “overshooting” convective tops or radiative cooling [*Sherwood and Wahrlich*, 1999; *Holloway and Neelin*, 2007], although the downward propagation of this signal from the stratosphere at earlier lags is not completely consistent with that argument. The near-quadrature relationship between the stratospheric zonal wind and temperature

in Figures 8a and 8b matches that expected for an eastward propagating dry, internal, linear Kelvin or gravity wave (Figure 4a), with the tilt consistent with the upward propagation of wave energy induced by an eastward moving upper tropospheric heat source [*Lindzen*, 1967; *Lindzen and Matsuno*, 1968; *Andrews et al.*, 1987]. The vertical scale of these features is also consistent with linear theory discussed in section 2. The vertical wavelength of the stratospheric zonal wind and temperature signals in Figures 8a and 8b is  $\sim 5$  km, matching the theoretical value predicted by equation (17) and Table 1 for a realistic lower stratospheric stratification with zero mean wind and  $\sim 40$  m equivalent depth. However, we note that while CCEW signals are present in the lower stratosphere, overall, the spectrum there is dominated by dry waves, which, in general, have greater vertical wavelengths and group velocities, allowing for more efficient upward propagation [*Ern et al.*, 2008; *Hendon and Wheeler*, 2008].

#### 4.2. Initiation Mechanisms of Kelvin Waves

[46] Besides the triggering of new Kelvin wave events by preexisting equatorial convection, there is strong evidence that Kelvin waves can also be initiated through extratropical forcing. *Straub and Kiladis* [2003a] found that Kelvin wave convection originating over the western Pacific was preferentially preceded by extratropical Rossby wave train activity emanating out of the southern Indian Ocean storm track. *Liebmann et al.* [2009] present evidence that sea level “pressure surges” propagating from extratropical South America northward along the eastern slope of the Andes into the deep tropics often preceded Kelvin wave activity over the Amazon. They distinguished the frequent Kelvin waves propagating into South America from the Pacific, like those seen in Figure 6, from other waves originating over the Amazon from the pressure surges. Other evidence suggests that Kelvin wave activity can be forced indirectly by wave forcing within the extratropical storm track [*Yang et al.*, 2007c], through the direct projection of vorticity forcing onto the equatorial Kelvin structure, as discussed by *Hoskins and Yang* [2000]. An example of this potential forcing can be seen in Figure 7c, where a wave train in the Southern Hemisphere along  $20^\circ\text{S}$  is seen to move eastward in tandem with the equatorial Kelvin pressure pattern at lag [see *Straub and Kiladis*, 2003a, Figure 2].

#### 4.3. Impacts of Kelvin Waves

[47] Kelvin waves are known to interact strongly with the MJO [*Dunkerton and Crum*, 1995]. *Straub et al.* [2006] analyzed a case from May 1998, previously documented by *Takayabu et al.* [1999], where a Kelvin wave originating over South America propagated over Africa and then into the Indian Ocean, apparently triggering an MJO, which then spawned another Kelvin wave that continued eastward back to South America. This interaction was linked to the demise of the strong 1997–1998 El Niño event in these studies through the sudden increase of Pacific trade winds associated with the MJO. While the convective envelope of the MJO itself is frequently composed of Kelvin waves

[Masunaga, 2007; Roundy, 2008], statistically, this is most likely over the Indian sector, whereas Kelvin activity over the Pacific like that in Figure 6 is most common after the decay of the MJO over the west Pacific [see Straub and Kiladis, 2003b].

[48] Figure 5 shows that Kelvin waves have a notable influence on regions such as Indonesia [Wheeler and McBride, 2005; Murata et al., 2006], the Atlantic ITCZ [Wang and Fu, 2007], South America [Liebmann et al., 2009], and Africa [Mounier et al., 2007, 2008; Mekonnen et al., 2008; Nguyen and Duvel, 2008]. Straub et al. [2006] showed that Kelvin waves are frequently implicated in the onset of the summer monsoon over the South China Sea, as was also seen by Flatau et al. [2003] for onset over India and Mounier et al. [2008] for Africa. Recent analyses suggest that Kelvin waves apparently have a small but statistically significant influence on tropical cyclogenesis [Bessafi and Wheeler, 2006; Frank and Roundy, 2006], along with some evidence for a reverse relationship [Sobel and Camargo, 2005]. The meridional mass circulation of Kelvin waves is associated with the development of low level cyclonic and upper level anticyclonic gyres [Roundy, 2008]. Low level cyclonic gyres left behind over the eastern Indian Ocean after a Kelvin wave could potentially influence the development of tropical cyclones for up to several days.

## 5. THE $n = 1$ WESTWARD INERTIO-GRAVITY WAVES

[49] As discussed in section 1, large-scale westward propagating “cloud clusters” with periods of  $\sim 2$  days are frequently observed within the MJO envelope. These disturbances were first identified as  $n = 1$  WIG waves by Takayabu [1994b] and were particularly prominent during COARE [Chen et al., 1996; Schrage et al., 2001; Clayson et al., 2002]. The high spatial and temporal resolution data from COARE enabled WIG waves to be studied in great detail [Takayabu et al., 1996; Haertel and Johnson, 1998; Haertel and Kiladis, 2004; Haertel et al., 2008]. As might be expected from their close association with the MJO, WIG waves are most prominent over the Indian and Pacific Ocean warm pool regions (Figure 5f; WK99). We note that since WIG filtering is done for the space-time region shown in Figure 1a using both antisymmetric and symmetric components, this also includes the  $n = 2$  WIG wave which overlaps the spectral peak for the latter in Figure 1b. However, since we concentrate on equatorial convection, it turns out that the structures shown here resemble  $n = 1$  WIG waves (Figure 3a), with  $n = 2$  WIG waves (Figure 3b) isolated when using off-equatorial convection (not shown).

[50] The theoretical  $n = 1$  WIG (Figure 3a) has divergence maximized on the equator, in phase with antisymmetric meridional flow, and in quadrature with symmetric pressure and zonal wind. Figure 9 shows the composite  $n = 1$  WIG wave for a base point within the COARE study region at  $0^\circ$ ,  $155.0^\circ\text{E}$ . The observed structure is dominated by largely divergent flow branches arcing

toward or away from the equator connected to each other by off-equatorial zonal flow, matching the pressure and flow patterns predicted by theory quite well. At 850 hPa (Figures 9a and 9b) the  $T_b$  minimum is displaced well to the east of the theoretical and observed convergence minimum, while at 200 hPa, maximum divergence is nearly collocated with the implied deepest convection (Figure 9c).

[51] A wide range of scales has been reported for  $n = 1$  WIG waves, with phase speeds ranging from 10 to  $>30 \text{ m s}^{-1}$ . The composite wave in Figure 9 has a phase speed of around  $29 \text{ m s}^{-1}$ , with nearly opposite patterns from day  $-1$  to day 0 at 850 hPa, corresponding to a wavelength of around 5000 km (as found by WK00). This is almost twice the phase speed of the WIG waves observed during COARE, although those modes had wavelengths that were only half as large so that in both cases the periods are still very close to 2 days. The occurrence of WIG convection timed to the peak of the diurnal convective cycle every other day has led to speculation of a dependence on this diurnal phase locking, with a day required for the recovery of boundary layer moist entropy between events [Takayabu et al., 1996; Chen et al., 1996; Chen and Houze, 1997; Liebmann et al., 1997].

[52] Although long-period radiosonde data are not available for the COARE region, events were frequent enough during COARE that reasonable vertical structures can be obtained from the dense array of four times daily soundings taken during that experiment, using 1.5–3 day filtered  $T_b$  as a predictor [Haertel and Kiladis, 2004]. WIG waves (Figure 10) have opposite vertical tilts compared to Kelvin waves (Figure 8), as expected, with elbows at similar levels. Discontinuities in temperature at around 900 hPa are tied to amplified near-surface fluctuations, with cold surface anomalies during and just after the deepest convection. As with the Kelvin wave, the lowermost troposphere initially warms and moistens ahead of deep convection, then moisture is transported rapidly upward while the midtroposphere warms and the boundary layer cools and dries as  $T_b$  reaches a minimum.

[53] High-resolution COARE soundings allowed for the precise calculation of divergence and associated vertical motion, along with the “apparent heat source” (Q1 [Yanai et al., 1973]) due primarily to condensational heating [Ciesielski et al., 2003]. For composite COARE WIG waves, low level convergence peaks ahead of the deepest convection and rises with time (Figure 11a), yielding a tilted Q1 structure (Figure 11b), which shows heating peaking first at low levels, then maximizing at around 400 hPa just before the  $T_b$  minimum, and finally transitioning to heating over cooling behind the wave. As documented by Takayabu et al. [1996] and Haertel et al. [2008], the divergence and heating profiles are in accord with the evolution of cloudiness from shallow to deep and then stratiform, as in Kelvin waves.

[54] Haertel and Kiladis [2004] were able to reproduce the gross structure COARE WIG waves simply by forcing a linear primitive equation with their composite Q1 field moving at the observed phase speed, suggesting not only

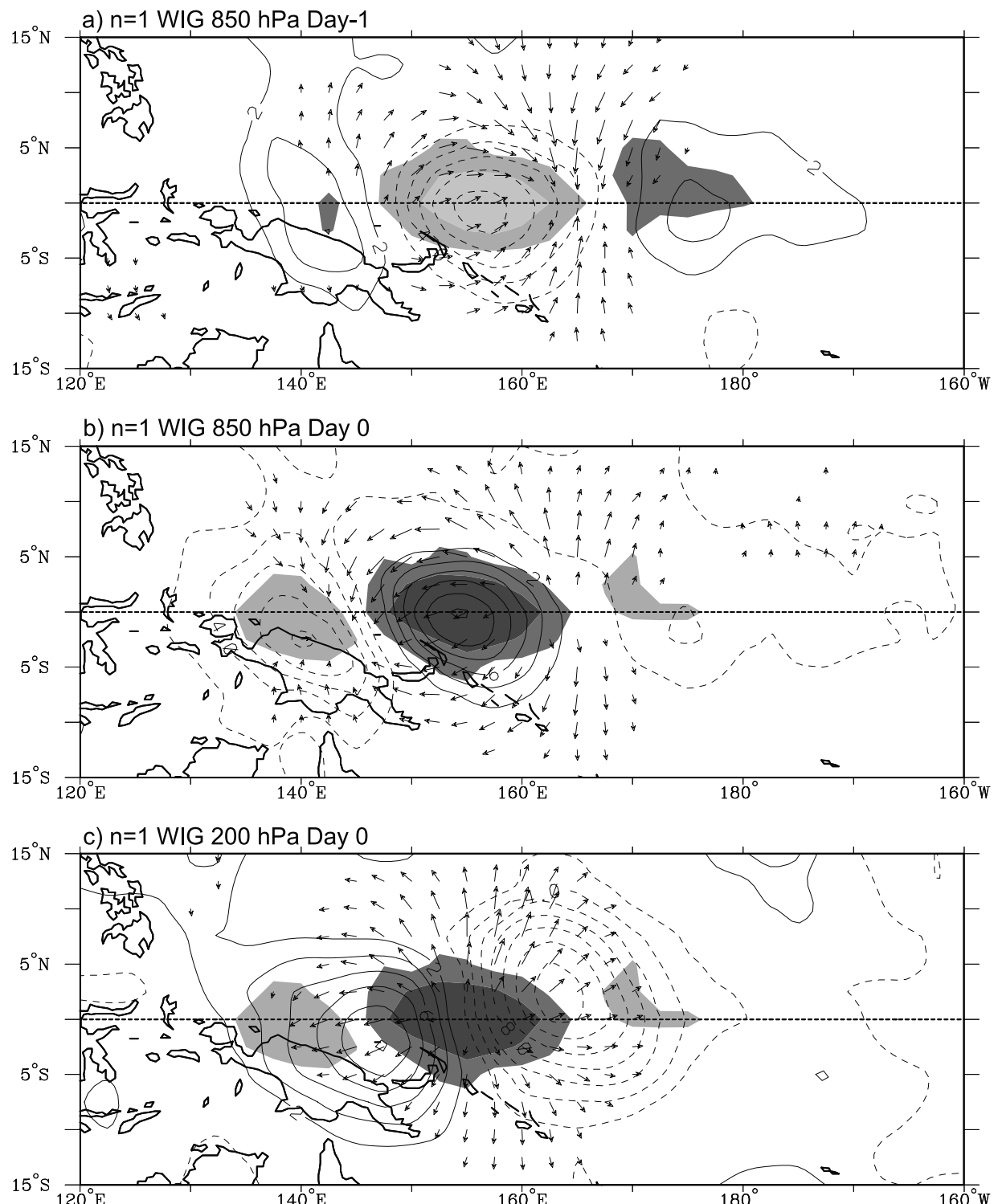


**Figure 9.** Maps of anomalous  $T_b$  (shading), geopotential height (contours), and wind (vectors) associated with a  $-20\text{ K}$  perturbation in  $n = 1$  WIG wave  $T_b$  at the base point  $0.0^\circ, 155^\circ\text{E}$ , for (a) day  $-1$  at 850 hPa, (b) day 0 at 850 hPa, and (c) day 0 at 200 hPa. The contour interval is 2 m, with negative contours dashed. Dark (light) shading is for negative (positive)  $T_b$  perturbations of  $\pm 10\text{ K}$  and  $3\text{ K}$ .  $T_b$  and wind vectors are locally significant at the 95% level, with the largest vectors around  $2\text{ m s}^{-1}$ .

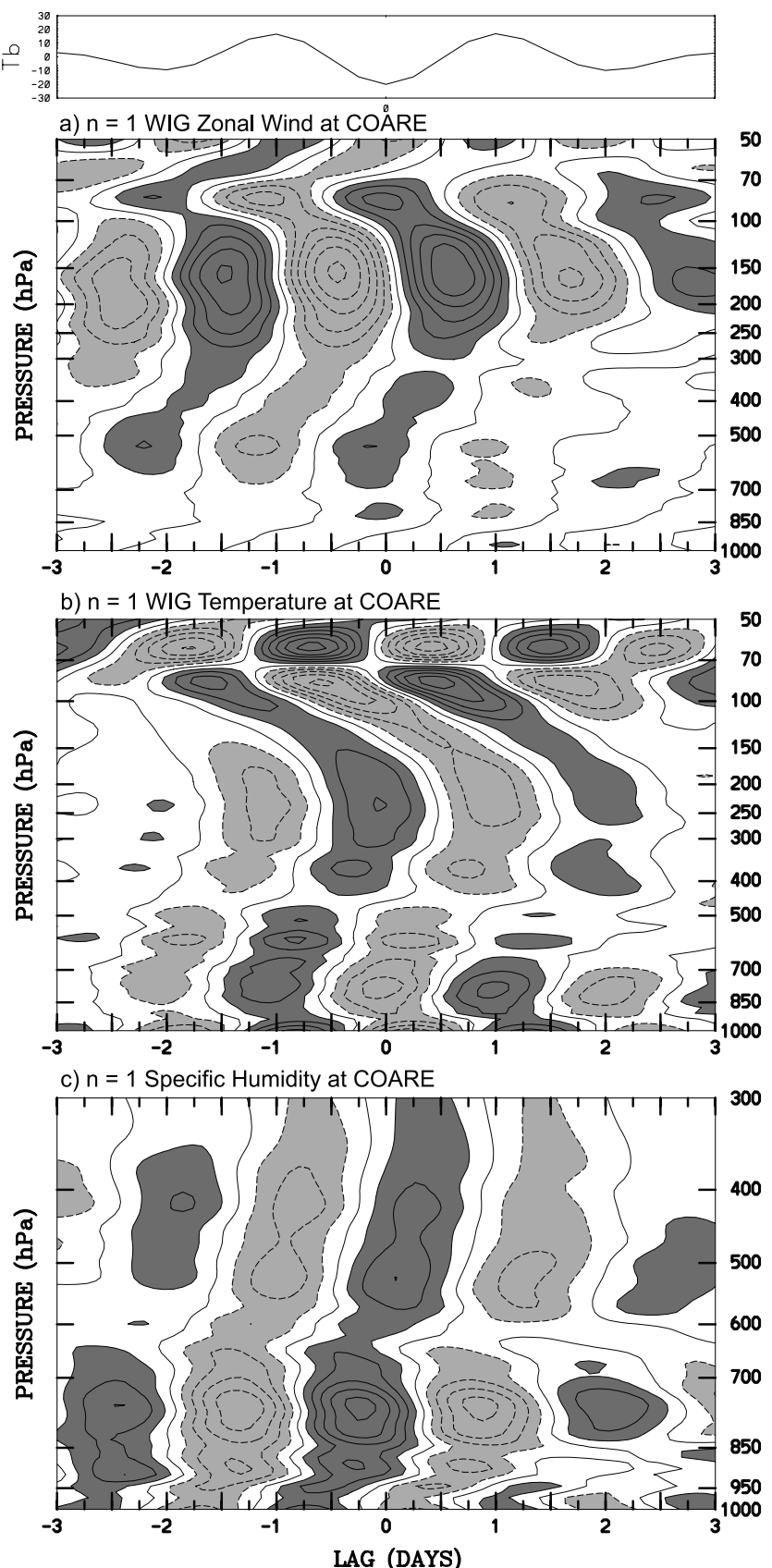


**Figure 10.** Time-height sections of anomalies of (a) zonal wind, (b) temperature, and (c) specific humidity within the COARE region centered on  $2.0^{\circ}\text{S}$ ,  $155.0^{\circ}\text{E}$ , scaled to a  $-20\text{ K}$  perturbation in  $n = 1$  WIG filtered  $T_b$  at the nearest grid point on day 0. Contour interval is  $0.4\text{ m s}^{-1}$  for wind,  $0.1\text{ K}$  for temperature, and  $0.1\text{ g kg}^{-1}$  for specific humidity, with negative contours dashed. Dark shading represents positive perturbations. The associated  $T_b$  anomaly is shown at the top in  $^{\circ}\text{K}$ .

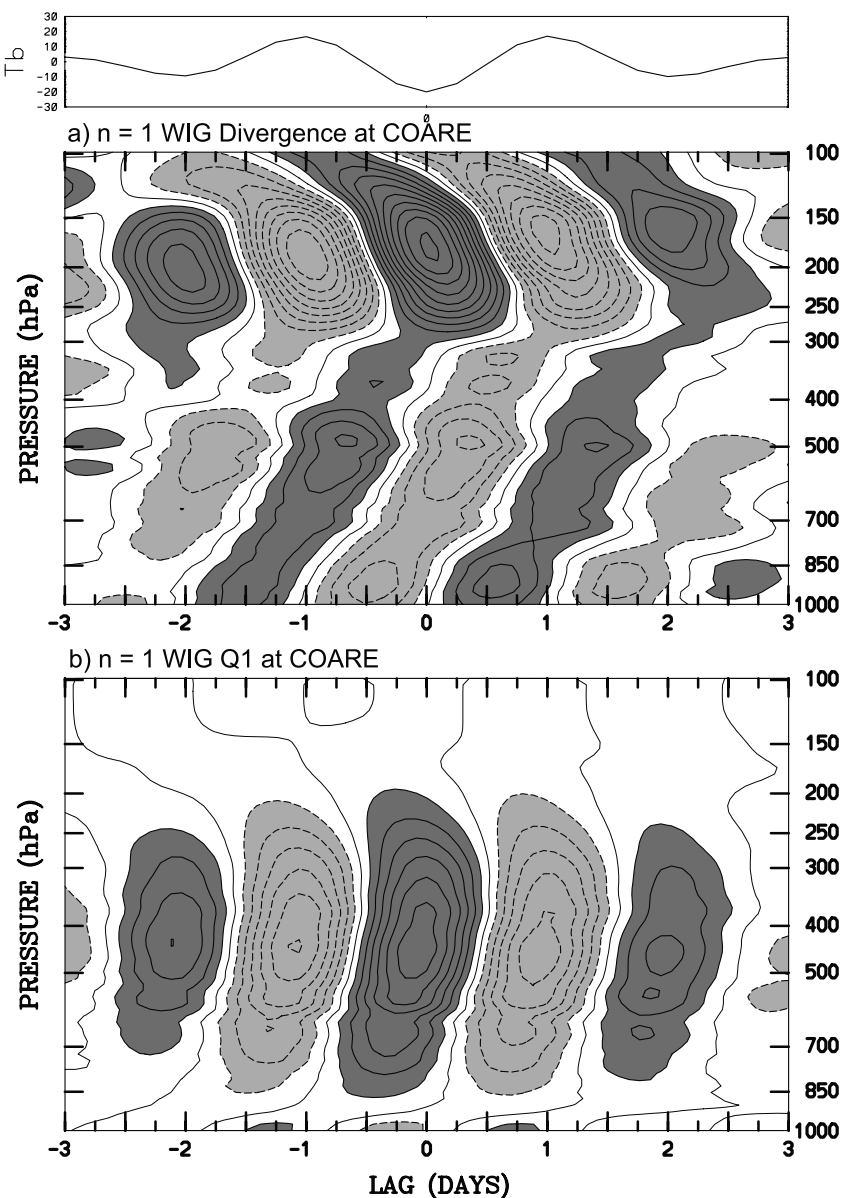


**Figure 11.** Time-height section of anomalies of (a) divergence and (b) diabatic heating (Q1) within the COARE region centered on 2.0°S, 155.0°E, scaled to a -20 K perturbation in  $n = 1$  WIG filtered  $T_b$  at the nearest grid point on day 0. Contour interval is  $1.0 \times 10^{-6} \text{ s}^{-1}$  for divergence and  $1 \text{ K d}^{-1}$  for Q1, with positive values shaded dark. The associated  $T_b$  anomaly is shown at the top in °K (adapted from Haertel and Kiladis [2004]).

that the WIG wind and temperature structure are linear responses to heating but also that the heating measurements are reliable. These results will be considered in more detail in section 11 with regards to the dynamics of CCEWs.

## 6. MIXED ROSSBY-GRAVITY WAVES

### 6.1. Observed Structure

[55] As discussed in section 1, dry MRG waves were the first of the modes predicted by Matsuno [1966] to be observed, through an examination of wind fluctuations in stratospheric radiosonde data [Yanai and Maruyama, 1966; Maruyama, 1967]. Further work established that MRG waves also exist in the troposphere coupled with convection

[Zangvil, 1975; Zangvil and Yanai, 1981], propagating westward as predicted by theory. Although MRG waves are distinct from EWs [Yanai and Murakami, 1970a, 1970b; Wallace, 1971], it appears that they, along with  $n = 1$  ER waves, coexist within a continuum, with some disturbances transitioning from one to another and developing hybrid structures, particularly over the west Pacific [Takayabu and Nitta, 1993; Dunkerton and Baldwin, 1995; Yang et al., 2007c]. As an illustration of this transitioning process, Figure 12 shows the first combined empirical orthogonal function of 2–10 day westward filtered OLR for the global 30°N–30°S domain. Gyres centered on the equator over the central Pacific are consistent with MRG waves (see Figure 3c), but as the wave anomalies progress westward,

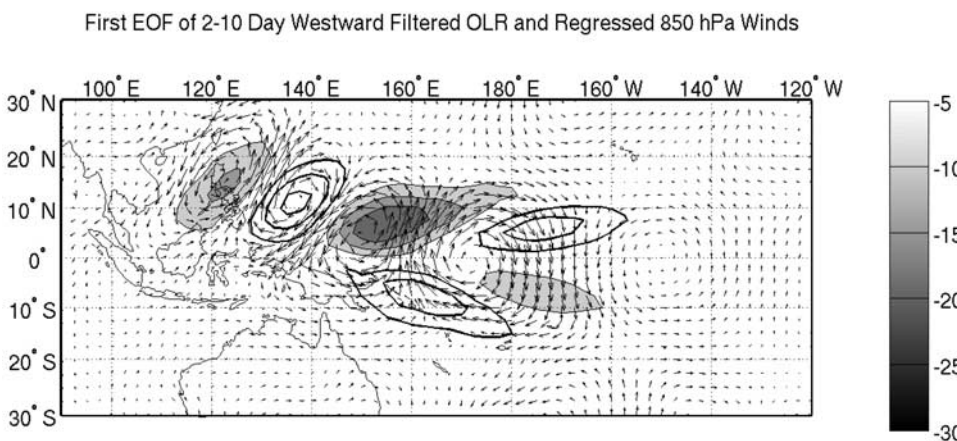


**Figure 12.** First empirical orthogonal function (EOF) of 2–10 day westward filtered outgoing longwave radiation (OLR) using 30°N–30°S data from 1979 to 2006. Also shown is the pattern of 850 hPa winds regressed onto the principal component time series of this EOF. OLR anomalies are contoured using a 5  $\text{W m}^{-2}$  interval, and negative anomalies are shaded according to the bar on the right.

they transition to off-equatorial gyres which then propagate northwestward toward the Philippines region. This is a commonly observed sequence for disturbances originating as equatorial waves over the western Pacific [Lau and Lau, 1990; Numaguti, 1995; Chang *et al.*, 1996; Sobel and Bretherton, 1999; Straub and Kiladis, 2003b].

[56] Relatively fast MRG waves are dominant in the upper troposphere and especially the lower stratosphere. While these upper waves may be initially forced by convection, they generally propagate as dry modes (see section 1). MRG waves closely coupled to convection have correspondingly shallower equivalent depths and display large perturbations in the lower troposphere [Liebmann and Hendon, 1990; Hendon and Liebmann, 1991; Dunkerton, 1993].

[57] Convectively coupled MRG waves appear in the westward propagating portion of the inertia-gravity wave continuum of the antisymmetric  $T_b$  spectrum of WK99 (Figure 1b). Their signal in satellite data is most prominent over the western and central Pacific ITCZ regions (Figure 5d). They are strongest during boreal summer and fall, although there is evidence that these waves do occur within all oceanic convergence zones throughout the year [Roundy and Frank, 2004a; WK99; WK00]. Over the west Pacific the convective and dynamical signals of MRG waves propagate westward at speeds from 15 to 25  $\text{m s}^{-1}$  and, in general, display eastward energy dispersion at  $\sim 5 \text{ m s}^{-1}$  [Takayabu and Nitta, 1993; Hendon and Liebmann, 1991; Dunkerton and Baldwin, 1995; Sobel *et al.*, 2004; WK00].

[58] Figure 13 shows the structure of the MRG wave using filtered CLAUS  $T_b$  as a predictor at the base point 7.5°N, 172.5°E. At 850 hPa the circulation pattern matches the theoretical structure of Figure 3c quite well, with gyres centered on and symmetric about the equator and an antisymmetric  $T_b$  signal. The wavelength is around 9000 km, consistent with previous estimates. Convection is enhanced in off-equatorial poleward flow and suppressed in equator-

ward flow, also consistent with the regions of divergence in Figure 3c. At later lags the equatorial gyres and associated  $T_b$  perturbations propagate to the northwest over the Philippines as in Figure 12 (not shown).

[59] The associated 200 hPa pattern in Figure 13c implies strong tilts in the vertical, with the vorticity and pressure patterns in near quadrature with those at 850 hPa. Here the gyres are displaced slightly north of the equator, a signal which persists even when using a symmetric Southern Hemisphere base point (7.5°S, 172.5°E) as a predictor, as well as a variety of base points throughout the Pacific and Atlantic ITCZ (not shown). Although such off-equatorial gyres can be expected as a response to heating displaced away from the equator [e.g., Gill, 1980; Mapes, 1998; Sobel and Horinouchi, 2000], asymmetries in the basic state flow may also be a factor [e.g., Aijoyer and Molinari, 2003].

[60] The vertical tilt of the MRG meridional wind is confirmed in Figure 14a using the Majuro radiosonde record. Lower tropospheric poleward flow at the time of lowest  $T_b$  is present from the surface to around 750 hPa, then tilts eastward to an elbow around 200 hPa, with an opposite tilt in the upper troposphere and lower stratosphere. This is roughly in the same sense as the WIG waves in Figure 10, except with a much larger scale and an elbow at a somewhat higher level. Other aspects of the vertical structure of temperature (Figure 14b) and moisture (Figure 14c) match those for the Kelvin and WIG waves described in sections 4 and 5.

## 6.2. Impacts of MRG Waves

[61] Frank and Roundy [2006] studied the relationship between MRG waves and tropical cyclone formation, finding a preference for cyclogenesis within counterclockwise MRG gyres as they moved off the equator and became cyclonic vorticity centers as in Figure 12. Such a sequence has been observed during the formation of individual tropical cyclones by Dickinson and Molinari [2002], Straub and Kiladis [2003b], and Zhou and Wang [2007]. The

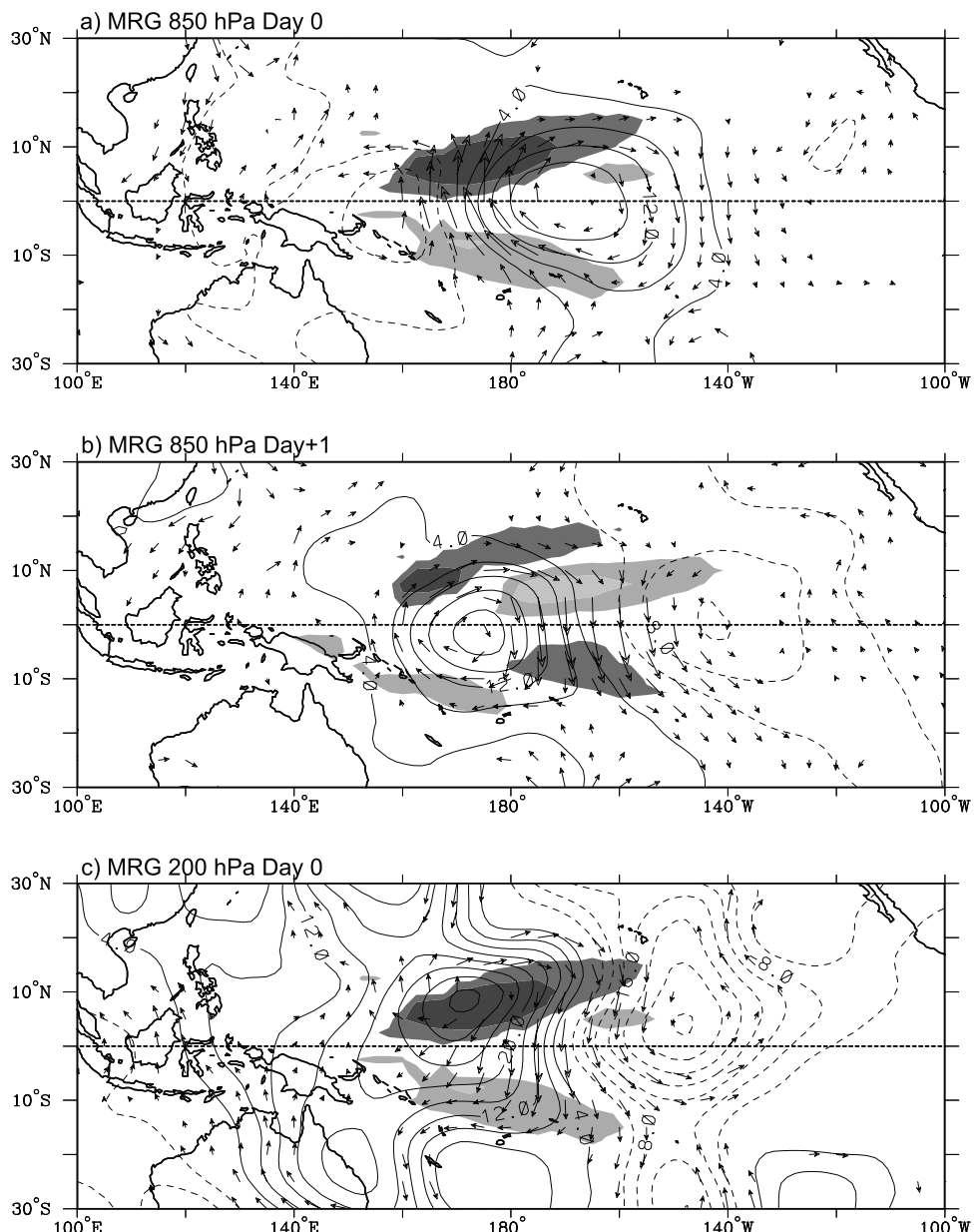


**Figure 13.** Maps of anomalous  $T_b$  (shading), stream function (contours), and wind (vectors) associated with a  $-20\text{ K}$  perturbation in MRG wave  $T_b$  at the base point  $7.5^\circ\text{N}$ ,  $172.5^\circ\text{E}$ , for (a) day 0 at  $850\text{ hPa}$ , (b) day +1 at  $850\text{ hPa}$ , and (c) day 0 at  $200\text{ hPa}$ . The contour interval is  $4 \times 10^{-5} \text{ m}^2 \text{ s}^{-1}$ , with negative contours dashed. Dark (light) shading is for negative (positive)  $T_b$  perturbations of  $\pm 10\text{ K}$  and  $3\text{ K}$ .  $T_b$  and wind vectors are locally significant at the  $95\%$  level, with the largest vectors around  $4\text{ m s}^{-1}$ .

transition from MRG to smaller-scale structures is thought to be aided by barotropic deformation in regions of zonal flow confluence, where low level westerlies and easterlies meet over the western Pacific, leading to a zonal contraction and the development of smaller-scale, off-equatorial Rossby gyres [Kuo et al., 2001; Aiyer and Molinari, 2003]. This confluence may also result in an amplification of a disturbance via the “wave accumulation” mechanism [e.g., Farrell and Watterson, 1985; Webster and Chang, 1988], where the wave’s zonal group velocity goes to zero, thereby trapping the wave energy and creating an environment conducive to tropical cyclone formation [Holland, 1995; Sobel and Bretherton, 1999].

[62] There is also some evidence for MRG-associated tropical cyclogenesis over the Indian sector [Bessafi and Wheeler, 2006], as indicated in Figure 5. Triggering of MRG waves by lateral forcing through the projection of extratropical Rossby waves onto MRG structures, as discussed for Kelvin waves in section 4, is also supported both observationally [Magaña and Yanai, 1995] and theoretically [Hoskins and Yang, 2000].

## 7. THE $n = 0$ EASTWARD INERTIO-GRAVITY WAVES

[63] Dry  $n = 0$  and higher meridional mode EIG waves are known to exist in the stratosphere [see Tindall et al.,

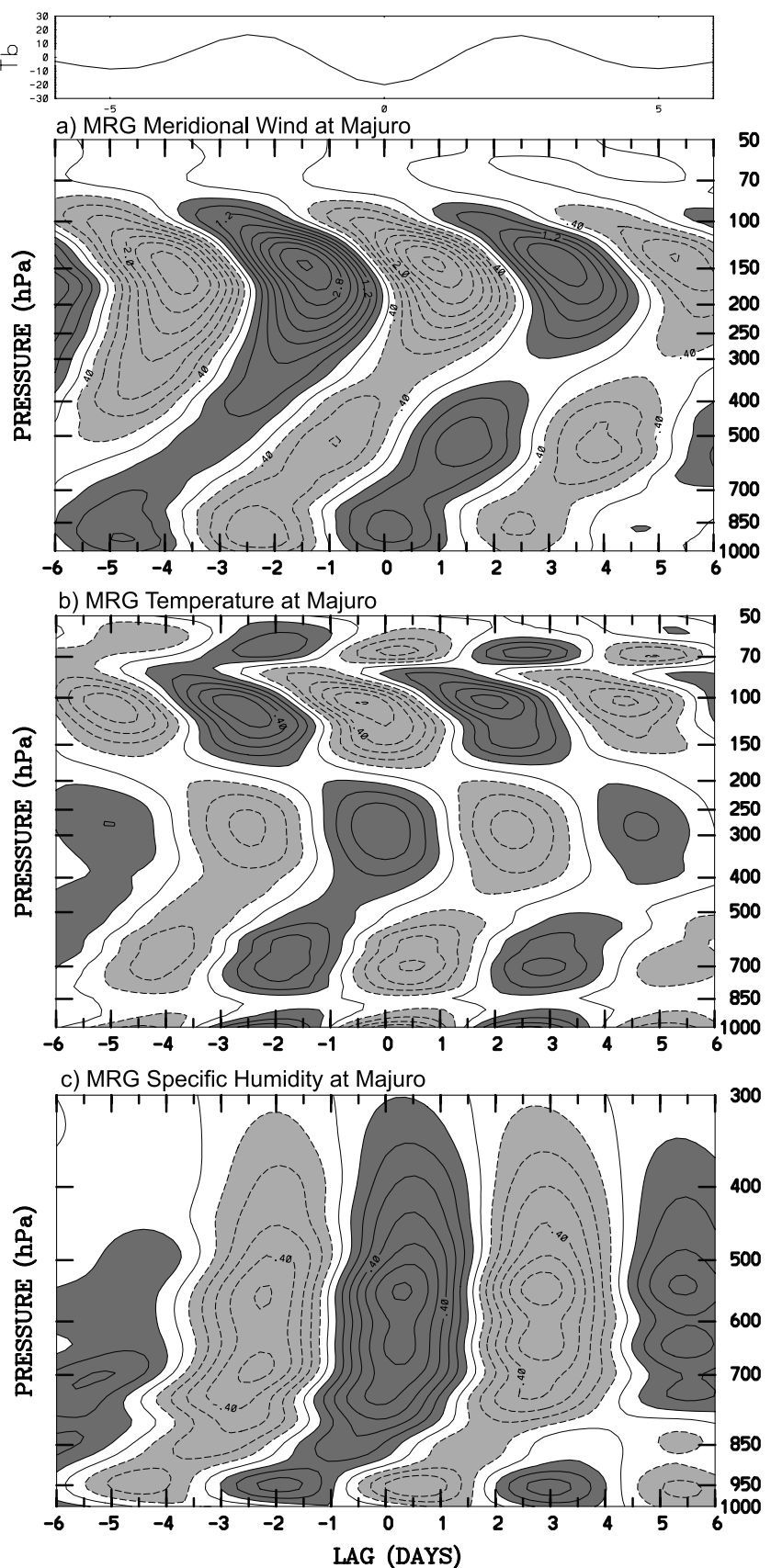


**Figure 14.** Time-height sections of anomalies in (a) meridional wind, (b) temperature, and (c) specific humidity at Majuro ( $7.1^{\circ}\text{N}$ ,  $171.4^{\circ}\text{E}$ ), scaled to a  $-20\text{ K}$  perturbation in MRG filtered  $T_b$  at the nearest grid point on day 0. Contour interval is  $0.4\text{ m s}^{-1}$  for wind,  $0.1\text{ K}$  for temperature, and  $0.1\text{ g kg}^{-1}$  for specific humidity, with negative contours dashed. Dark shading represents positive perturbations. The associated  $T_b$  anomaly is shown at the top in  $^{\circ}\text{K}$ .

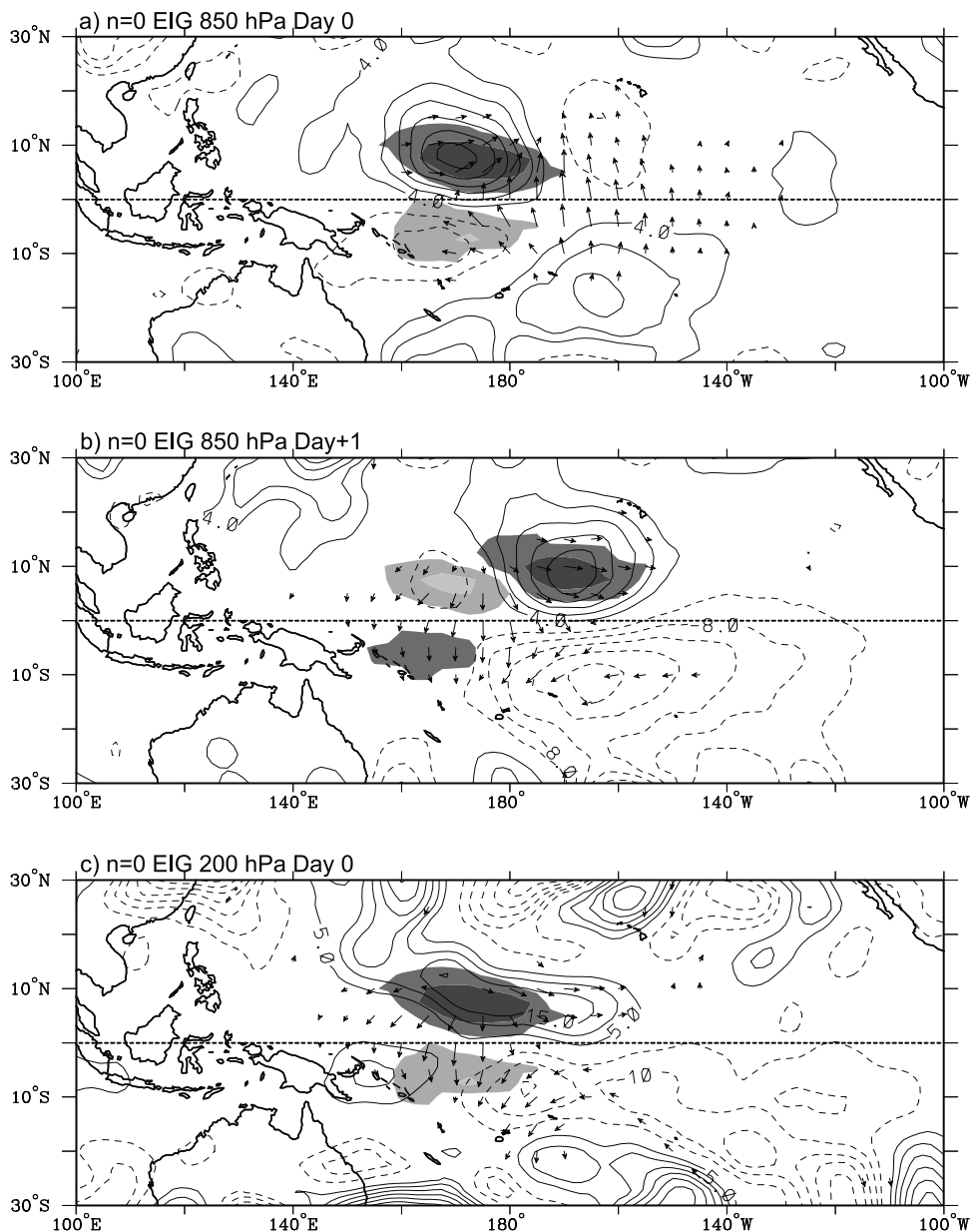


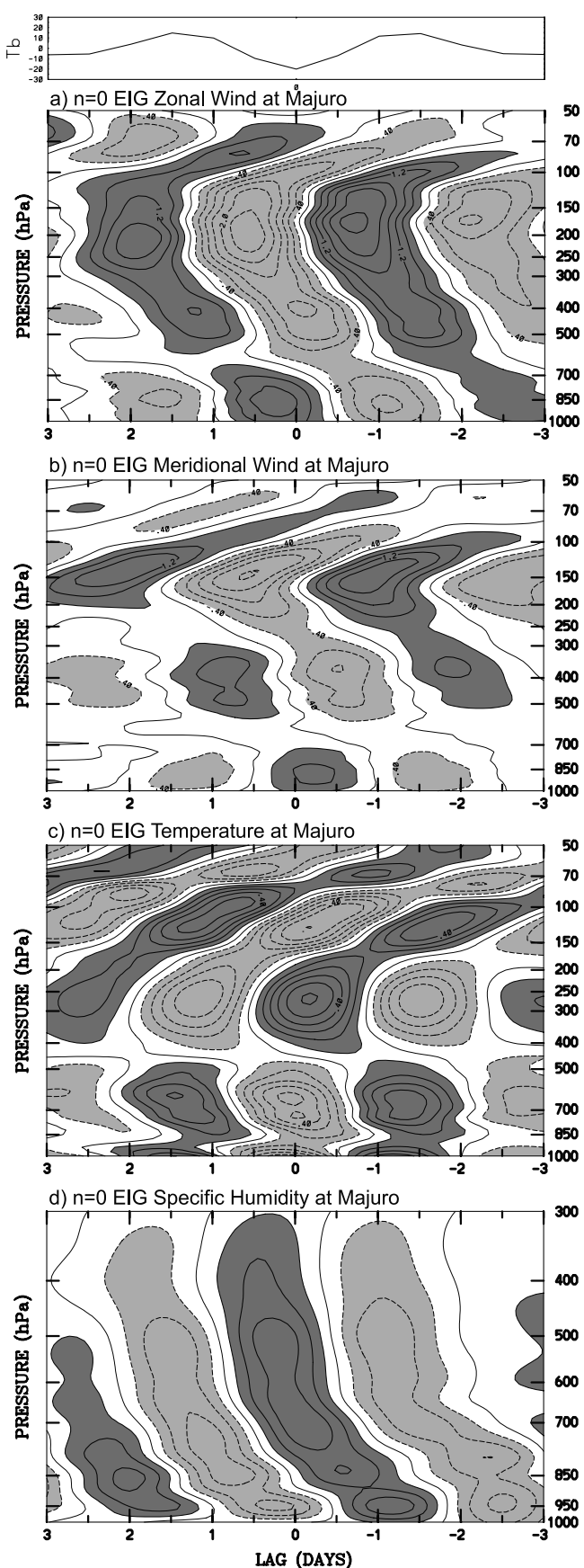
**Figure 15.** Maps of anomalous  $T_b$  (shading), geopotential height (contours), and wind (vectors) associated with a  $-20\text{ K}$  perturbation in  $n = 0$  EIG wave  $T_b$  at the base point  $7.5^\circ\text{N}$ ,  $172.5^\circ\text{E}$ , for (a) day 0 at  $850\text{ hPa}$ , (b) day +1 at  $850\text{ hPa}$ , and (c) day 0 at  $200\text{ hPa}$ . The contour interval is  $4\text{ m}$ , with negative contours dashed. Dark (light) shading is for negative (positive)  $T_b$  perturbations of  $\pm 10\text{ K}$  and  $3\text{ K}$ .  $T_b$  and wind vectors are locally significant at the  $95\%$  level, with the largest vectors around  $4\text{ m s}^{-1}$ .

2006]. The existence of convectively coupled  $n = 0$  EIG waves was first inferred by their space-time spectral peak by Takayabu [1994a], yet despite their strong spectral signal in Figure 1b, there is little mention of convectively coupled EIG waves in the literature.

[64] Following WKW00,  $T_b$  data are filtered for the  $n = 0$  EIG wave with the inclusion of the zonal wave number 0 portion of the associated space-time spectral peak (Figure 1b). Although this choice is somewhat arbitrary, inclusion of the zonal mean does not have a substantial impact on the results since the structure of the EIG wave is dominated by the zonally asymmetric component. Figure 5 indicates near congruence of the regions affected by MRG

and EIG activity. Although they are treated as separate disturbances here, the MRG and EIG spectral peaks form a continuum, and the extent of their covariability would be an interesting future research topic.

[65] WKW00 and Yang *et al.* [2003, 2007a, 2007b, 2007c] documented the structure of the  $n = 0$  EIG mode, while Yang *et al.* [2007a, 2007b] analyzed  $n = 1$  EIG waves as well. Since there is little evidence of an  $n = 1$  EIG spectral peak in Figure 1a, we will focus on the stronger  $n = 0$  EIG disturbance here. The  $n = 0$  EIG horizontal structure (Figure 15) deviates to a greater degree from its theoretical structure (Figure 3d) than other waves treated here since the convective and meridional wind fields do not display a



quadrature relationship with pressure, even at upper levels. Antisymmetric  $T_b$  and pressure propagate eastward coherently with its associated largely divergent cross equatorial flow at  $30 \text{ m s}^{-1}$ .

[66] Most aspects of the  $n = 0$  EIG vertical structure (Figure 16) show a remarkable resemblance to the CCEWs already discussed. One difference is the shallower location of the  $\sim 650 \text{ hPa}$  discontinuity in the EIG zonal wind signal, as opposed to the  $\sim 450 \text{ hPa}$  feature of the Kelvin wave. A similar discontinuity is observed in the meridional flow above and below  $600 \text{ hPa}$  (Figure 16b), which may relate to the location of the freezing level there. Large longitudinal and seasonal differences in the structure of the  $n = 0$  EIG wave are thought to be due to Doppler shifting by the basic state flow [Yang *et al.*, 2007a, 2007b].

## 8. EQUATORIAL ROSSBY WAVES

### 8.1. Observed Structure

[67] Atmospheric  $n = 1$  ER waves were inferred in the early 1980s through study of symmetric cyclonic circulations straddling the equator [Keen, 1982]. These westward propagating “cyclone pairs” sometimes simultaneously develop into tropical depressions and were thought to influence the equatorial ocean through wind stress associated with the accompanying “westerly wind burst” along the equator. Takayabu [1994a] unambiguously identified the spectral signal in cloudiness of convectively coupled ER waves, and soon after they were studied within the context of the COARE data set [Numaguti, 1995; Pires *et al.*, 1997]. Kiladis and Wheeler [1995] composited the dynamical structure of ER waves and found, somewhat surprisingly, that they had an equivalent barotropic structure in the vertical in their temperature and wind fields, at least over their central Pacific study region. Subsequent work has established that ER waves indeed appear to have barotropic structures where they are only weakly coupled to convection but a more complex vertical structure over the warm pool when deep convection is involved [Yang *et al.*, 2007a, 2007c; WKW00]. This change in structure may not only be related to convective coupling, but also to differences in vertical shear from the western to eastern Pacific. For example, Wang and Xie [1996] found that stronger easterly shear, as is found over the warm pool, favors higher-amplitude baroclinic modal structures in the lower troposphere in ER and MRG waves, with much less pronounced effects on Kelvin waves.

**Figure 16.** Time-height sections of anomalies in (a) zonal wind, (b) meridional wind, (c) temperature, and (d) specific humidity at Majuro ( $7.1^\circ\text{N}$ ,  $171.4^\circ\text{E}$ ), scaled to a  $-20 \text{ K}$  perturbation in  $n = 0$  EIG filtered  $T_b$  at the nearest grid point on day 0. Contour interval is  $0.4 \text{ m s}^{-1}$  for wind,  $0.1 \text{ K}$  for temperature, and  $0.1 \text{ g kg}^{-1}$  for specific humidity, with negative contours dashed. Dark shading represents positive perturbations. The associated  $T_b$  anomaly is shown at the top in  $^\circ\text{K}$ .

[68] Since ER variability decreases rather sharply from west to east across the Pacific (Figure 5b) [Roundy and Frank, 2004a], we examine the composite structure of ER waves over the west Pacific warm pool, at the point  $7.5^{\circ}\text{N}$ ,  $152.0^{\circ}\text{E}$  (Figure 17). Note that the spectral filter used for this analysis differs from that used in past studies [Roundy and Frank, 2004a, 2004b; WK99], with a low end cutoff at 1 m equivalent depth to avoid splitting the spectral peak centered at  $\sim 30$  days (Figure 1a). Tests reveal that the overall results are not sensitive to these choices. Overall, ER wave structure varies much more substantially by season and regionally than the CCEWs treated so far (as does the MJO [Kiladis et al., 2005]), but Figure 17 is representative of ER structures over the warm pool in general.

[69] Cyclone pair structures are clearly visible in Figures 17a and 17b, with circulation and convective features propagating westward at a phase speed of around  $4.5 \text{ m s}^{-1}$ . While the convective signal is displaced to the east of the cyclones as in the theoretical picture (Figure 3e), there is also a substantial  $T_b$  signal within the equatorial westerlies between the cyclones. Also visible in Figure 17a are locally low pressures on the equator and easterly wind perturbations to the east of the convective center, a pattern strongly resembling the “forced Kelvin response” to equatorial heating [Gill, 1980]. Evidently, ER waves last long enough and propagate slowly enough to force a “Gill-type” response, as in the MJO [Hendon and Salby, 1994].

[70] Once the convective signal reaches the region of New Guinea, it dissipates south of the equator (Figure 17b), while the northern gyre and convective center shift to around  $15^{\circ}\text{N}$  as they continue to propagate westward into the Indian Ocean (not shown). This signal persists even for base points south of the equator within the South Pacific Convergence Zone so that northern Australia is less affected by ER activity than is Indochina (Figure 5b).

[71] At 200 hPa (Figure 17c), mass flows outward from the convection and an anticyclonic circulation located almost directly above the cyclone in Figure 17b. At earlier lags the equatorial signal is preceded by a positively tilted extratropical Rossby wave train propagating equatorward from the North Pacific storm track (not shown), supporting the notion that ER waves can be forced by wave energy originating in the extratropics, as was discussed by Kiladis and Wheeler [1995], Kiladis [1998], Hoskins and Yang [2000], and Yang et al. [2007c].

[72] Unlike the equivalent barotropic structures for ER waves farther east, circulation features in Figures 18a and 18b have a first baroclinic mode vertical structure, with convection embedded within westerly and southerly anomalies up to  $\sim 400$  hPa and opposite circulations above this up to the tropopause. The temperature structure is more complex (Figure 18c), with a very shallow cold layer (only at the lowest level of data) within the convective region, then two more shallow warm and cold layers above this, and a more typical warm layer in the upper troposphere capped by the usual cold tropopause level. The thin layering of the stratospheric temperature signals are in accord with the relatively slow ER phase speed given by equation (17).

[73] The moisture signal also differs from other CCEWs discussed in sections 4–7: moistening occurs nearly simultaneously throughout the troposphere starting at around day  $-4$ , with an unusual discontinuity at the 950 hPa level. Thus, it appears likely that ER waves have a rather different evolution of cloud morphology than the other waves, although this has yet to be confirmed.

## 8.2. Impacts of ER Waves

[74] Unlike other CCEWs, ER  $T_b$  variance is most dominant over the Asian monsoon and warm pool regions, rather than in the Pacific ITCZ (Figure 5b). Much of the peak activity over the western North Pacific and Asia is due to westward propagating monsoon gyres confined to the Northern Hemisphere [Chatterjee and Goswami, 2004], although symmetric ER waves are commonly observed over the Indian Ocean [Roundy and Frank, 2004b; Yokoi and Satomura, 2005; Shinoda and Han, 2005], and cases of propagating ER waves impacting the Australian-Indonesian monsoon were identified by Wheeler and McBride [2005].

[75] Analysis of ER waves is more problematic than the other CCEWs because their slow speeds and broad spatial scales allow them to be strongly modulated by propagation through varying background wind states. In particular, wind anomalies associated with the MJO are similar in magnitude to the phase speeds of ER waves. Another potential complication is that the ER spectral peak in Figure 1a lies in a region that could partially represent a standing component of the MJO [Roundy and Frank, 2004b], although eastward propagation is dominant at this time scale [Zhang and Hendon, 1997]. Nevertheless, westward propagating components of the MJO corresponding to ER waves are well documented [Zhu and Wang, 1993; Kemball-Cook and Wang, 2001; Masunaga, 2007]. Roundy and Frank [2004b, 2004c] give statistical and case study evidence of the modulation of convective activity due to the interaction of the MJO and ER modes, with an ER wave apparently responsible for the genesis of the MJO in some cases. One possible mechanism for the statistical relationship between ER waves and the MJO is that the MJO modulates propagation of midlatitude Rossby wave trains [Weickmann and Berry, 2007]. These wave trains can perturb the equatorial waveguide in a manner that generates ER waves, which may then, in turn, influence the amplitude and timing of the MJO itself [e.g., Meehl et al., 2001; Roundy and Frank, 2004b].

[76] Frank and Roundy [2006], Bessafi and Wheeler [2006], and Molinari et al. [2007] demonstrate relationships between ER waves and tropical cyclogenesis. When evident, cyclogenesis events tend to cluster to the east of the ER wave trough, with ER waves also subject to the deformation effects of varying zonal flow as described in section 6 for MRG waves.

## 9. EASTERLY WAVES

[77] Although EWs do not correspond to a normal mode solution of Matsuno's [1966] SW equations, they were the

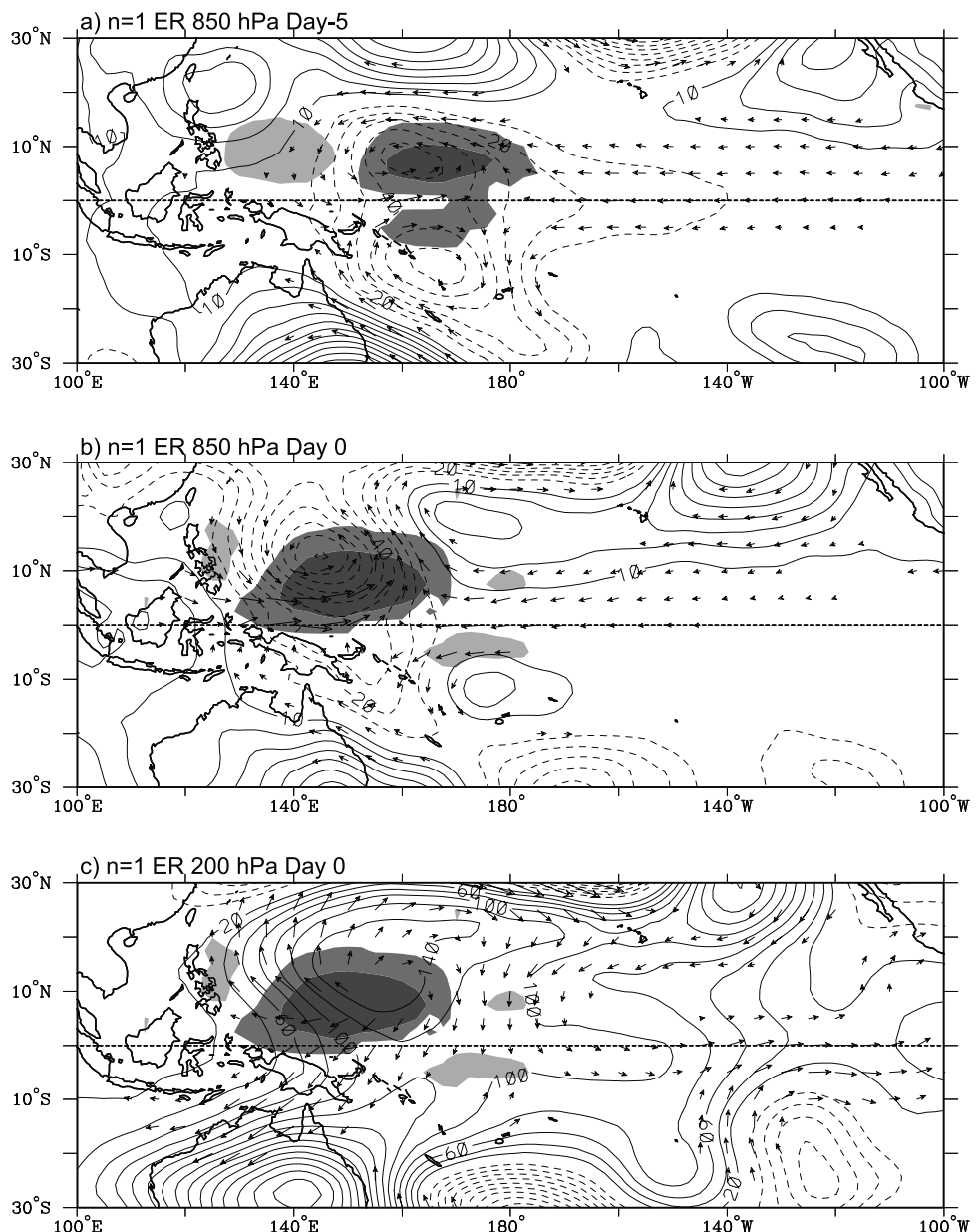
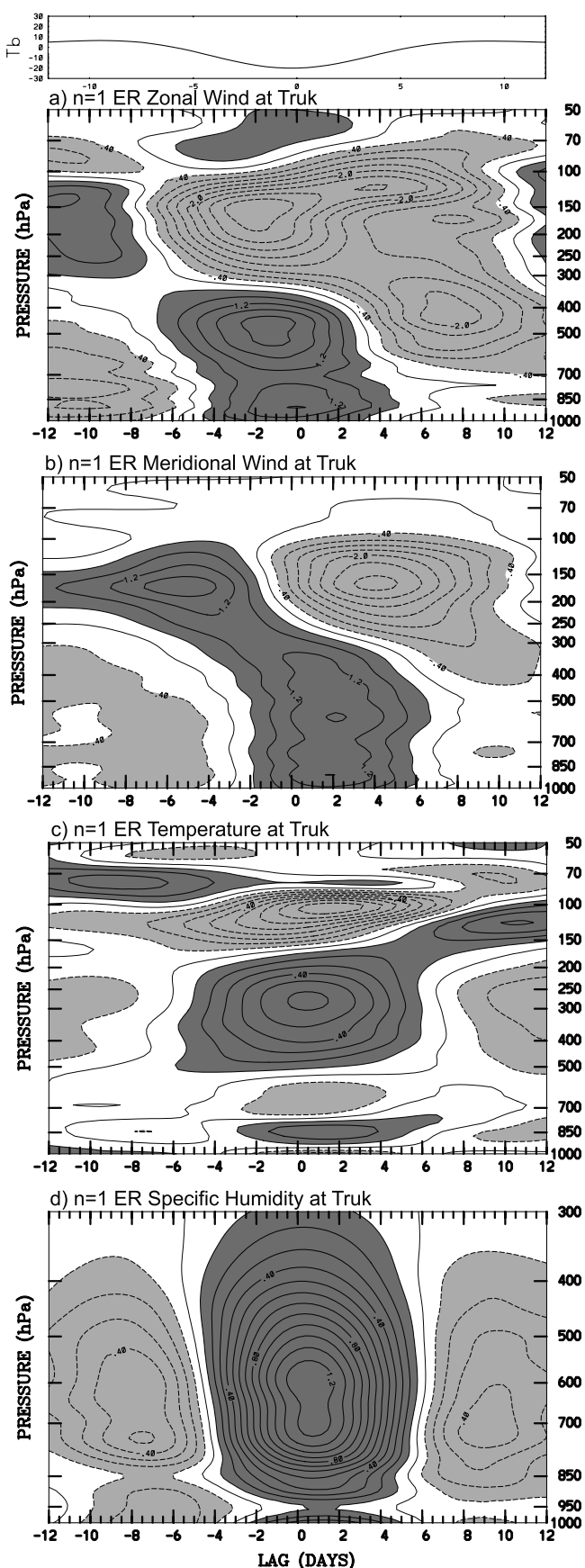


**Figure 17.** Maps of anomalous  $T_b$  (shading), geopotential height (contours), and wind (vectors) associated with a  $-20 \text{ K}$  perturbation in  $n = 1$  ER wave  $T_b$  at the base point  $7.5^\circ\text{N}, 152.0^\circ\text{E}$ , for (a) day -5 at 850 hPa, (b) day 0 at 850 hPa, and (c) day 0 at 200 hPa. The contour interval is 10 m in Figures 17a and 17b and 20 m in Figure 17c, with negative contours dashed. Dark (light) shading is for negative (positive)  $T_b$  perturbations of  $\pm 10 \text{ K}$  and 3 K.  $T_b$  and wind vectors are locally significant at the 95% level, with the largest vectors around  $2 \text{ m s}^{-1}$ .

first convectively coupled wave to be recognized (see section 1) and have extremely important impacts, and therefore they will be briefly treated here within the context of the other modes discussed in sections 4–8. EWs are off-equatorial westward propagating Rossby gyres that appear as “inverted troughs” in pressure and wind within the trade wind field of the ITCZ of the Northern Hemisphere. They are primarily active over the Pacific and Atlantic sectors, as well as over sub-Saharan Africa during the monsoon season (Figure 5c). The signal of EWs appears most prominently in space-time spectra calculated for seasons when ITCZ convection is most active, i.e., May through October (WK99). This TD-type spectral signal merges with the

MRG signal in the antisymmetric spectrum (WK99, Figure 5c), a reflection of the broad class of hybrid waves discussed in section 6. As evidence of this, when 850 hPa circulation is regressed against TD-filtered  $T_b$  in the region of the westernmost Pacific ITCZ, the pattern shown in Figure 12 is almost perfectly reproduced (not shown), representing the transition from MRG to EWs.

[78] Early observations of EWs in the Pacific and West African/east Atlantic regions indicate that they have wavelengths of 2500–3500 km, westward phase speeds of  $8 \text{ m s}^{-1}$ , periods of 3–4 days, and maximum meridional wind anomalies at 700–850 hPa [Reed and Recker, 1971; Reed et al., 1977; Thompson et al., 1979]. Wave characteristics and



phasing with convection vary with latitude and between land and ocean regions in the West African/east Atlantic region [Reed et al., 1977; Kiladis et al., 2006]. Studies of Pacific EWs also find variations in wave characteristics as a function of longitude [Reed and Recker, 1971; Tam and Li, 2006; Serra et al., 2008]. Much of the structural change observed in Pacific EWs is attributed to variations in the background mean vertical wind shear across the Pacific [Holton, 1971; Reed and Recker, 1971]. Horizontal and vertical wind shear also strongly influences the structure of African EWs [Norquist et al., 1977; Hsieh and Cook, 2005], and the strong relationship between EWs and tropical cyclogenesis has been attributed to the effects of deformation and wave accumulation within zonally varying zonal flows (see section 6). Conversely, the eastward dispersion of Rossby wave energy emanating from tropical cyclones has been shown to be a source of EWs [Holland, 1995; Sobel and Bretherton, 1999; Krouse et al., 2008], along with potential generation by extratropical forcing [Tam and Li, 2006] and latent heating within the region of the African easterly jet [e.g., Hsieh and Cook, 2007; Thorncroft et al., 2008].

[79] The structure of EWs has been extensively documented and will not be presented here, especially since their vertical structure and scale are virtually indistinguishable from the MRG waves in Figure 14 [see Kiladis et al., 2006; Serra et al., 2008]. Energetics studies of EWs over Africa demonstrate strong baroclinic conversions, with energy extracted from the vertical shear within the African easterly jet [Norquist et al., 1977; Kiladis et al., 2006; Hall et al., 2006; Hsieh and Cook, 2007]. As EWs leave the coast, barotropic conversions become more dominant, with energy extracted primarily from the basic state horizontal shear. In the Pacific ITCZ, there is much less horizontal and vertical shear in the basic state, and energetics calculations indicate that latent heating must be the primary energy source for Pacific EWs [Tai and Ogura, 1987; Lau and Lau, 1992; Tam and Li, 2006; Serra et al., 2008]. While the energetics of EWs have been documented to a large extent, similar work has yet to be done for the other CCEWs. Although it is likely that latent heating must be a dominant energy source for most CCEWs, the presence of strong shear, especially over monsoon regions, may also be important in their generation and maintenance.

## 10. SELF-SIMILARITY IN CONVECTIVELY COUPLED WAVE STRUCTURES

[80] The analyses of CCEW characteristics reviewed above reveals some intriguing aspects of their organization.

**Figure 18.** Time-height sections of anomalies in (a) zonal wind, (b) meridional wind, (c) temperature, and (d) specific humidity at Truk (7.5°N, 151.9°E), scaled to a  $-20\text{ K}$  perturbation in  $n = 1$  ER filtered  $T_b$  at the nearest grid point on day 0. Contour interval is  $0.4 \text{ m s}^{-1}$  for wind,  $0.1 \text{ K}$  for temperature, and  $0.1 \text{ g kg}^{-1}$  for specific humidity. Dark shading represents positive perturbations. The associated  $T_b$  anomaly is shown at the top in °K.

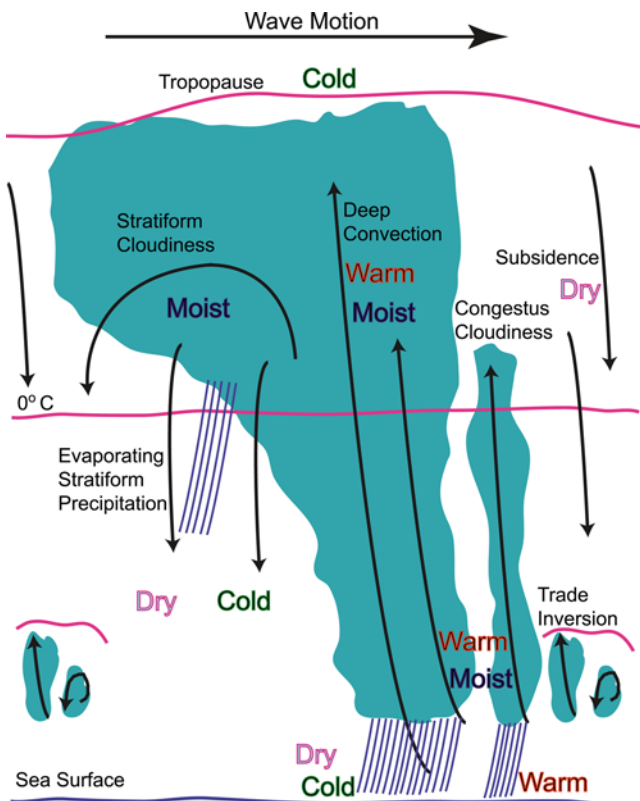


**Figure 19.** The hierarchy of cloudiness, temperature, and humidity within CCEWs, valid from MCS to MJO scales. Wave movement is from left to right (adapted from Johnson et al. [1999], Straub and Kiladis [2003c], and Khouider and Majda [2008]).

While their horizontal scales and propagation characteristics differ widely, their vertical structures display a remarkable level of “self-similarity,” regardless of the wave considered. With the exception of ER waves, all of the CCEWs (as well as the MJO and EWs) are characterized by the following features: (1) anomalously warm lower tropospheric temperatures ahead of the deepest convection (as inferred from the large-scale upward vertical motion and  $T_b$  minimum), from the surface to  $\sim 500$  hPa, transitioning to cold perturbations just prior to and during the  $T_b$  minimum; (2) anomalously warm upper tropospheric temperatures in the layer from 500 to 150 hPa, peaking at around 250 hPa, either just prior to or coincident with the deepest convection; (3) a change in the direction of the vertical tilt (elbow) in the temperature and wind fields at  $\sim 250$ – $300$  hPa such that the perturbations ascend (descend) with time below (above) this level; (4) convergence and moistening of the lowermost layers ahead of the deepest convection, followed by a rapid lofting of moisture throughout the entire troposphere just before the onset of deepest convection, quickly evolving into a moist over dry signal during and immediately following the convective peak; and (5) a separate cold, dry signal in the shallowest layers near the surface during the time of downdrafts.

[81] This scale invariance indicates that diabatic heating and cloud morphology is organized among CCEWs in such a way that its evolution is consistent with the observed

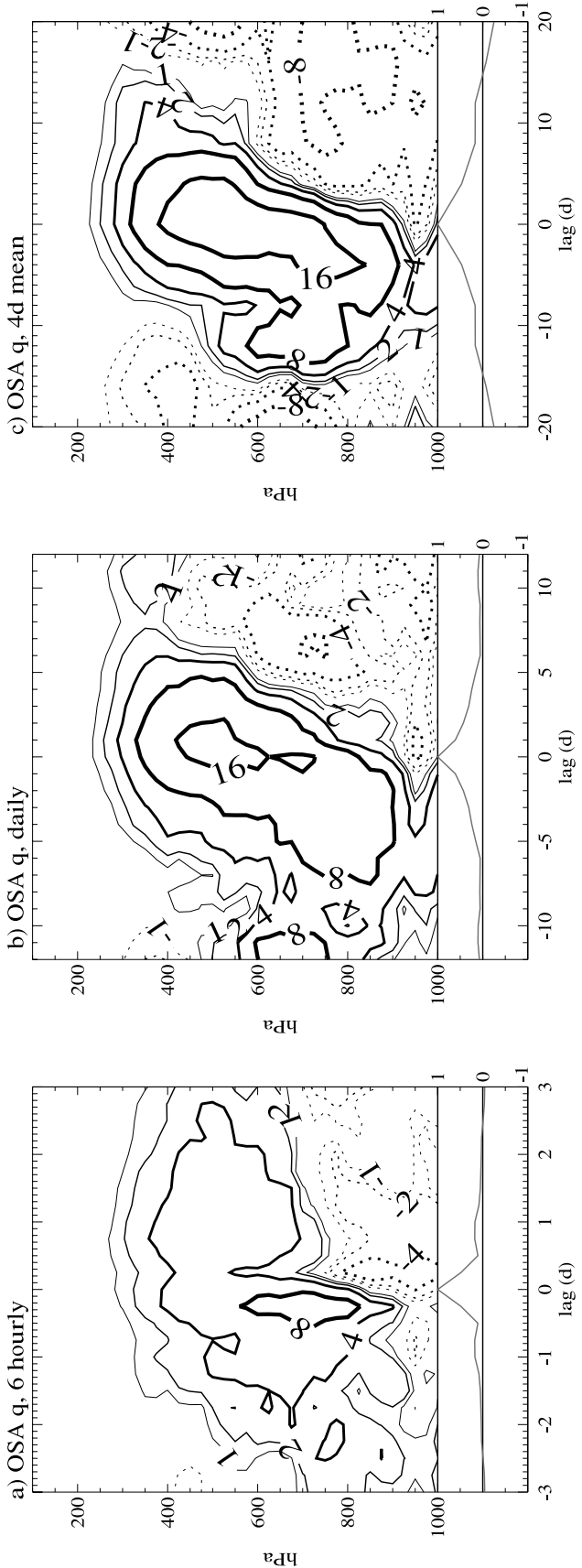
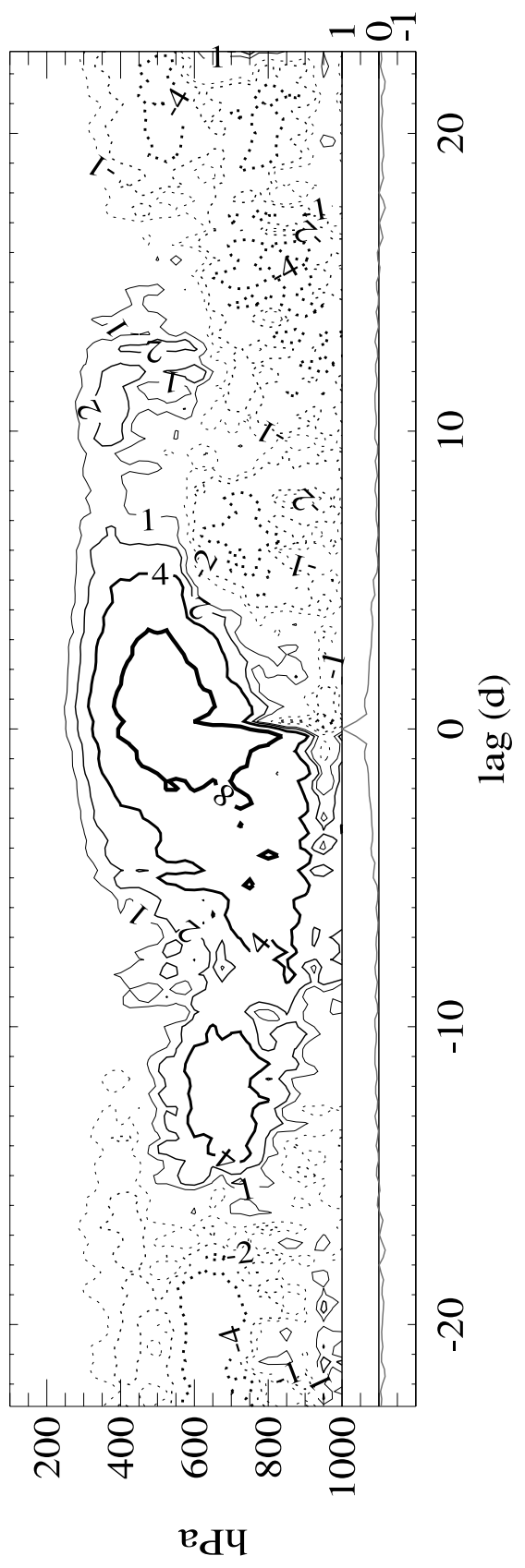
dynamical fields. As discussed in section 5, a propagating Q1 structure in Figure 11b can reproduce the observed  $n = 1$  WIG vertical structure in a linear primitive equation model and suggests that a consistent evolution in cloud morphology within CCEWs ought to be observed, as in Kelvin (section 4) and WIG waves (section 5). This progression mirrors that of individual MCSs and is illustrated in Figure 19. Shallow cumulus capped at the trade inversion first develops into taller “congestus” clouds which precondition the atmosphere by moistening the midtroposphere, allowing the development of deep convective heating in cumulonimbus clouds [Johnson et al., 1999]. This is followed by stratiform rainfall with upper tropospheric precipitation falling into relatively dry lower levels, cooling the air through evaporation. Such an evolution has also been confirmed for the MJO [Kiladis et al., 2005; Masunaga et al., 2006; Benedict and Randall, 2007; Haertel et al., 2008].

[82] Diabatic heating profiles like that in Figure 11b are, in fact, characteristic even to the development of individual cumulonimbus clouds, where a time scale of hours is set by mesoscale dynamics and microphysical processes. The ubiquity of vertical heating and dynamical profiles along with cloud morphological fields from MCSs to planetary scales raises some fundamental questions about the manner in which convection is coupled to the large-scale circulation [Kiladis et al., 2005; Mapes et al., 2006; Majda, 2007]. An example of such scale invariance is given in Figure 20, where specific humidity is regressed upon rain rate filtered for successively longer time scales using radiosonde data from the Outer Sounding Array during COARE. The shapes of these profiles qualitatively resemble the humidity evolution for individual CCEWs in Figures 8c, 10c, 14c, and 16d, again suggestive of a systematic transition from shallow to deep convection, then stratiform precipitation dominant across all four time scales depicted. A similar treatment of divergence also leads to consistent inferred vertical motion and diabatic heating fields [Mapes et al., 2006].

[83] By testing the idea that larger-scale convective disturbances can be represented as aggregates of smaller-scale MCSs, Mapes et al. [2006] concluded that the only way tilted vertical structures could be produced was through a variation in the populations of cloud types across a large-scale wave, rather than variations in either the lifetimes or degree of evolution of individual MCSs as a function of wave phase. This “stretched building block” hypothesis posits that the relative abundance of shallow, deep, and stratiform cloudiness is modulated by the large-scale environment, whereby the life cycles of individual MCSs are aliased onto longer time scales through linear superposition. The observed self-similarity across scales has obvious implications for the theory and numerical simulation of CCEWs, as we discuss further in section 11.

## 11. MODELS OF CONVECTIVELY COUPLED WAVES

[84] Efforts to explain an observed phenomenon theoretically often give rise to physically based models, so it is

**d) OSA q, unfiltered****Figure 20**

natural that efforts to model CCEWs have recently accelerated. There is already a long history of work aimed at modeling the MJO, yet it can be claimed that this still represents one of the great stumbling blocks in tropical meteorology (see reviews by Zhang [2005], Slingo *et al.* [2005], and Waliser [2006]). CCEWs are arguably simpler disturbances, but challenges for the hierarchy of models used to explain and simulate them still exist.

### 11.1. Simple Theoretical Models

[85] The nature of the coupling between convection and large-scale circulation has been treated theoretically since the 1970s, starting with formulations such as *wave conditional instability of the second kind* (*wave-CISK*). In its most general interpretation, wave-CISK latent heating induces wavelike circulations that favor further convection via low level convergence [see Hayashi, 1970; Lindzen, 1974; Stevens *et al.*, 1997]. While wave-CISK formulations feature wave growth due to the generation of APE, in their simplest formulations the largest growth occurs at the smallest resolvable scale, leading to the so-called “CISK catastrophe” [Crum and Dunkerton, 1992; Matthews and Lander, 1999]. Nevertheless, the basic principle has led to the formulation of widely used convective parameterization schemes in general circulation models (GCMs) which are closed on moisture convergence [Kuo, 1974; see Kasahara, 2000]. An alternate view, not necessarily mutually exclusive from wave-CISK, is known as *quasi-equilibrium* (*QE*). QE is predicated on the fact that the buoyancy adjustment time scale of convection is short compared to the lifetime of the large-scale disturbances they are embedded within [see Emanuel, 2007]. In its simplest form, QE states that over large areas, the production of instability by large-scale forcing due to radiation and heat fluxes is balanced by its removal via large-scale convection, either instantaneously or with some typically short (in hours) lag time. QE has formed the basis for “adjustment scheme” convective parameterizations, as in the Arakawa and Schubert [1974] and Betts and Miller [1986] formulations, where convection is closed on widely varying definitions of parcel instability or some other measure of “disequilibrium” in the local thermodynamic sounding such as *convective available potential energy* (*CAPE*). For example, the constraint of *strict quasi-equilibrium* (*SQE*) assumes that convection consumes CAPE in such a way that the free tropospheric temperature profile remains moist adiabatic and is directly correlated to the perturbations in the boundary layer moist entropy such as moist static energy (*MSE*) or equivalent potential temperature.

[86] Observations show that QE holds over the tropics to the extent that there is a good correlation between CAPE and deep convection in monthly data [e.g., Bhat *et al.*,

1996]. In addition, free tropospheric temperature profiles within convecting regions do tend to follow moist adiabats [Xu and Emanuel, 1989], and their perturbations vary coherently within the 800–200 hPa layer [Holloway and Neelin, 2007], as predicted by QE. However, these profiles are only moderately correlated with boundary layer equivalent potential temperature [Brown and Bretherton, 1997], or MSE [Holloway and Neelin, 2007], although such correlations improve somewhat on monthly or longer time scales, suggesting the importance of factors other than a rapid vertical adjustment to boundary layer moist entropy. In addition, on synoptic time scales characteristic of CCEWs, CAPE tends to peak prior to convective initiation and is more often negatively correlated with the deepest convection [Sherwood, 1999; Straub and Kiladis, 2003c; Sobel *et al.*, 2004], counter to the assumptions of SQE. In the simplest models of CCEWs, SQE leads to a quadrature relationship between convective heating and temperature and actually becomes a negative correlation (damping) when allowing for a finite time for convective development [Emanuel *et al.*, 1994]. SQE also results in CCEW structures comprising only a first baroclinic vertical mode, in contrast to the higher-mode structures in observations, although this can be mitigated by further assumptions in more complex models [Neelin and Zeng, 2000]. The fact that even relatively simple QE-based convective closures lead to quite realistic GCM behavior on longer time scales [e.g., Zeng *et al.*, 2000] shows that it is indeed a useful simplification for climate studies, even if it is not strictly valid on the scale of CCEWs.

### 11.2. Vertical Modes

[87] Given the complex vertical structures of CCEWs described in sections 4–10, many theoretical approaches used to account for these configurations have relied on the idea of vertical modes. As discussed in section 2, a solution to the primitive equations linearized about a basic state of rest may be decomposed into a superposition of vertical modes, each of which is algebraically equivalent to a solution of the linearized shallow water equations associated with an equivalent depth (Table 1).

[88] In an unbounded atmosphere, there is a continuum of vertical modes and equivalent depths, although reasonable vertical decompositions can be obtained by assuming discrete modes corresponding to a rigid lid [e.g., Fulton and Schubert, 1985; Mapes, 1998]. Using the observed WIG Q1 heating profile in Figure 11b, which is significantly nonzero only below 150 hPa, a minimal decomposition of the heating is obtained by projecting it onto the vertical modes for an atmosphere having the COARE mean temperature profile and an upper boundary at 150 hPa [Haertel and Kiladis, 2004]. The heating projects primarily onto just two

**Figure 20.** Lag-height regressions of specific humidity versus rain rate from TOGA COARE Outer Sounding Array (OSA). The data are progressively regressed to coarser time intervals of (a) 6 h, (b) 1 day, and (c) 4 days, and a light high-pass filter is used for each panel (cutoff period six times the lag window width). (d) The original unfiltered 6 h data are used, with a very wide lag window. Contour unit is  $0.1 \text{ g kg}^{-1} \text{ mm}^{-1} \text{ h}^{-1}$  (reprinted from Mapes *et al.* [2006], copyright 2006, with permission from Elsevier).

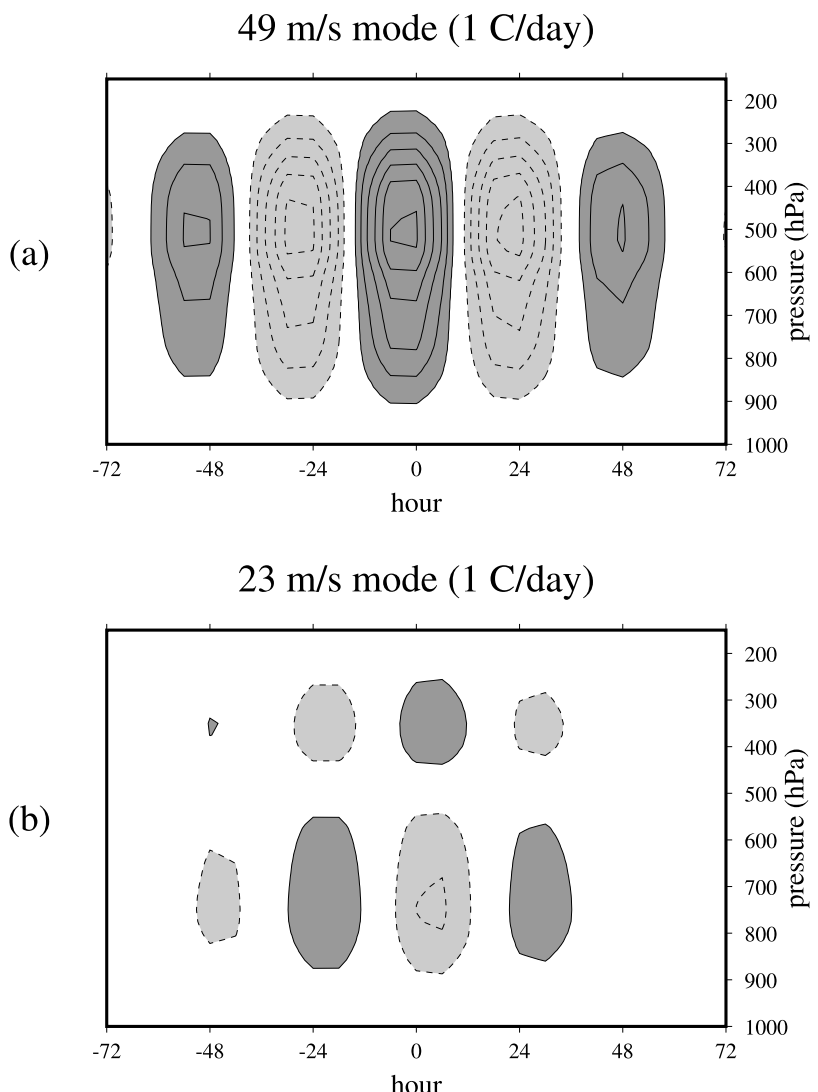


**Figure 21.** Time-height cross section of the first two vertical modes of the composite TOGA COARE diabatic heating (Q1) field shown in Figure 11b. Contours are  $1 \text{ C d}^{-1}$ , with positive values shaded dark [from Haertel and Kiladis, 2004].

modes. The first has a gravity wave speed of  $49 \text{ m s}^{-1}$  and is associated with deep convective heating of the same sign throughout the troposphere peaking at midlevels (Figure 21a). The second has a gravity wave speed of  $23 \text{ m s}^{-1}$ , with heating of opposite sign in the lower and upper troposphere (Figure 21b). In WIG waves the second-mode upper level heating lags that of the deep convection, while its leading portion can also be reasonably envisioned as representing the effects of low level convergence and heating associated with shallow and congestus convection in Figure 19. Superposition of the two modes (e.g., Figure 22a) yields the gross features of the observed vertical tilt in Figure 11b, including the top-heavy heating profiles typically seen in tropical convective disturbances [Houze, 2004].

[89] Haertel and Kiladis [2004] recovered most of the dynamical structure of observed WIG waves by forcing a linear primitive equation model with the observed COARE WIG heating in Figure 11b moving westward at their

composite phase speed ( $16 \text{ m s}^{-1}$ ). Taking advantage of this linearity, they also examined the response to its first two vertical modes and to each individually. The two modes together reproduce the gross structure of the WIG tropospheric temperature field (Figure 22a), with upper (lower) warmth slightly leading (lagging) the position of deepest convection. Although the heating associated with the first mode is much stronger than the second, the temperature response to the second mode is significantly higher amplitude (Figures 22b and 22c). In both cases the temperature perturbations are nearly in quadrature with the heating, as in dry Kelvin or gravity modes (Figure 4b). Superposition of the modes also results in the latent heating from the first mode being in phase with the upper tropospheric positive temperature perturbation from the second mode, generating APE.

[90] In an analysis of the temperature tendency between Q1 heating and the adiabatic temperature change due to vertical motion in both the model and observations, Haertel

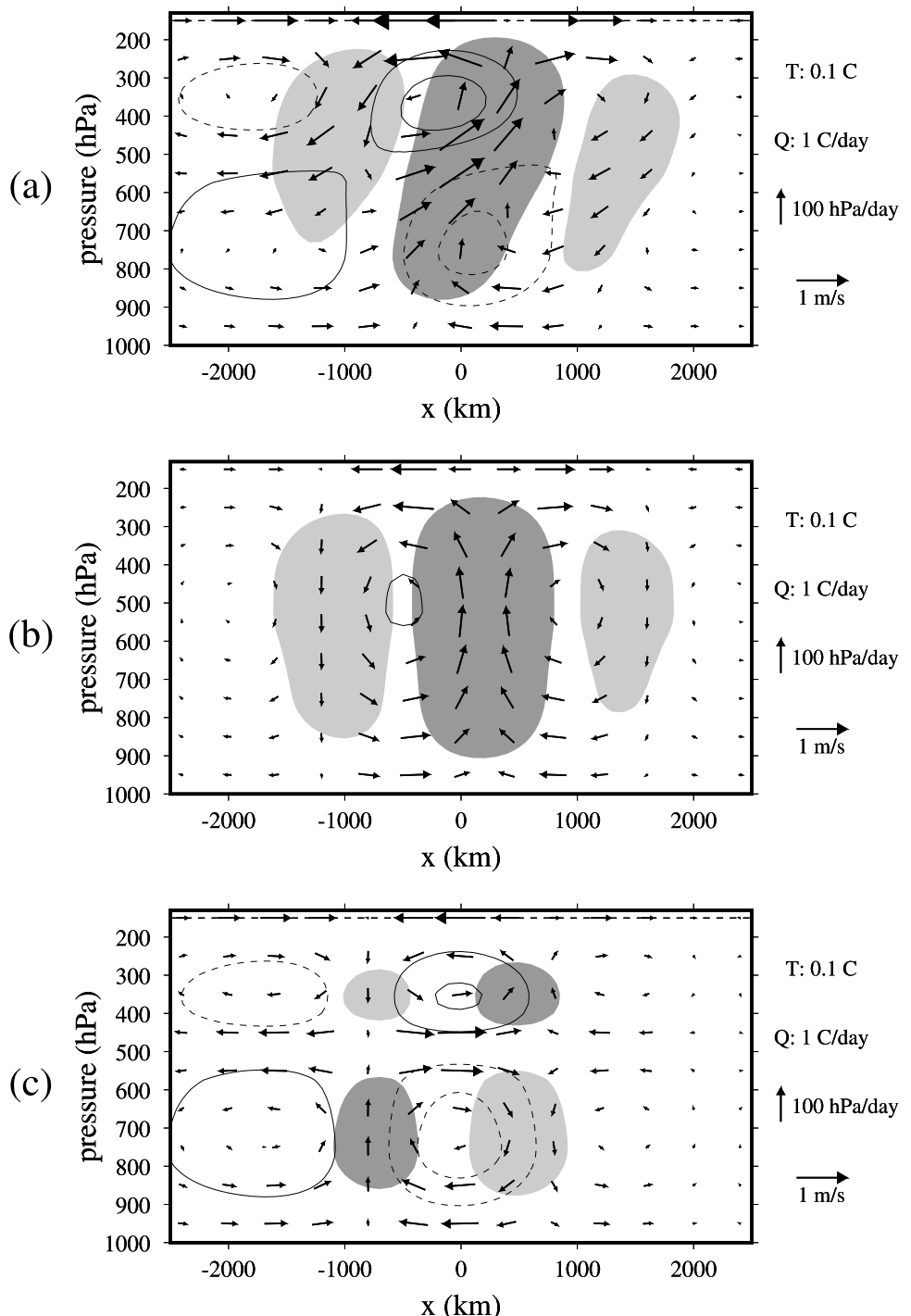


**Figure 22.** East–west vertical cross section of the response to moving the heat sources in Figure 21 to the west at  $16 \text{ m s}^{-1}$  through a linear primitive equation model (see section 11.2). (a) Both modes, (b) the  $49 \text{ m s}^{-1}$  mode, and (c) the  $23 \text{ m s}^{-1}$  mode. Perturbation temperature is contoured using a  $0.1 \text{ C}$  interval, solid (dashed) contours are positive (negative), and the zero contour is omitted. Perturbation heating amplitudes  $>1 \text{ C d}^{-1}$  are shaded, dark (light) for positive (negative) values. Vector scaling is to the right of each plot [from Haertel and Kiladis, 2004].

and Kiladis [2004] found that these terms were nearly balanced for the first mode but that heating only partially canceled vertical advection for the second mode, leading to its larger temperature signal. The degree of cancellation ( $\sim 95\%$  for the first mode and  $\sim 75\%$  for the second) was quantitatively consistent with the reduction of equivalent

depth of each mode to that observed in the waves. It was also found that the higher mode was crucial to the wave's moist enthalpy budget since its divergence structure ahead of convection (located at  $-800 \text{ km}$  in Figure 22c) is optimized to export low MSE air at midlevels, where mean MSE is low, and import it at lower and upper levels where

mean MSE is high, resulting in a column integrated increase in MSE [Haertel *et al.*, 2008]. Adding to the physical appeal of the vertical mode model is the strong relationship between the first mode and deep convective clouds and the leading (trailing) portion of the second mode with shallow and congestus (stratiform) clouds, based on COARE radar data.

### 11.3. Simple Coupled Wave Convection Models

[91] Recent modeling approaches have taken advantage of the observed self-similarity of CCEWs to construct physically based two-mode approaches to represent heating, with the second mode lagging the first, often by some specified interval (usually a few hours). Mapes [2000] used a two vertical mode setting to propose the “stratiform instability” mechanism to explain the relatively slow phase speeds of CCEWs, along with their tilted vertical structures. As a break from an adjustment scheme closure, particular significance is given to the effects of the second stratiform mode on *convective inhibition (CIN)*, which was shown to be crucial to the propagation speed of unstable modes of this model. The second mode controls CIN through its effect on lower troposphere temperature (as in Figure 22c), with less CIN when the lower tropospheric sounding is cold and therefore less stable. The role of CIN as a control on convection has some observational basis [e.g., Raymond *et al.*, 2003; Raymond and Fuchs, 2007].

[92] Alternate two-mode models were developed by Majda and Shefter [2001a, 2001b], Majda *et al.* [2004], and Khouider and Majda [2006a, 2006b, 2008], utilizing successively more complete “multicloud” parameterizations designed to account for the observed evolution of heating, moistening, and convective downdrafts in CCEWs. In the most recent versions of these models the second mode also plays a crucial role by moistening the boundary layer ahead of deep convection, with instability generated by a nonlinear switch tied to midlevel moistening by congestus clouds. A dependence of deep convection on midtropospheric moistening has observational support [Brown and Zhang, 1997; Sherwood, 1999] and is also the basis of a two-mode model by Kuang [2008]. In this model a large-scale “moisture-stratiform” instability is controlled by moistening of the midtroposphere, downplaying the role of CIN, while deep convection is, in turn, modulated by the temperature structure of the second mode, as shown by Mapes [2000].

[93] All of the two-mode models described above are characterized by convectively coupled gravity modes moving at  $15\text{--}20 \text{ m s}^{-1}$ , analogs of Kelvin waves in their nonrotating frameworks. While it might be assumed that the second mode is responsible for setting the relatively slow phase speed of the CCEWs in these simulations, the dry phase speed of the second mode is generally several  $\text{m s}^{-1}$  faster than the waves themselves so that a governing effect of gross moist stability cannot be ruled out. For example, Raymond and Fuchs [2007] developed a simple model which, by design, only supports a first-mode heating structure, and a simplified moist GCM by Frierson [2007]

also lacks a strong second-mode heating. Yet these models simulate Kelvin waves with realistic higher-mode vertical structures and phase speeds, and in both cases it is demonstrated that the scaling of the waves is set by the gross moist stability. Unstable growth in the former, linearized model is also dependent on CIN, as in the work by Mapes [2000].

[94] The success of the diverse approaches described above raises questions as to the optimal method to potentially improve CCEW simulation in more sophisticated GCM simulations, although they all point toward the need to better parameterize the effects of convection and its interaction with the large scale.

### 11.4. General Circulation Model Performance

[95] GCMs have long been capable of producing CCEW-like disturbances in the tropics. The vast majority of studies analyzing these disturbances, however, have focused on the MJO, although many of these MJO models are perhaps better categorized as “moist Kelvin waves” [e.g., Lau *et al.*, 1988] since their phase speeds are frequently too fast when compared to observations. In this section, we review the limited number of studies that assess GCM simulations of higher-frequency CCEWs and note that this is currently an area of active research.

[96] Hayashi [1974] performed a spectral analysis of zonal wind in the Geophysical Fluid Dynamics Laboratory GCM and found evidence of Kelvin, MRG, ER, and EWs. ER and EWs were also apparent in the model’s precipitation spectra, suggesting convective coupling, while coupled Kelvin and ER signals were less distinct. Lau *et al.* [1988] found evidence of an eastward moving wave in an idealized GCM, which was categorized as an MJO. However, its wave number 2–5 spectral peak in precipitation and its phase speed of  $18 \text{ m s}^{-1}$  suggest that it might have been more appropriately classified as a convectively coupled Kelvin wave. This disturbance exhibited many of the classic signatures of observed Kelvin waves, such as in-phase zonal wind and geopotential height fluctuations and low-level moisture and convergence leading precipitation and upward motion. Perhaps most importantly, individual precipitation elements did not propagate eastward at  $18 \text{ m s}^{-1}$ , as was the case in earlier models; rather, the eastward movement of the wave represented the successive development of new precipitation cells, as seen in observations (e.g., Figure 6). Horinouchi and Yoden [1998] also found evidence of Kelvin waves and  $n = 1$  WIG waves with realistic hierarchical structures in convection and equivalent depths of 20 m in the cumulus heating field of a GCM.

[97] Lin *et al.* [2006] calculated space-time spectra of tropical precipitation in 14 coupled GCMs participating in the Intergovernmental Panel on Climate Change (IPCC) Fourth Assessment Report (AR4), based on the WK99 methodology. Of the 14 models, roughly half had spectral peaks in or near the observed Kelvin and MRG bands, while few accurately captured spectral power in the ER and  $n = 1$  WIG bands. Interestingly, models that did have signals of CCEWs had phase speeds that were universally too fast, and

their equivalent depths were in the 50–90 m range rather than the observed 12–50 m, suggestive of a common bias in physical parameterization across models.

[98] Apart from its utility in identifying the disturbances and their scales within a given model, the space-time spectral approach is also an efficient way to determine whether a model has a reasonable representation of the overall “background” variability. *Lin et al.* [2006] speculated that problems with convective parameterization, particularly gross moist stabilities that were too large, were the source of the discrepancy between models and observations. Spectra that are too red in most of the models suggested that convective self-suppression processes need to be further incorporated into GCM parameterizations, such as the inclusion of unsaturated convective downdrafts that lead to CIN via the “cold pool” boundary layer temperature signals in observed CCEWs (see Figures 8b, 10b, 14b, and 16c). Furthermore, it is well documented that GCMs in general lack the “top heavy” heating profiles observed in nature, presumably because of improper treatment of stratiform precipitation and its duration and timing relative to deep convection [e.g., *Lin et al.*, 2004].

[99] Since GCMs are so complex, it has been a challenge to diagnose precisely why they have deficiencies in representing CCEWs. *Frierson* [2007] analyzed a particularly robust convectively coupled Kelvin wave with a reasonable propagation speed in an “intermediate” GCM that used the full primitive equations, an aquaplanet boundary condition, and idealized parameterizations of radiation and moisture. The primary sensitivity in this model was the overall gross moist stability, even to the extent that reasonably scaled Kelvin waves appeared when shallow convection and stratiform precipitation played less of a role than presumed in nature. Similarly, *Lin et al.* [2008] tested a variety of convective parameterization schemes and “trigger functions,” which restrict the onset of convection on the basis of the amount of available moisture. They found that a stronger moisture trigger decreased the wave speeds and increased their variance toward observed values by strengthening higher vertical mode contributions from the “large-scale condensation” over the deep convection schemes. The strength and speed of GCM-generated CCEWs also depended realistically on the gross moist stability. Similarly, *Suzuki et al.* [2006] found that a trigger function was necessary to produce a reasonable spectrum of CCEWs in their GCM, which uses an adjustment scheme convective parameterization. Inclusion of the trigger function altered the dependence of deep convection from one controlled by CAPE (as in SQE) to one controlled by free tropospheric humidity and also produced quite realistic wave dynamical structures. In some respects a trigger function may be viewed as acting as a rough proxy for CIN by allowing more moisture to build up ahead of deep convection, resulting in stronger coupling between precipitation, moisture, and the wave.

[100] An analysis by *Yang et al.* [2009] suggests that even in models that are able to simulate CCEWs with partial success, they fail to capture the observed geographical

distribution of wave activity and do not necessarily produce waves with horizontal and vertical structures resembling observations. Detailed diagnosis of CCEWs in GCMs is just now beginning and will no doubt continue as a means to explore the improvement of model physical parameterizations.

### 11.5. Cloud-Resolving Models

[101] Another class of models known as cloud-resolving models (CRMs) attempts to explicitly represent cloud-scale motions and their diabatic effects. In CRMs, cloud micro-physics, boundary layer processes, and radiation are generally still parameterized, although individual cloud elements and their evolution are more explicitly represented than in other models. CRMs require high temporal and spatial resolution, with <10 km grid spacing, so three-dimensional versions have typically only been run over limited regions driven by realistic fluctuations along their boundaries, or over periodic domains.

[102] Many CRMs spontaneously develop CCEWs and, in particular, convectively coupled gravity waves [e.g., *Grabowski and Moncrieff*, 2001; *Peters and Bretherton*, 2006; *Tulich et al.*, 2007] or Kelvin waves when rotation is included [e.g., *Kuang et al.*, 2005; *Shutts*, 2006]. These waves have realistic phase speeds and multimode vertical structures and tilts and develop through the upscale organization of MCSs without any a priori assumptions of scale selection or vertical modes.

[103] As in GCMs, detailed analyses of the dynamics of CCEWs in complex CRMs is problematic, although progress has recently been made in this area. For example, *Tulich et al.* [2007] and *Tulich and Mapes* [2008] simulated quite realistic convectively coupled gravity waves in a two-dimensional CRM, with a hierarchy of convective organization much like that seen in Figures 6 and 19. The vertical structures of the large-scale wave envelopes broadly match those shown here for CCEWs (e.g., Figure 8), down to the two-tiered tilted tropospheric temperature configuration, near-surface cold pools below regions of deepest convection, and the gradual moistening of the lower troposphere by shallow convection ahead of the waves. The wave structures projected onto multiple vertical modes, and it was demonstrated that the triggering of new convective envelopes occurred through MCS gust fronts and cold pools, along with low level destabilization by propagating gravity wave packets. These packets were preferentially excited by both deep convective and higher-mode (stratiform) heating profiles, with CIN induced by profiles of the opposite sign also playing an important role in determining the propagation speed of large-scale envelopes. These processes were interpreted as an affirmation of the basic stratiform instability mechanism, with convective triggering and suppression essentially governed by the lower tropospheric temperature structure induced by the propagation and interaction of multiple vertical mode wave packets.

[104] Recently, short-duration CRM runs have been done using global domains [e.g., *Tomita et al.*, 2005; *Nasuno et al.*, 2008]. Runs with grid spacings of 7.0 and 3.5° spontaneously develop CCEWs, and especially MJO-like

features and Kelvin waves, although their phase speeds appear to be somewhat too fast. Future analysis of CCEWs, as well as efforts to improve convective parameterization in GCMs, will certainly rely heavily on CRMs, especially as computing power increases to the point of routinely running these models on global domains.

## 12. REAL-TIME MONITORING AND FORECAST APPLICATIONS

[105] An ultimate goal of meteorological research is its application to forecasting. The previous sections of this review have provided evidence of the importance of CCEWs in modulating tropical clouds and convection, their role in determining tropical circulation variability, and their simulation by numerical models. But to what extent are CCEWs useful for weather forecasting?

[106] Skill in tropical weather forecasting has traditionally lagged that in midlatitudes, and current daily to weekly tropical forecasts have only modest credibility, at best, with the majority of users [Smith *et al.*, 2001]. While this is partly a consequence of the highly convective nature of tropical weather, the poorer performance of numerical models in the tropics and the limited number of conceptual models for forecasters are also blamed [Smith *et al.*, 2001]. Perhaps adding to this lagging skill, the use of CCEWs as conceptual models by forecasters has yet to reach the mainstream. However, the extent to which CCEWs may successfully be used for tropical forecasting, independently of numerical model guidance, is still mostly uncertain [Molinari *et al.*, 2006].

[107] Support for an important role of CCEWs for forecasting comes from the case studies cited here that have demonstrated an influence on actual tropical weather events [Straub and Kiladis, 2002; Sobel *et al.*, 2004; Wheeler and McBride, 2005; Straub *et al.*, 2006]. However, the geographical range of the direct influence of CCEWs is somewhat limited (Figure 5). The direct impact of Kelvin waves on convection, for example, is confined to within  $\sim 10^\circ$  of the equator (Figure 5a), while that for  $n = 1$  ER waves is currently thought to be limited to the Indian and west Pacific ocean basins (Figure 5b). The use of CCEWs in the forecast process is also hampered by the extent to which they can be detected in real time. The filtering typically employed to extract the waves in research studies is applied after the fact, i.e., using a filtering procedure for which all future times of a data set are effectively known (e.g., section 3). Wheeler and Weickmann [2001] investigated a “real-time filtering” approach, whereby OLR filtering is performed on anomaly data with zero-padding applied to all future times, and then made predictions through simple extrapolation. Forecast skill of this approach depends on wave type, extending out to about half the typical period of each wave. This has been continuously provided on the World Wide Web, with a daily update frequency, since 1999 (e.g., [http://www.cdc.noaa.gov/map/clim/olr\\_modes/](http://www.cdc.noaa.gov/map/clim/olr_modes/)). While this tool has received a fair amount of attention among researchers and some forecasters, the extent to which

it has been applied successfully for forecasting has not been documented. One aspect requiring improvement is the time it takes for the global OLR data to become available. Currently, this takes  $\sim 12$  h, and at present, there is also no use of wind data.

[108] One obvious forecast application for CCEWs is through their association with tropical cyclones (TCs), as has been discussed individually for each wave type in sections 4–9. TCs preferentially occur within certain phases of some of the waves, usually within the regions of off-equatorial wave-enhanced convective activity and/or low level cyclonic vorticity [Dickinson and Molinari, 2002; Bessafi and Wheeler, 2006; Frank and Roundy, 2006; Molinari *et al.*, 2007]. Where TC modulation occurs (shown schematically in Figure 5) there is good potential for the improvement of intraseasonal TC activity forecasting [Leroy and Wheeler, 2008] (see also <http://www.atmos.albany.edu/facstaff/roundy/tcforecast/tcforecast.html>).

[109] Another aspect of CCEWs relevant for forecasting is their incorporation into numerical forecast models and the focus that they provide for tropical numerical prediction. Žagar *et al.* [2004, 2005], for example, demonstrated improvements in model initialization over the tropics by projecting observations onto the theoretical structures of CCEWs [Yang *et al.*, 2003] under the constraint of four-dimensional variational data assimilation. Such approaches will undoubtedly lead to future improvements in tropical forecasts of CCEW impacts.

## 13. OUTLOOK

[110] The prediction and subsequent discovery of equatorially trapped modes in the atmosphere and ocean during the 1960s and 1970s provides a prime example of the success of mathematical theory in geophysics. The success of Matsuno’s [1966] linear theory has resulted in relatively straightforward interpretation of equatorial wave dynamics and their impacts on circulations, especially for the dry modes of the middle atmosphere. While the basic structure and dispersive characteristics of CCEWs correspond to a large degree to Matsuno’s [1966] SW solutions, the complication of coupling to moist processes poses remaining challenges. It seems evident that CCEWs should be easier to understand and simulate than the MJO, and so it may seem surprising that the volume of literature on the MJO is more extensive than that on CCEWs. This is likely attributable to the fact that the MJO has a more obvious impact on tropical and extratropical weather because of its larger scale and lower frequency, which also made it easier to detect in early observations.

[111] CCEWs at times compose a large portion of the MJO and other large-scale convective envelopes and are themselves composed of smaller-scale MCSs; thus, an assessment of this wave-wave interdependence appears to be a crucial step toward understanding the maintenance of large-scale tropical circulations [Moncrieff, 2004]. The observed structural self-similarity across scales provides a framework to explore the implications of these interactions

in simplified models [Majda, 2007], although it raises yet unresolved questions about the physical significance of projecting the life cycles of individual MCSs onto larger scales [Mapes et al., 2006].

[112] The relative roles of moist processes and the concept of gross moist stability versus higher-mode vertical structure in determining the scale of CCEWs are not yet evident. The fact that analogs to CCEWs can be reproduced in simple numerical models and CRMs holds promise that many of these issues will soon be resolved, leading to overall improvement of the handling of moist tropical waves in GCMs used for operational forecasting and climate studies.

[113] In this article we have reviewed the historical development leading up to the current state of knowledge of CCEWs and provided an assessment of their impacts on day-to-day variability on synoptic-scale weather within the tropics. Although not every aspect of CCEWs has been covered in detail, we have attempted to highlight some of the outstanding remaining research problems along with appropriate references for further reading. As evidenced by the ever-increasing number of journal articles on CCEWs, there appears little doubt that they will continue to be of great interest to researchers well into the future.

## GLOSSARY

**Available potential energy (APE):** In a closed system, the maximum amount of kinetic energy available by an adiabatic redistribution of mass to a statically stable state of rest.

**Convective available potential energy (CAPE):** The maximum amount of kinetic energy generated by lifting subcloud air from its level of free convection to its level of neutral buoyancy.

**Convective inhibition (CIN):** A measure of shallow stability, generally assumed to be the energy required to lift an air parcel within the boundary layer to its level of free convection.

**Convectively coupled equatorial wave (CCEW):** An equatorially trapped wave in which deep convection is coupled to the wave's large-scale circulation and thermodynamical field.

**Dry (or "free") mode:** A wave that is uncoupled to convection or any other steady forcing.

**Gross moist stability:** The reduced stability that a large-scale convecting atmosphere "feels" because of the partial cancellation of convective heating and adiabatic cooling in regions of ascent.

**Intertropical Convergence Zone (ITCZ):** A narrow region where the trade winds meet from either hemisphere, generally oriented along or parallel to the equator, and characterized by a high frequency of transient deep convection.

**Madden-Julian oscillation (MJO):** A quasiperiodic, planetary-scale envelope of deep convection coupled to a large-scale circulation pattern which propagates eastward at

around 5 m/s and dominates the intraseasonal (30–90 day) variability of the tropical atmosphere.

**Mesoscale convective system (MCS):** The largest entity of an organized, individual convective cloud system, consisting of an ensemble of cumulonimbus clouds producing a contiguous mesoscale area of rainfall on the order of 100 km or more in horizontal scale in at least one direction, lasting from several hours to at most a couple of days.

**Quasi-equilibrium (QE):** The general assumption that the amount of convection adjusts relatively quickly to the generation of convective instability in a large-scale, statistical sense.

**Radiation upper boundary condition:** A specification which allows wave energy to be radiated through the upper boundary of a model rather than being reflected.

**Rossby radius of deformation:** The horizontal scale at which rotation effects become as important as buoyancy effects.

**Shallow water (SW) equations:** A set of equations governing an incompressible, constant density fluid in which the horizontal scale of the flow is much greater than the layer depth.

**Strict quasi-equilibrium (SQE):** A quasi-equilibrium formulation in which convection adjusts relatively quickly (within hours) to local changes in CAPE, resulting in virtual temperature profiles along a moist adiabat tied to boundary layer equivalent potential temperature.

**Wave conditional instability of the second kind (wave-CISK):** A positive feedback process whereby wave-induced low level convergence produces convective heating, leading to further convergence and convection, generating available potential energy and amplifying the wave.

[114] **ACKNOWLEDGMENTS.** We thank Gerald North for motivating the writing of this article and Adam Sobel, Guiying Yang, and an anonymous reviewer for valuable comments that helped clarify several aspects of the original manuscript.

[115] The Editor responsible for this paper was Gerald North. He thanks Adam Sobel and one other anonymous technical reviewer.

## REFERENCES

- Aiyer, A. R., and J. Molinari (2003), Evolution of mixed Rossby-gravity waves in idealized MJO environments, *J. Atmos. Sci.*, 60, 2837–2855, doi:10.1175/1520-0469(2003)060<2837:EOMRWI>2.0.CO;2.
- American Meteorological Society (2000), *Glossary of Meteorology*, 855 pp., doi:10.2172/764692, Boston, Mass.
- Andrews, D. G., J. R. Holton, and C. B. Leovy (1987), *Middle Atmosphere Dynamics*, 489 pp., Academic, San Diego, Calif.
- Arakawa, A., and W. H. Schubert (1974), Interaction of a cumulus cloud ensemble with the large-scale environment, *J. Atmos. Sci.*, 31, 674–701, doi:10.1175/1520-0469(1974)031<0674:IOACCE>2.0.CO;2.
- Baldwin, M. P., et al. (2001), The quasi-biennial oscillation, *Rev. Geophys.*, 39, 179–229, doi:10.1029/1999RG000073.
- Benedict, J. J., and D. A. Randall (2007), Observed characteristics of the MJO relative to maximum rainfall, *J. Atmos. Sci.*, 64, 2332–2354, doi:10.1175/JAS3968.1.

- Bessafi, M., and M. C. Wheeler (2006), Modulation of South Indian Ocean tropical cyclones by the Madden-Julian oscillation and convectively coupled equatorial waves, *Mon. Weather Rev.*, **134**, 638–656, doi:10.1175/MWR3087.1.
- Betts, A. K., and M. J. Miller (1986), A new convective adjustment scheme. Part II: Single column tests using GATE wave, BOMEX, ATEx, and arctic air-mass data sets, *Q. J. R. Meteorol. Soc.*, **112**, 693–709.
- Bhat, G. S., J. Srinivasan, and S. Gadgil (1996), Tropical deep convection, convective available potential energy, and sea surface temperature, *J. Meteorol. Soc. Jpn.*, **74**, 155–166.
- Booker, J. R., and F. P. Bretherton (1967), The critical layer for internal gravity waves in a shear flow, *J. Fluid Mech.*, **27**, 513–519, doi:10.1017/S0022112067000515.
- Bretherton, F. P. (1964), Low frequency oscillations trapped near the equator, *Tellus*, **16**, 181–185.
- Brown, R. G., and C. S. Bretherton (1997), A test of the strict quasi-equilibrium theory on long space and time scales, *J. Atmos. Sci.*, **54**, 624–638, doi:10.1175/1520-0469(1997)054<0624:ATOTSQ>2.0.CO;2.
- Brown, R. G., and C. Zhang (1997), Variability of midtropospheric moisture and its effect on cloud-top height distribution during TOGA COARE, *J. Atmos. Sci.*, **54**, 2760–2774, doi:10.1175/1520-0469(1997)054<2760:VOMMAI>2.0.CO;2.
- Chang, C.-P. (1970), Westward propagating cloud patterns in the tropical Pacific as seen from time-composite satellite photographs, *J. Atmos. Sci.*, **27**, 133–138, doi:10.1175/1520-0469(1970)027<0133:WPCPIT>2.0.CO;2.
- Chang, C.-P., J. M. Chen, P. A. Carr, and L. E. Harr (1996), Northwestward-propagating wave patterns over the tropical western North Pacific during summer, *Mon. Weather Rev.*, **124**, 2245–2266, doi:10.1175/1520-0493(1996)124<2245:NWPWOT>2.0.CO;2.
- Chao, W. C. (2007), Chimeric equatorial waves as a better descriptor for “convectively coupled equatorial waves,” *J. Meteorol. Soc. Jpn.*, **85**, 521–524, doi:10.2151/jmsj.85.521.
- Chatterjee, P., and B. N. Goswami (2004), Structure, genesis and scale selection of the tropical quasi-biweekly mode, *Q. J. R. Meteorol. Soc.*, **130**, 1171–1194.
- Chen, S. S., and R. A. Houze (1997), Diurnal variation and life cycle of deep convective systems over the tropical Pacific warm pool, *Q. J. R. Meteorol. Soc.*, **123**, 357–388, doi:10.1002/qj.49712353806.
- Chen, S. S., R. A. Houze, and B. E. Mapes (1996), Multiscale variability of deep convection in relation to large-scale circulation in TOGA COARE, *J. Atmos. Sci.*, **53**, 1380–1409, doi:10.1175/1520-0469(1996)053<1380:MVODCI>2.0.CO;2.
- Cho, H.-K., K. P. Bowman, and G. R. North (2004), Equatorial waves including the Madden-Julian Oscillation in TRMM rainfall and OLR data, *J. Clim.*, **17**, 4387–4406, doi:10.1175/3215.1.
- Ciesielski, P. E., R. H. Johnson, P. T. Haertel, and J. Wang (2003), Corrected TOGA COARE sounding humidity data: Impact on diagnosed properties of convection and climate over the warm pool, *J. Clim.*, **16**, 2370–2384, doi:10.1175/2790.1.
- Clayson, C. A., B. Strahl, and J. M. Schrage (2002), 2–3-day convective variability in the tropical western Pacific, *Mon. Weather Rev.*, **130**, 529–548, doi:10.1175/1520-0493(2002)130<0529:DCVITT>2.0.CO;2.
- Crum, F. X., and T. J. Dunkerton (1992), Analytic and numerical models of wave-CISK with conditional heating, *J. Atmos. Sci.*, **49**, 1693–1708, doi:10.1175/1520-0469(1992)049<1693:AANMOW>2.0.CO;2.
- Dickinson, M., and J. Molinari (2002), Mixed Rossby-gravity waves and western Pacific tropical cyclogenesis. Part I: Synoptic evolution, *J. Atmos. Sci.*, **59**, 2183–2196, doi:10.1175/1520-0469(2002)059<2183:MRGAW>2.0.CO;2.
- Dunkerton, T. J. (1993), Observation of 3–6-day meridional wind oscillations over the tropical Pacific, 1973–1992: Vertical structure and interannual variability, *J. Atmos. Sci.*, **50**, 3292–3307, doi:10.1175/1520-0469(1993)050<3292:OODMWO>2.0.CO;2.
- Dunkerton, T. J., and M. P. Baldwin (1995), Observation of 3–6 day meridional wind oscillations over the tropical Pacific, 1973–1992: Horizontal structure and propagation, *J. Atmos. Sci.*, **52**, 1585–1601.
- Dunkerton, T. J., and F. X. Crum (1995), Eastward propagating ~2- to 15-day equatorial convection and its relation to the tropical intraseasonal oscillation, *J. Geophys. Res.*, **100**, 25,781–25,790, doi:10.1029/95JD02678.
- Dunn, G. E. (1940), Cyclogenesis in the tropical Atlantic, *Bull. Am. Meteorol. Soc.*, **21**, 215–229.
- Emanuel, K. A. (2007), Quasi-equilibrium dynamics of the tropical atmosphere, in *The Global Circulation of the Atmosphere*, edited by T. Schneider and A. H. Sobel, pp. 186–218, Princeton Univ. Press, Princeton, N. J.
- Emanuel, K. A., J. D. Neelin, and C. S. Bretherton (1994), On large-scale circulations in convecting atmospheres, *Q. J. R. Meteorol. Soc.*, **120**, 1111–1143, doi:10.1002/qj.49712051902.
- Ern, M., P. Preusse, M. Krebsbach, M. G. Mlynczak, and J. M. Russell (2008), Equatorial wave analysis from SABER and ECMWF temperature, *Atmos. Chem. Phys.*, **8**, 845–869.
- Eskridge, R. E., O. A. Alduchov, I. V. Chernykh, Z. Panmao, A. C. Polansky, and S. R. Doty (1995), A comprehensive aerological reference data set: Rough and systematic errors, *Bull. Am. Meteorol. Soc.*, **76**, 1759–1775, doi:10.1175/1520-0477(1995)076<1759:ACARDS>2.0.CO;2.
- Farrell, B., and I. Watterson (1985), Rossby waves in opposing currents, *J. Atmos. Sci.*, **42**, 1746–1756, doi:10.1175/1520-0469(1985)042<1746:RWIOC>2.0.CO;2.
- Flatau, M. K., P. J. Flatau, J. Schmidt, and G. N. Kiladis (2003), Delayed onset of the 2002 Indian monsoon, *Geophys. Res. Lett.*, **30**(14), 1768, doi:10.1029/2003GL017434.
- Frank, W. M., and P. E. Roundy (2006), The role of tropical waves in tropical cyclogenesis, *Mon. Weather Rev.*, **113**, 647–658.
- Frierson, D. M. W. (2007), Convectively coupled Kelvin waves in an idealized moist general circulation model, *J. Atmos. Sci.*, **64**, 2076–2090, doi:10.1175/JAS3945.1.
- Fulton, S. R., and W. H. Schubert (1985), Vertical normal mode transforms: Theory and application, *Mon. Weather Rev.*, **113**, 2397–2417.
- Garcia, R. R., and M. L. Salby (1987), Transient response to localized episodic heating in the tropics. Part II: Far-field behavior, *J. Atmos. Sci.*, **44**, 499–530, doi:10.1175/1520-0469(1987)044<0499:TRTLEH>2.0.CO;2.
- Gill, A. E. (1980), Some simple solutions for heat-induced tropical circulation, *Q. J. R. Meteorol. Soc.*, **106**, 447–462, doi:10.1002/qj.49710644905.
- Gill, A. E. (1982a), *Atmosphere-Ocean Dynamics*, 662 pp., Academic, San Diego, Calif.
- Gill, A. E. (1982b), Studies of moisture effects in simple atmospheric models: The stable case, *Geophys. Astrophys. Fluid Dyn.*, **19**, 119–152, doi:10.1080/03091928208208950.
- Grabowski, W. W., and M. W. Moncrieff (2001), Large-scale organization of tropical convection in two-dimensional explicit numerical simulations, *Q. J. R. Meteorol. Soc.*, **127**, 445–468, doi:10.1002/qj.49712757211.
- Gruber, A. (1974), The wavenumber-frequency spectra of satellite-measured brightness in the tropics, *J. Atmos. Sci.*, **31**, 1675–1680, doi:10.1175/1520-0469(1974)031<1675:TWFOS>2.0.CO;2.
- Haertel, P. T., and R. H. Johnson (1998), Two-day disturbances in the equatorial western Pacific, *Q. J. R. Meteorol. Soc.*, **124**, 615–636, doi:10.1002/qj.49712454611.
- Haertel, P. T., and G. N. Kiladis (2004), On the dynamics of two-day equatorial disturbances, *J. Atmos. Sci.*, **61**, 2707–2721, doi:10.1175/JAS3352.1.
- Haertel, P. T., G. N. Kiladis, A. Denno, and T. Rickenbach (2008), Vertical mode decompositions of 2-day waves and the Madden-

- Julian oscillation, *J. Atmos. Sci.*, 65, 813–833, doi:10.1175/2007JAS2314.1.
- Hall, N. M. J., G. N. Kiladis, and C. D. Thorncroft (2006), Three dimensional structure and dynamics of African easterly waves. Part II: Dynamical modes, *J. Atmos. Sci.*, 63, 2231–2245, doi:10.1175/JAS3742.1.
- Hayashi, Y. (1970), A theory of large-scale equatorial waves generated by condensation heat and accelerating the zonal wind, *J. Meteorol. Soc. Jpn.*, 48, 140–160.
- Hayashi, Y. (1974), Spectral analysis of tropical disturbances appearing in a GFDL general circulation model, *J. Atmos. Sci.*, 31, 180–218, doi:10.1175/1520-0469(1974)031<0180:SAOTDA>2.0.CO;2.
- Hendon, H. H., and B. Liebmann (1991), The structure and annual variation of antisymmetric fluctuations of tropical convection and their association with Rossby-gravity waves, *J. Atmos. Sci.*, 48, 2127–2140, doi:10.1175/1520-0469(1991)048<2127:TSAAVO>2.0.CO;2.
- Hendon, H. H., and B. Liebmann (1994), Organization of convection within the Madden-Julian oscillation, *J. Geophys. Res.*, 99, 8073–8083, doi:10.1029/94JD00045.
- Hendon, H. H., and M. L. Salby (1994), The life cycle of the Madden Julian oscillation, *J. Atmos. Sci.*, 51, 2225–2237.
- Hendon, H. H., and M. C. Wheeler (2008), Some space-time spectral analyses of tropical convection and planetary-scale waves, *J. Atmos. Sci.*, 65, 2936–2948, doi:10.1175/2008JAS2675.1.
- Hodges, K. I., D. W. Chappell, G. J. Robinson, and G. Yang (2000), An improved algorithm for generating global window brightness temperatures from multiple satellite infrared imagery, *J. Atmos. Oceanic Technol.*, 17, 1296–1312, doi:10.1175/1520-0426(2000)017<1296:AIAFGG>2.0.CO;2.
- Holland, G. J. (1995), Scale interaction in the western Pacific monsoon, *Meteorol. Atmos. Phys.*, 56, 57–59, doi:10.1007/BF01022521.
- Holloway, C. E., and J. D. Neelin (2007), The convective cold top and quasi-equilibrium, *J. Atmos. Sci.*, 64, 1467–1487, doi:10.1175/JAS3907.1.
- Holton, J. R. (1970), A note on forced equatorial waves, *Mon. Weather Rev.*, 98, 614–615, doi:10.1175/1520-0493(1970)098<0614:ANOFEW>2.3.CO;2.
- Holton, J. R. (1971), A diagnostic model for equatorial wave disturbances: The role of vertical shear of the mean zonal wind, *J. Atmos. Sci.*, 28, 55–64, doi:10.1175/1520-0469(1971)028<0055:ADMFEW>2.0.CO;2.
- Holton, J. R. (1972), Waves in the equatorial stratosphere generated by tropospheric heat sources, *J. Atmos. Sci.*, 29, 368–375, doi:10.1175/1520-0469(1972)029<0368:WITESG>2.0.CO;2.
- Holton, J. R. (1973), On the frequency distribution of atmospheric Kelvin waves, *J. Atmos. Sci.*, 30, 499–501, doi:10.1175/1520-0469(1973)030<0499:OTFDOA>2.0.CO;2.
- Holton, J. R. (2004), *An Introduction to Dynamic Meteorology*, 4th ed., 535 pp., Elsevier Academic, Burlington, Mass.
- Horiuchi, T., and S. Yoden (1998), Wave-mean flow interaction associated with a QBO like oscillation in a simplified GCM, *J. Atmos. Sci.*, 55, 502–526, doi:10.1175/1520-0469(1998)055<0502:WMFIW>2.0.CO;2.
- Hoskins, B. J., and B. Wang (2006), Large-scale atmospheric dynamics, in *The Asian Monsoon*, edited by B. Wang, chap. 9, pp. 357–415, Springer, New York.
- Hoskins, B. J., and G.-Y. Yang (2000), The equatorial response to higher-latitude forcing, *J. Atmos. Sci.*, 57, 1197–1213, doi:10.1175/1520-0469(2000)057<1197:TERTHL>2.0.CO;2.
- Houze, R. A., Jr. (2004), Mesoscale convective systems, *Rev. Geophys.*, 42, RG4003, doi:10.1029/2004RG000150.
- Hsieh, J.-S., and K. H. Cook (2005), Generation of African easterly wave disturbances: Relationship to the African easterly jet, *Mon. Weather Rev.*, 133, 1311–1327, doi:10.1175/MWR2916.1.
- Hsieh, J.-S., and K. H. Cook (2007), A study of the energetics of African easterly waves using a regional climate model, *J. Atmos. Sci.*, 64, 421–440, doi:10.1175/JAS3851.1.
- Johnson, R. H., T. M. Rickenbach, S. A. Rutledge, P. E. Ciesielski, and W. H. Schubert (1999), Trimodal characteristics of tropical convection, *J. Clim.*, 12, 2397–2418, doi:10.1175/1520-0442(1999)012<2397:TCOTC>2.0.CO;2.
- Kasahara, A. (2000), On the origin of cumulus parameterization for numerical prediction models, in *General Circulation Model Development, Past, Present and Future*, edited by D. A. Randall, pp. 199–224, Academic, San Diego, Calif.
- Keen, R. A. (1982), The role of cross-equatorial tropical cyclone pairs in the Southern Oscillation, *Mon. Weather Rev.*, 110, 1405–1416, doi:10.1175/1520-0493(1982)110<1405:TROCE>2.0.CO;2.
- Kemball-Cook, S. R., and B. Wang (2001), Equatorial waves and air-sea interaction in the boreal summer intraseasonal oscillation, *J. Clim.*, 14, 2923–2942, doi:10.1175/1520-0442(2001)014<2923:EWAASI>2.0.CO;2.
- Khouider, B., and A. J. Majda (2006a), A simple multicloud parameterization for convectively coupled waves. Part I: Linear analysis, *J. Atmos. Sci.*, 63, 1308–1323, doi:10.1175/JAS3677.1.
- Khouider, B., and A. J. Majda (2006b), Model multi-cloud parameterizations for convectively coupled waves: Detailed nonlinear wave evolution, *Dyn. Atmos. Oceans*, 42, 59–80, doi:10.1016/j.dynatmoce.2005.12.001.
- Khouider, B., and A. J. Majda (2008), Multi-cloud models for organized tropical convection: Enhanced congestus heating, *J. Atmos. Sci.*, 65, 895–914, doi:10.1175/2007JAS2408.1.
- Kiladis, G. N. (1998), Observations of Rossby waves linked to convection over the eastern tropical Pacific, *J. Atmos. Sci.*, 55, 321–339, doi:10.1175/1520-0469(1998)055<0321:OORWLT>2.0.CO;2.
- Kiladis, G. N., and M. Wheeler (1995), Horizontal and vertical structure of observed tropospheric equatorial Rossby waves, *J. Geophys. Res.*, 100, 22,981–22,997, doi:10.1029/95JD02415.
- Kiladis, G. N., K. H. Straub, and P. T. Haertel (2005), Zonal and vertical structure of the Madden-Julian oscillation, *J. Atmos. Sci.*, 62, 2790–2809, doi:10.1175/JAS3520.1.
- Kiladis, G. N., C. D. Thorncroft, and N. M. J. Hall (2006), Three dimensional structure and dynamics of African easterly waves. Part I: Observations, *J. Atmos. Sci.*, 63, 2212–2230, doi:10.1175/JAS3741.1.
- Krouse, K. D., A. H. Sobel, and L. M. Polvani (2008), On the wavelength of Rossby waves radiated by tropical cyclones, *J. Atmos. Sci.*, 65, 644–654, doi:10.1175/2007JAS2402.1.
- Kuang, Z. (2008), A moisture-stratiform instability for convectively coupled waves, *J. Atmos. Sci.*, 65, 834–854, doi:10.1175/2007JAS2444.1.
- Kuang, Z., P. N. Blossey, and C. S. Bretherton (2005), A new approach for 3D cloud-resolving simulations of large-scale atmospheric circulation, *Geophys. Res. Lett.*, 32, L02809, doi:10.1029/2004GL021024.
- Kuo, H.-C., J.-H. Chen, R. T. Williams, and C.-P. Chang (2001), Rossby waves in zonally opposing mean flow: Behavior in northwest Pacific summer monsoon, *J. Atmos. Sci.*, 58, 1035–1050.
- Kuo, H.-L. (1974), Further studies of the parameterization of the influence of cumulus convection on large-scale flow, *J. Atmos. Sci.*, 31, 1232–1240, doi:10.1175/1520-0469(1974)031<1232:FSOTPO>2.0.CO;2.
- Lau, K.-H., and N.-C. Lau (1990), Observed structure and propagation characteristics of tropical summertime synoptic scale disturbances, *Mon. Weather Rev.*, 118, 1888–1913, doi:10.1175/1520-0493(1990)118<1888:OSAPCO>2.0.CO;2.
- Lau, K.-H., and N.-C. Lau (1992), The energetics and propagation dynamics of tropical summertime synoptic-scale disturbances, *J. Clim.*, 120, 2523–2539.

- Lau, N.-C., I. M. Held, and J. D. Neelin (1988), The Madden-Julian Oscillation in an idealized general circulation model, *J. Atmos. Sci.*, **45**, 3810–3832.
- Leroy, A., and M. C. Wheeler (2008), Statistical prediction of weekly tropical cyclone activity in the Southern Hemisphere, *Mon. Weather Rev.*, **136**, 3637–3654, doi:10.1175/2008MWR2426.1.
- Liebmann, B., and H. H. Hendon (1990), Synoptic-scale disturbances near the equator, *J. Atmos. Sci.*, **47**, 1463–1479, doi:10.1175/1520-0469(1990)047<1463:SSDNTE>2.0.CO;2.
- Liebmann, B., and C. A. Smith (1996), Description of a complete (interpolated) OLR dataset, *Bull. Am. Meteorol. Soc.*, **77**, 1275–1277.
- Liebmann, B., H. H. Hendon, and J. D. Glick (1997), On the generation of two-day convective disturbances across the western equatorial Pacific, *J. Meteorol. Soc. Jpn.*, **75**, 939–946.
- Liebmann, B., G. N. Kiladis, L. M. V. Carvalho, C. Jones, C. S. Vera, I. Bladé, and D. Allured (2009), Origin of convectively coupled Kelvin waves over South America, *J. Clim.*, **22**, 300–315.
- Lin, J., B. E. Mapes, M. Zhang, and M. Newman (2004), Stratiform precipitation, vertical heating profiles, and the Madden-Julian oscillation, *J. Atmos. Sci.*, **61**, 296–309, doi:10.1175/1520-0469(2004)061<0296:SPVHPA>2.0.CO;2.
- Lin, J.-L., et al. (2006), Tropical intraseasonal variability in 14 IPCC AR4 climate models. Part I: Convective signals, *J. Clim.*, **19**, 2665–2690, doi:10.1175/JCLI3735.1.
- Lin, J.-L., M.-I. Lee, D. Kim, I.-S. Kang, and D. M. W. Frierson (2008), The impacts of convective parameterization and moisture triggering on AGCM-simulated convectively coupled equatorial waves, *J. Clim.*, **21**, 883–909, doi:10.1175/2007JCLI1790.1.
- Lindzen, R. S. (1967), Planetary waves on beta-planes, *Mon. Weather Rev.*, **95**, 441–451, doi:10.1175/1520-0493(1967)095<0441:PWOBP>2.3.CO;2.
- Lindzen, R. S. (1974), Wave-CISK in the tropics, *J. Atmos. Sci.*, **31**, 156–179, doi:10.1175/1520-0469(1974)031<0156:WCITT>2.0.CO;2.
- Lindzen, R. S. (2003), The interaction of waves and convection in the tropics, *J. Atmos. Sci.*, **60**, 3009–3020, doi:10.1175/1520-0469(2003)060<3009:TIOWAC>2.0.CO;2.
- Lindzen, R. S., and J. R. Holton (1968), A theory of the quasi-biennial oscillation, *J. Atmos. Sci.*, **25**, 1095–1107, doi:10.1175/1520-0469(1968)025<1095:ATOTQB>2.0.CO;2.
- Lindzen, R. S., and T. Matsuno (1968), On the nature of large scale wave disturbances in the equatorial lower stratosphere, *J. Meteorol. Soc. Jpn.*, **46**, 215–221.
- Livezey, R. E., and W. Y. Chen (1983), Statistical field significance and its determination by Monte Carlo techniques, *Mon. Weather Rev.*, **111**, 46–59.
- Madden, R., and P. Julian (1971), Detection of a 40–50 day oscillation in the zonal wind in the tropical Pacific, *J. Atmos. Sci.*, **28**, 702–708, doi:10.1175/1520-0469(1971)028<0702:DOADDOI>2.0.CO;2.
- Madden, R., and P. Julian (1972), Description of global scale circulation cells in the tropics with a 40–50 day period, *J. Atmos. Sci.*, **29**, 1109–1123, doi:10.1175/1520-0469(1972)029<1109:DOGSCC>2.0.CO;2.
- Madden, R., and P. Julian (1994), Observations of the 40–50-day tropical oscillation-A review, *Mon. Weather Rev.*, **122**, 814–837, doi:10.1175/1520-0493(1994)122<0814:OOTDTO>2.0.CO;2.
- Magaña, V., and M. Yanai (1995), Mixed Rossby-gravity waves triggered by lateral forcing, *J. Atmos. Sci.*, **52**, 1473–1486, doi:10.1175/1520-0469(1995)052<1473:MRWTBL>2.0.CO;2.
- Majda, A. J. (2007), New multiscale models and self-similarity in tropical convection, *J. Atmos. Sci.*, **64**, 1393–1404, doi:10.1175/JAS3880.1.
- Majda, A. J., and M. G. Shefter (2001a), Waves and instabilities for model tropical convective parameterizations, *J. Atmos. Sci.*, **58**, 896–914, doi:10.1175/1520-0469(2001)058<0896:WAIFMT>2.0.CO;2.
- Majda, A. J., and M. G. Shefter (2001b), Models for stratiform instability and convectively coupled waves, *J. Atmos. Sci.*, **58**, 1567–1584, doi:10.1175/1520-0469(2001)058<1567:MFSIAC>2.0.CO;2.
- Majda, A. J., B. Khouider, G. N. Kiladis, K. H. Straub, and M. G. Shefter (2004), A model for convectively coupled tropical waves: Nonlinearity, rotation, and comparison with observations, *J. Atmos. Sci.*, **61**, 2188–2205, doi:10.1175/1520-0469(2004)061<2188:AMFCCT>2.0.CO;2.
- Mapes, B. E. (1998), The large-scale part of tropical mesoscale convective system circulations: A linear vertical spectral band model, *J. Meteorol. Soc. Jpn.*, **76**, 29–55.
- Mapes, B. E. (2000), Convective inhibition, subgrid-scale triggering energy, and stratiform instability in a toy tropical wave model, *J. Atmos. Sci.*, **57**, 1515–1535, doi:10.1175/1520-0469(2000)057<1515:CISSTE>2.0.CO;2.
- Mapes, B. E., and R. A. Houze (1995), Diabatic divergence profiles in western Pacific mesoscale convective systems, *J. Atmos. Sci.*, **52**, 1807–1828, doi:10.1175/1520-0469(1995)052<1807:DDPIWP>2.0.CO;2.
- Mapes, B. E., S. Tulich, J. Lin, and P. Zuidema (2006), The mesoscale convection life cycle: Building block or prototype for large-scale tropical waves?, *Dyn. Atmos. Oceans*, **42**, 3–29, doi:10.1016/j.dynatmoce.2006.03.003.
- Maruyama, T. (1967), Large-scale disturbances in the equatorial lower stratosphere, *J. Meteorol. Soc. Jpn.*, **45**, 196–199.
- Maruyama, T. (1994), Upward transport of westerly momentum due to disturbances of the equatorial lower stratosphere in the period range of about 2 days—Singapore data analysis for 1983–1993, *J. Meteorol. Soc. Jpn.*, **72**, 423–432.
- Masunaga, H. (2007), Seasonality and regionality of the Madden-Julian oscillation, Kelvin wave, and equatorial Rossby wave, *J. Atmos. Sci.*, **64**, 4400–4416, doi:10.1175/2007JAS2179.1.
- Masunaga, H., and C. D. Kummerow (2006), The Madden-Julian oscillation recorded in early observations from the Tropical Rainfall Measuring Mission (TRMM), *J. Atmos. Sci.*, **63**, 2777–2794, doi:10.1175/JAS3783.1.
- Matsuno, T. (1966), Quasi-geostrophic motions in the equatorial area, *J. Meteorol. Soc. Jpn.*, **44**, 25–43.
- Matthews, A. J., and J. Lander (1999), Physical and numerical contributions to the structure of Kelvin wave-CISK modes in a spectral transform model, *J. Atmos. Sci.*, **56**, 4050–4058, doi:10.1175/1520-0469(1999)056<4050:PANCTT>2.0.CO;2.
- Meehl, G. A., R. Lukas, G. N. Kiladis, K. M. Weickmann, A. J. Matthews, and M. Wheeler (2001), A conceptual framework for time and space scale interactions in the climate system, *Clim. Dyn.*, **17**, 753–775, doi:10.1007/s003820000143.
- Mekonnen, A., C. D. Thorncroft, A. R. Aiyer, and G. N. Kiladis (2008), Convectively coupled Kelvin waves over tropical Africa during the boreal summer: Structure and variability, *J. Clim.*, **21**, 6649–6667.
- Molinari, J., D. Vollaro, and C. Schreck (2006), Incorporation of equatorial wave modes into tropical synoptic meteorology: Is it worth the trouble?, paper 11C.1 presented at 27th Conference on Hurricanes and Tropical Meteorology, Am. Meteorol. Soc., Monterey, Calif.
- Molinari, J., K. Lombardo, and D. Vollaro (2007), Tropical cyclogenesis within an equatorial Rossby wave packet, *J. Atmos. Sci.*, **64**, 1301–1317, doi:10.1175/JAS3902.1.
- Moncrieff, M. W. (2004), Analytic representation of the large-scale organization of tropical convection, *J. Atmos. Sci.*, **61**, 1521–1538, doi:10.1175/1520-0469(2004)061<1521:AROTLO>2.0.CO;2.
- Moskowitz, B. M., and C. S. Bretherton (2000), An analysis of frictional feedback on a moist equatorial Kelvin mode, *J. Atmos. Sci.*, **57**, 2188–2206, doi:10.1175/1520-0469(2000)057<2188:AAOFFO>2.0.CO;2.

- Mounier, F., G. N. Kiladis, and S. Janicot (2007), Analysis of the dominant mode of convectively coupled Kelvin waves in the West African monsoon, *J. Clim.*, 20, 1487–1503, doi:10.1175/JCLI4059.1.
- Mounier, F., S. Janicot, and G. N. Kiladis (2008), The West African monsoon dynamics. Part III: The Quasi-Biweekly Zonal Dipole, *J. Clim.*, 21, 1911–1928.
- Murata, F., M. D. Yamanaka, H. Hashiguchi, S. Mori, M. Kudsy, T. Sribimawati, and B. Suhardi (2006), Dry intrusions following eastward-propagating synoptic-scale cloud systems over Sumatra Island, *J. Meteorol. Soc. Jpn.*, 84, 277–294.
- Nakazawa, T. (1986), Mean features of 30–60 day variations as inferred from 8-year OLR data, *J. Meteorol. Soc. Jpn.*, 64, 777–786.
- Nakazawa, T. (1988), Tropical super clusters within intraseasonal variations over the western Pacific, *J. Meteorol. Soc. Jpn.*, 66, 823–839.
- Nasuno, T., H. Tomita, S. Iga, H. Miura, and M. Satoh (2008), Convectively coupled equatorial waves simulated on an aquaplanet in a global nonhydrostatic experiment, *J. Atmos. Sci.*, 65, 1246–1265, doi:10.1175/2007JAS2395.1.
- Neelin, J. D., and I. M. Held (1987), Modeling tropical convergence based on the moist static energy budget, *Mon. Weather Rev.*, 115, 3–12, doi:10.1175/1520-0493(1987)115<0003:MTCBOT>2.0.CO;2.
- Neelin, J. D., and N. Zeng (2000), A quasi-equilibrium tropical circulation model-formulation, *J. Atmos. Sci.*, 57, 1741–1766, doi:10.1175/1520-0469(2000)057<1741:QETCM>2.0.CO;2.
- Nguyen, H., and J. P. Duvel (2008), Synoptic wave perturbations and convective systems over equatorial Africa, *J. Clim.*, 21, 6372–6388.
- Norquist, D. C., E. E. Recker, and R. J. Reed (1977), The energetics of African wave disturbances as observed during phase III of GATE, *Mon. Weather Rev.*, 105, 334–342, doi:10.1175/1520-0493(1977)105<0334:TEAOAWD>2.0.CO;2.
- Numaguti, A. (1995), Characteristics of 4-to-20-day-period disturbances observed in the equatorial Pacific during the TOGA COARE IOP, *J. Meteorol. Soc. Jpn.*, 73, 353–377.
- Pedlosky, J. (1987), *Geophysical Fluid Dynamics*, 710 pp., Springer, New York.
- Peters, M. E., and C. S. Bretherton (2006), Structure of tropical variability from a vertical mode perspective, *Theor. Comput. Fluid Dyn.*, 20, 501–524, doi:10.1007/s00162-006-0034-x.
- Pires, P., J.-L. Redelsperger, and J.-P. Lafore (1997), Equatorial atmospheric waves and their association to convection, *Mon. Weather Rev.*, 125, 1167–1184, doi:10.1175/1520-0493(1997)125<1167:EAWATA>2.0.CO;2.
- Raymond, D. J., and Z. Fuchs (2007), Convectively coupled gravity and moisture modes in a simple atmospheric model, *Tellus*, 59, 627–640, doi:10.1111/j.1600-0870.2007.00268.x.
- Raymond, D. J., G. B. Raga, C. S. Bretherton, J. Molinari, C. López-Carrillo, and Ž. Fuchs (2003), Convective forcing in the Intertropical Convergence Zone of the eastern Pacific, *J. Atmos. Sci.*, 60, 2064–2082, doi:10.1175/1520-0469(2003)060<2064:CFITIC>2.0.CO;2.
- Reed, R. J., and E. E. Recker (1971), Structure and properties of synoptic-scale wave disturbances in the equatorial western Pacific, *J. Atmos. Sci.*, 28, 1117–1133, doi:10.1175/1520-0469(1971)028<1117:SAPSOSS>2.0.CO;2.
- Reed, R. J., D. C. Norquist, and E. E. Recker (1977), The structure and properties of African wave disturbances as observed during phase III of GATE, *Mon. Weather Rev.*, 105, 317–333.
- Riehl, H. (1945), Waves in the easterlies and the polar front in the tropics, *Misc. Rep.* 17, 79 pp., Dep. of Meteorol., Univ. of Chicago, Chicago, Ill.
- Riehl, H. (1948), On the formation of typhoons, *J. Meteorol.*, 5, 247–264.
- Rosenthal, S. L. (1960), A simplified linear theory of equatorial easterly waves, *J. Meteorol.*, 17, 484–488.
- Rosenthal, S. L. (1965), Some preliminary theoretical considerations of tropospheric wave motions in equatorial latitudes, *Mon. Weather Rev.*, 93, 605–612, doi:10.1175/1520-0493(1965)093<0605:SPTCOT>2.3.CO;2.
- Roundy, P. E. (2008), Analysis of convectively coupled Kelvin waves in the Indian Ocean MJO, *J. Atmos. Sci.*, 65, 1342–1359, doi:10.1175/2007JAS2345.1.
- Roundy, P. E., and W. M. Frank (2004a), A climatology of waves in the equatorial region, *J. Atmos. Sci.*, 61, 2105–2132, doi:10.1175/1520-0469(2004)061<2105:ACOWIT>2.0.CO;2.
- Roundy, P. E., and W. M. Frank (2004b), Effects of low-frequency wave interactions on intraseasonal oscillations, *J. Atmos. Sci.*, 61, 3025–3040, doi:10.1175/JAS-3348.1.
- Roundy, P. E., and W. M. Frank (2004c), Applications of a multiple linear regression model to the analysis of relationships between eastward- and westward-moving intraseasonal modes, *J. Atmos. Sci.*, 61, 3041–3048, doi:10.1175/JAS-3349.1.
- Salby, M. L., and R. R. Garcia (1987), Transient response to localized episodic heating in the tropics. Part I: Excitation and short-time near field behavior, *J. Atmos. Sci.*, 44, 458–498, doi:10.1175/1520-0469(1987)044<0458:TRTLEH>2.0.CO;2.
- Sato, K., F. Hasegawa, and I. Hirota (1994), Short-period disturbances in the equatorial lower stratosphere, *J. Meteorol. Soc. Jpn.*, 72, 859–872.
- Schrage, J. M., C. A. Clayson, and B. Strahl (2001), Statistical properties of episodes of enhanced 2–3-day convection in the Indian and Pacific oceans, *J. Clim.*, 14, 3482–3494, doi:10.1175/1520-0442(2001)014<3482:SPOEOE>2.0.CO;2.
- Serra, Y. L., G. N. Kiladis, and M. F. Cronin (2008), Horizontal and vertical structure of easterly waves in the Pacific ITCZ, *J. Atmos. Sci.*, 65, 1266–1284, doi:10.1175/2007JAS2341.1.
- Sherwood, S. C. (1999), Convective precursors and predictability in the tropical western Pacific, *Mon. Weather Rev.*, 127, 2977–2991, doi:10.1175/1520-0493(1999)127<2977:CPAPIT>2.0.CO;2.
- Sherwood, S. C., and R. Wahrlrich (1999), Observed evolution of tropical deep convective events and their environment, *Mon. Weather Rev.*, 127, 1777–1795, doi:10.1175/1520-0493(1999)127<1777:OEOTDC>2.0.CO;2.
- Shinoda, T., and W. Han (2005), Influence of the Indian Ocean dipole on atmospheric subseasonal variability, *J. Clim.*, 18, 3891–3909, doi:10.1175/JCLI3510.1.
- Shutts, G. (2006), Upscale effects in simulations of tropical convection on an equatorial beta-plane, *Dyn. Atmos. Oceans*, 42, 30–58, doi:10.1016/j.dynatmoce.2006.02.006.
- Slingo, J. M., P. M. Inness, and K. R. Sperber (2005), Modeling, in *Intraseasonal Variability in the Atmosphere-Ocean Climate System*, edited by W. K.-M. Lau and D. Waliser, chap. 11, pp. 361–388, Springer, New York.
- Smith, R. K., G. Garden, J. Molinari, and B. R. Morton (2001), Proceedings of an International Workshop on the Dynamics and Forecasting of Tropical Weather Systems, *Bull. Am. Meteorol. Soc.*, 82, 2825–2829.
- Sobel, A. H., and C. S. Bretherton (1999), Development of synoptic-scale disturbances over the summertime tropical northwest Pacific, *J. Atmos. Sci.*, 56, 3106–3127, doi:10.1175/1520-0469(1999)056<3106:DOSSDO>2.0.CO;2.
- Sobel, A. H., and S. J. Camargo (2005), Influence of western North Pacific tropical cyclones on their large-scale environment, *J. Atmos. Sci.*, 62, 3396–3407, doi:10.1175/JAS3539.1.
- Sobel, A. H., and T. Horinouchi (2000), On the dynamics of easterly waves, monsoon depressions, and tropical depression type disturbances, *J. Meteorol. Soc. Jpn.*, 78, 167–173.
- Sobel, A. H., S. E. Yuter, C. S. Bretherton, and G. N. Kiladis (2004), Large-scale meteorology and deep convection during TRMM KWAJEX, *Mon. Weather Rev.*, 132, 422–444, doi:10.1175/1520-0493(2004)132<0422:LMADCD>2.0.CO;2.

- Stevens, B., D. A. Randall, X. Lin, and M. T. Montgomery (1997), Comments on ‘On large-scale circulations in convecting atmospheres’ by Kerry A. Emanuel, J. David Neelin and Christopher S. Bretherton, *Q. J. R. Meteorol. Soc.*, **123**, 1771–1778.
- Straub, K. H., and G. N. Kiladis (2002), Observations of a convectively coupled Kelvin wave in the eastern Pacific ITCZ, *J. Atmos. Sci.*, **59**, 30–53, doi:10.1175/1520-0469(2002)059<0030:OOACCK>2.0.CO;2.
- Straub, K. H., and G. N. Kiladis (2003a), Extratropical forcing of convectively coupled Kelvin waves during austral winter, *J. Atmos. Sci.*, **60**, 526–543, doi:10.1175/1520-0469(2003)060<0526:EFOCCK>2.0.CO;2.
- Straub, K. H., and G. N. Kiladis (2003b), Interactions between the boreal summer intraseasonal oscillation and higher frequency tropical wave activity, *Mon. Weather Rev.*, **131**, 945–960, doi:10.1175/1520-0493(2003)131<0945:IBTBSI>2.0.CO;2.
- Straub, K. H., and G. N. Kiladis (2003c), The observed structure of convectively coupled Kelvin waves: Comparison with simple models of coupled wave instability, *J. Atmos. Sci.*, **60**, 1655–1668, doi:10.1175/1520-0469(2003)060<1655:TOSOCC>2.0.CO;2.
- Straub, K. H., G. N. Kiladis, and P. E. Ciesielski (2006), The role of equatorial waves in the onset of the South China Sea summer monsoon and the demise of El Niño during 1998, *Dyn. Atmos. Oceans*, **42**, 216–238, doi:10.1016/j.dynatmoce.2006.02.005.
- Suzuki, T., Y. N. Takayabu, and S. Emori (2006), Coupling mechanisms between equatorial waves and cumulus convection in an AGCM, *Dyn. Atmos. Oceans*, **42**, 81–106, doi:10.1016/j.dynatmoce.2006.02.004.
- Tai, K.-S., and Y. Ogura (1987), An observational study of easterly waves over the eastern Pacific in the northern summer using FGGE data, *J. Atmos. Sci.*, **44**, 339–361, doi:10.1175/1520-0469(1987)044<0339:AOSOEW>2.0.CO;2.
- Takayabu, Y. N. (1994a), Large-scale cloud disturbances associated with equatorial waves. Part I: Spectral features of the cloud disturbances, *J. Meteorol. Soc. Jpn.*, **72**, 433–448.
- Takayabu, Y. N. (1994b), Large-scale cloud disturbances associated with equatorial waves. Part II: Westward propagating inertio-gravity waves, *J. Meteorol. Soc. Jpn.*, **72**, 451–465.
- Takayabu, Y. N., and M. Murakami (1991), The structure of super cloud clusters observed in 1–20 June 1986 and their relationship to easterly waves, *J. Meteorol. Soc. Jpn.*, **69**, 105–125.
- Takayabu, Y. N., and T. S. Nitta (1993), 3–5 day-period disturbances coupled with convection over the tropical Pacific Ocean, *J. Meteorol. Soc. Jpn.*, **71**, 221–246.
- Takayabu, Y. N., K.-M. Lau, and C.-H. Sui (1996), Observation of a quasi-2-day wave during TOGA COARE, *Mon. Weather Rev.*, **124**, 1892–1913, doi:10.1175/1520-0493(1996)124<1892:OOAQDW>2.0.CO;2.
- Takayabu, Y. N., T. Iguchi, M. Kachi, A. Shibata, and H. Kanzawa (1999), Abrupt termination of the 1997–98 El Niño in response to a Madden-Julian oscillation, *Nature*, **402**, 279–282, doi:10.1038/46254.
- Tam, C.-Y., and T. Li (2006), Origin and dispersion characteristics of the observed tropical summertime synoptic scale waves over the western Pacific, *Mon. Weather Rev.*, **134**, 1630–1646, doi:10.1175/MWR3147.1.
- Thompson, R. M., Jr., S. W. Payne, E. E. Recker, and R. J. Reed (1979), Structure and properties of synoptic-scale wave disturbances in the Intertropical Convergence Zone of the eastern Atlantic, *J. Atmos. Sci.*, **36**, 53–72, doi:10.1175/1520-0469(1979)036<0053:SAPSOSS>2.0.CO;2.
- Thorncroft, C. D., N. M. J. Hall, and G. N. Kiladis (2008), Three dimensional structure and dynamics of African easterly waves. Part III: Genesis, *J. Atmos. Sci.*, **65**, 3596–3607.
- Tindall, J. C., J. Thuburn, and E. J. Highwood (2006), Equatorial waves in the lower stratosphere. I: A novel detection method, *Q. J. R. Meteorol. Soc.*, **132**, 177–194, doi:10.1256/qj.04.152.
- Tomita, H., H. Miura, S. Iga, T. Nasuno, and M. Satoh (2005), A global cloud-resolving simulation: Preliminary results from an aqua planet experiment, *Geophys. Res. Lett.*, **32**, L08805, doi:10.1029/2005GL022459.
- Tsuda, T., Y. Murayama, H. Wiriyosumarto, S. W. B. Harijono, and S. Kato (1994a), Radiosonde observations of equatorial atmospheric dynamics over Indonesia: 1. Equatorial waves and diurnal tides, *J. Geophys. Res.*, **99**, 10,491–10,505, doi:10.1029/94JD00355.
- Tsuda, T., Y. Murayama, H. Wiriyosumarto, S. W. B. Harijono, and S. Kato (1994b), Radiosonde observations of equatorial atmospheric dynamics over Indonesia: 2. Characteristics of gravity waves, *J. Geophys. Res.*, **99**, 10,507–10,516, doi:10.1029/94JD00354.
- Tulich, S. N., and B. E. Mapes (2008), Multiscale convective wave disturbances in the tropics: Insights from a two-dimensional cloud-resolving model, *J. Atmos. Sci.*, **65**, 140–165, doi:10.1175/2007JAS2353.1.
- Tulich, S. N., D. A. Randall, and B. E. Mapes (2007), Vertical-mode and cloud decomposition of large-scale convectively coupled gravity waves in a two-dimensional cloud-resolving model, *J. Atmos. Sci.*, **64**, 1210–1229, doi:10.1175/JAS3884.1.
- Uppala, S. M., et al. (2005), The ERA-40 re-analysis, *Q. J. R. Meteorol. Soc.*, **131**, 2961–3012, doi:10.1256/qj.04.176.
- Waliser, D. E. (2006), Intraseasonal variability, in *The Asian Monsoon*, edited by B. Wang, chap. 5, pp. 203–257, Springer, New York.
- Wallace, J. M. (1971), Spectral studies of tropospheric wave disturbances in the tropical western Pacific, *Rev. Geophys.*, **9**, 557–612, doi:10.1029/RG009i003p00557.
- Wallace, J. M., and L. A. Chang (1972), On the application of satellite data on the cloud brightness to the study of tropical wave disturbances, *J. Atmos. Sci.*, **29**, 1400–1403, doi:10.1175/1520-0469(1972)029<1400:OTAOSD>2.0.CO;2.
- Wallace, J. M., and V. E. Kousky (1968), Observational evidence of Kelvin waves in the tropical stratosphere, *J. Atmos. Sci.*, **25**, 900–907, doi:10.1175/1520-0469(1968)025<0900:OEOK-WI>2.0.CO;2.
- Wang, B. (1988), Dynamics of tropical low-frequency waves: An analysis of the moist Kelvin wave, *J. Atmos. Sci.*, **45**, 2051–2065, doi:10.1175/1520-0469(1988)045<2051:DOTLFW>2.0.CO;2.
- Wang, B. (2005), Theory, in *Intraseasonal Variability in the Atmosphere-Ocean Climate System*, edited by W. K.-M. Lau and D. Waliser, chap. 10, pp. 307–351, Springer, New York.
- Wang, B., and H. Rui (1990), Dynamics of the coupled moist Kelvin-Rossby wave on an equatorial  $\beta$ -plane, *J. Atmos. Sci.*, **47**, 397–413, doi:10.1175/1520-0469(1990)047<0397:DOTCMK>2.0.CO;2.
- Wang, B., and X. Xie (1996), Low-frequency equatorial waves in vertically sheared zonal flow. Part I: Stable waves, *J. Atmos. Sci.*, **53**, 449–467, doi:10.1175/1520-0469(1996)053<0449:LFEWIV>2.0.CO;2.
- Wang, H., and R. Fu (2007), The influence of Amazon rainfall on the Atlantic ITCZ through convectively coupled Kelvin waves, *J. Clim.*, **20**, 1188–1201, doi:10.1175/JCLI4061.1.
- Webster, P. J., and H.-R. Chang (1988), Equatorial energy accumulation and emanation regions: Impacts of a zonally varying basic state, *J. Atmos. Sci.*, **45**, 803–829, doi:10.1175/1520-0469(1988)045<0803:EEAAER>2.0.CO;2.
- Weickmann, K. M., and E. Berry (2007), A synoptic-dynamic model of subseasonal atmospheric variability, *Mon. Weather Rev.*, **135**, 449–474, doi:10.1175/MWR3293.1.
- Wheeler, M. C. (2002), Tropical meteorology: Equatorial waves, in *Encyclopedia of Atmospheric Sciences*, edited by J. Holton, J. Curry, and J. Pyle, pp. 2313–2325, Academic, San Diego, Calif.
- Wheeler, M., and G. N. Kiladis (1999), Convectively coupled equatorial waves: Analysis of clouds and temperature in the wavenumber-frequency domain, *J. Atmos. Sci.*, **56**, 374–399, doi:10.1175/1520-0469(1999)056<0374:CCEWAO>2.0.CO;2.

- Wheeler, M. C., and J. L. McBride (2005), Australian-Indonesian monsoon, in *Intraseasonal Variability in the Atmosphere-Ocean Climate System*, edited by W. K. M. Lau and D. E. Waliser, pp. 125–173, Springer, New York.
- Wheeler, M., and K. M. Weickmann (2001), Real-time monitoring and prediction of modes of coherent synoptic to intraseasonal tropical variability, *Mon. Weather Rev.*, 129, 2677–2694, doi:10.1175/1520-0493(2001)129<2677:RTMAPO>2.0.CO;2.
- Wheeler, M., G. N. Kiladis, and P. J. Webster (2000), Large-scale dynamical fields associated with convectively coupled equatorial waves, *J. Atmos. Sci.*, 57, 613–640, doi:10.1175/1520-0469(2000)057<0613:LSDFAW>2.0.CO;2.
- Wunsch, C., and A. E. Gill (1976), Observations of equatorially trapped waves in Pacific sea level variations, *Deep Sea Res.*, 23, 371–390.
- Xu, K.-M., and K. A. Emanuel (1989), Is the tropical atmosphere conditionally unstable?, *Mon. Weather Rev.*, 117, 1471–1479, doi:10.1175/1520-0493(1989)117<1471:ITTACU>2.0.CO;2.
- Yanai, M., and T. Maruyama (1966), Stratospheric wave disturbances propagating over the equatorial Pacific, *J. Meteorol. Soc. Jpn.*, 44, 291–294.
- Yanai, M., and M. Murakami (1970a), A further study of tropical wave disturbances by the use of spectrum analysis, *J. Meteorol. Soc. Jpn.*, 48, 185–197.
- Yanai, M., and M. Murakami (1970b), Spectrum analysis of symmetric and anti-symmetric equatorial waves, *J. Meteorol. Soc. Jpn.*, 48, 331–347.
- Yanai, M., S. Esbensen, and J. Chu (1973), Determination of bulk properties of tropical cloud clusters from large-scale heat and moisture budgets, *J. Atmos. Sci.*, 30, 611–627, doi:10.1175/1520-0469(1973)030<0611:DOBPOT>2.0.CO;2.
- Yang, G.-Y., B. Hoskins, and J. Slingo (2003), Convectively coupled equatorial waves: A new methodology for identifying wave structures in observational data, *J. Atmos. Sci.*, 60, 1637–1654, doi:10.1175/1520-0469(2003)060<1637:CCEWAN>2.0.CO;2.
- Yang, G.-Y., B. Hoskins, and J. Slingo (2007a), Convectively coupled equatorial waves. Part I: Horizontal and vertical structures, *J. Atmos. Sci.*, 64, 3406–3423, doi:10.1175/JAS4017.1.
- Yang, G.-Y., B. Hoskins, and J. Slingo (2007b), Convectively coupled equatorial waves. Part II: Propagation characteristics, *J. Atmos. Sci.*, 64, 3424–3437, doi:10.1175/JAS4018.1.
- Yang, G.-Y., B. Hoskins, and J. Slingo (2007c), Convectively coupled equatorial waves. Part III: Synthesis structures and their forcing and evolution, *J. Atmos. Sci.*, 64, 3438–3451, doi:10.1175/JAS4019.1.
- Yang, G.-Y., J. Slingo, and B. Hoskins (2009), Convectively coupled equatorial waves in high resolution Hadley centre climate models, *J. Clim.*, in press.
- Yokoi, S., and T. Satomura (2005), An observational study of intraseasonal variations over Southeast Asia during the 1998 rainy season, *Mon. Weather Rev.*, 133, 2091–2104, doi:10.1175/MWR2967.1.
- Yoshida, K. (1959), A theory of the Cromwell Current (the equatorial undercurrent) and of the equatorial upwelling—An interpretation in a similarity to a coastal circulation, *J. Oceanogr. Soc. Jpn.*, 15, 159–170.
- Yu, J.-Y., C. Chou, and J. D. Neelin (1998), Estimating the gross moist stability of the tropical atmosphere, *J. Atmos. Sci.*, 55, 1354–1372, doi:10.1175/1520-0469(1998)055<1354:ETGMSO>2.0.CO;2.
- Žagar, N., N. Gustafsson, and E. Källén (2004), Dynamical response of equatorial waves in four-dimensional variational data assimilation, *Tellus*, 56A, 29–46.
- Žagar, N., E. Andersson, and M. Fisher (2005), Balanced tropical data assimilation based on study of equatorial waves in ECMWF short-range forecast errors, *Q. J. R. Meteorol. Soc.*, 131, 987–1011, doi:10.1256/qj.04.54.
- Zangvil, A. (1975), Temporal and spatial behavior of large-scale disturbances in tropical cloudiness deduced from satellite brightness data, *Mon. Weather Rev.*, 103, 904–920, doi:10.1175/1520-0493(1975)103<0904:TASBOL>2.0.CO;2.
- Zangvil, A., and M. Yanai (1980), Upper tropospheric waves in the tropics. Part I: Dynamical analysis in the wavenumber-frequency domain, *J. Atmos. Sci.*, 37, 283–298, doi:10.1175/1520-0469(1980)037<0283:UTWITT>2.0.CO;2.
- Zangvil, A., and M. Yanai (1981), Upper tropospheric waves in the tropics. Part II: Association with clouds in the wavenumber-frequency domain, *J. Atmos. Sci.*, 38, 939–953, doi:10.1175/1520-0469(1981)038<0939:UTWITT>2.0.CO;2.
- Zeng, N., J. D. Neelin, and C. Chou (2000), A quasi-equilibrium tropical circulation model—Implementation and simulation, *J. Atmos. Sci.*, 57, 1767–1796, doi:10.1175/1520-0469(2000)057<1767:AQETCM>2.0.CO;2.
- Zhang, C. (2005), The Madden-Julian oscillation, *Rev. Geophys.*, 43, RG2003, doi:10.1029/2004RG000158.
- Zhang, C., and H. H. Hendon (1997), Propagating and standing components of the intraseasonal oscillation in tropical convection, *J. Atmos. Sci.*, 54, 741–752, doi:10.1175/1520-0469(1997)054<0741:PASCOLT>2.0.CO;2.
- Zhou, X., and B. Wang (2007), Transition from an eastern Pacific upper-level mixed Rossby-gravity wave to a western Pacific tropical cyclone, *Geophys. Res. Lett.*, 34, L24801, doi:10.1029/2007GL031831.
- Zhu, B., and B. Wang (1993), The 30–60-day convection seesaw between the tropical Indian and western Pacific oceans, *J. Atmos. Sci.*, 50, 184–199, doi:10.1175/1520-0469(1993)050<0184:TDCSBT>2.0.CO;2.

P. T. Haertel, Department of Geology and Geophysics, Yale University, New Haven, CT 06520, USA.

G. N. Kiladis, Earth System Research Laboratory, NOAA, 325 Broadway, Boulder, CO 80305-3328, USA. (george.kiladis@noaa.gov)

P. E. Roundy, Department of Atmospheric and Environmental Sciences, State University of New York at Albany, Albany, NY 12222, USA.

K. H. Straub, Department of Earth and Environmental Sciences, Susquehanna University, Selinsgrove, PA 17870, USA.

M. C. Wheeler, Bureau of Meteorology, Centre for Australian Weather and Climate Research, Melbourne, Vic 3001, Australia.